



**IMPACT OF TRENCH AND RAMP FILM COOLING DESIGNS TO REDUCE  
HEAT RELEASE EFFECTS IN A REACTING FLOW**

THESIS

Michael R. DeLallo, Captain, USAF

AFIT/GAE/ENY/12-M10

**DEPARTMENT OF THE AIR FORCE  
AIR UNIVERSITY**

***AIR FORCE INSTITUTE OF TECHNOLOGY***

---

**Wright-Patterson Air Force Base, Ohio**

APPROVED FOR PUBLIC RELEASE; DISTRIBUTION UNLIMITED

The views expressed in this thesis are those of the author and do not reflect the official policy or position of the United States Air Force, Department of Defense, or the United States Government. This material is declared a work of the U.S. Government and is not subject to copyright protection in the United States.

AFIT/GAE/ENY/12-M10

**IMPACT OF TRENCH AND RAMP FILM COOLING DESIGNS TO REDUCE  
HEAT RELEASE EFFECTS IN A REACTING FLOW**

THESIS

Presented to the Faculty

Department of Aeronautics and Astronautics

Graduate School of Engineering and Management

Air Force Institute of Technology

Air University

Air Education and Training Command

In Partial Fulfillment of the Requirements for the  
Degree of Master of Science in Aeronautical Engineering

Michael R. DeLallo, BS

Captain, USAF

March 2012

APPROVED FOR PUBLIC RELEASE; DISTRIBUTION UNLIMITED.

AFIT/GAE/ENY/12-M10

**IMPACT OF TRENCH AND RAMP FILM COOLING DESIGNS TO REDUCE  
HEAT RELEASE EFFECTS IN A REACTING FLOW**

Michael R. DeLallo, BS  
Captain, USAF

Approved:

\_\_\_\_\_  
Dr. Marc D. Polanka, (Chairman)

\_\_\_\_\_  
Date

\_\_\_\_\_  
Dr. Mark Reeder, (Member)

\_\_\_\_\_  
Date

\_\_\_\_\_  
Dr. James Rutledge, (Member)

\_\_\_\_\_  
Date

## **Abstract**

Increasing combustor fuel-air ratios are a recent area of concern in gas turbine film cooling due to the potential for heat release on the surface of film-cooled components. This investigation compared four different cooling designs on their heat release potential: namely fanned, normal and radial trenched, and ramped. Measurements of heat flux to the downstream surface, when subjected to a reacting mainstream flow, provide a qualitative comparison between the four tested configurations. Furthermore, this work studied the effect of multiple injection points in series along the surface of a flat plate. An upstream set of normal holes and an upstream slot are evaluated on their ability to protect the downstream coolant flow from the fuel rich mainstream. Results are presented in terms of heat flux, augmentation of heat flux, and adiabatic wall temperature calculations. Downstream heat release is suspected to be a result of coolant interaction with local free radical concentrations. Concentrations, volume flow rates and jet to mainstream momentum ratio dictate local equivalence ratio and hence, the available local enthalpy generation.

## **Acknowledgements**

Throughout this thesis effort, numerous people have given me overwhelming help and support. My faculty advisor, Dr Marc Polanka guided me through each obstacle I encountered. The AFIT laboratory staff always provided me with the tools, experience, and expertise needed. Dr Scott Stouffer and Dr David Blunck, my sponsors from the AFRL Propulsion Directorate, supplied the insight and assistance required to obtain our results. I would also like to recognize the efforts of Mike Arstingstall of UDRI for his assistance in helping to set up and run the equipment necessary to conduct this experiment and Jacob Wilson from our lab for his help drawing the film cooling designs. I would like to thank Brian Bohan of the Air Force Research Laboratory for his efforts in updating the facility and in acquiring the fan shaped hole data used in this effort.

Capt Michael R. DeLallo

# Table of Contents

Page

Abstract.....	iv
Acknowledgements.....	v
Table of Contents.....	vi
List of Figures.....	viii
List of Tables.....	xii
<i>List of Symbols</i> .....	xiii
List of Abbreviations.....	iv
I. Introduction.....	1
I.1 Film cooling and heat release.....	3
I.2 The Ultra Compact Combustor.....	5
I.3 Thesis Objective.....	7
II. Literature Review.....	9
II.1 Film cooling.....	9
II.1.1 Momentum flux.....	11
II.1.2 Blowing ratio.....	12
II.1.3 Turbulence.....	14
II.1.4 Injection angle and hole shape.....	16
II.1.5 Surface curvature.....	18
II.2 Combustor design.....	20
II.3 Perpendicular jet injection.....	25
II.4 Reaction rates and potential heat release.....	27
III. EXPERIMENTAL SETUP.....	31
III.1 Test Setup.....	31
III.2 Test method.....	35
III.3 Heat sink.....	41
III.4 Configurations tested.....	43
III.5 Pictures of different blowing conditions.....	48
III.6 Correction factors and error analysis.....	51
III.7 Methods of analysis.....	59
III.7.1 Augmentation.....	60

III.7.2	Normalized wall temperature.....	61
III.7.3	Extrapolating to adiabatic wall temperature .....	66
III.8	Determination of WSR Equivalence Ratio .....	67
IV.	Results and Analysis .....	71
IV.1	Test Matrix for Phase I and Phase II.....	71
IV.2	Data Analysis Techniques for Phase I and Phase II .....	72
IV.3	Augmentation.....	74
IV.3.1	Phase I - Single Row Injection at 25 Hole Diameters .....	74
IV.3.2	Phase II - Single Row Injection at 25 Hole Diameters .....	78
IV.3.3	Phase I - Single Row Injection at 95 Hole Diameters .....	83
IV.3.4	Phase II - Single Row Injection at 95 Hole Diameters .....	86
IV.3.5	Phase I - Series Injection Data at 25 hole diameters.....	89
IV.3.6	Phase II - Series Injection Data at 51 hole diameters .....	96
IV.3.7	Phase I and II - Volumetric comparison of upstream input .....	102
IV.4	Phase I and II - Normalized wall temperature .....	106
V.	Conclusions and Recommendations .....	115
V.1	Overview.....	115
V.2	Augmentation Conclusion .....	116
V.3	Adiabatic Wall Temperature Calculation Conclusion .....	117
V.4	Recommendations for Future Work.....	118
VI.	BIBLIOGRAPHY.....	130

## List of Figures

	Page
Figure I-1. Turbine inlet temperature impact on engine performance [1] .....	2
Figure I-2. Dual-spool turbofan engine with station numbers, [2] .....	4
Figure I-3. High pressure turbine blade .....	5
Figure I-4. Conventional and UCC circumferential cavity.....	6
Figure I-5. UCC hybrid vane cascade, [3] .....	6
Figure II-1. Dimensionless temperature along jet centerline (I=0.5) [4].....	12
Figure II-2. Dimensionless temperature along jet centerline (I=0.63) [4].....	12
Figure II-3. Dimensionless temperature along jet centerline (I=0.83) [4].....	12
Figure II-4. Effectiveness (-B/A) with downstream distance, G=Blowing ratio, DR=1.25 [5] .....	13
Figure II-5. Effectiveness variation (-B/A) with downstream distance, G=Blowing ratio, DR=1.67 [5].....	14
Figure II-6. Adiabatic conditions under turbulent conditions [6].....	16
Figure II-7. Cooling hole geometries and effectiveness results [7].....	17
Figure II-8. Cylindrical, fan shape, laidback fan shape configurations [8] .....	18
Figure II-9. 2-D adiabatic effectiveness contours[8] .....	18
Figure II-10. Variation of lateral average effectiveness[10].....	20
Figure II-11. J79 combustor can .....	21
Figure II-12. Annular combustor illustration (GE CF6-80C).....	22
Figure II-13. Various slot configurations [11].....	23
Figure II-14. Slot parameter diagram [13].....	25
Figure II-15. Lateral jet injection into combustion chamber [2] .....	27
Figure III-1. Front view of test rig .....	32
Figure III-2. Lower half of reactor core with jet ring inside WSR housing .....	33
Figure III-3. Experimental test setup .....	34
Figure III-4. Flow straightener.....	34
Figure III-5. Example test spread sheet – Phase II, normal trench – Dec-15-2011 .....	37
Figure III-6. Phase II - Time response - C shallow thermocouple –.....	39
Figure III-7. Phase II - Time response – C deep thermocouple –.....	39

Figure III-8. Time rate of change in temperature - C deep & shallow thermocouple – $\phi=1.3$ US: Offset normal DS: Normal trench .....	41
Figure III-9. Cooling configurations .....	45
Figure III-10. Offset normal drawing detail (cm) .....	45
Figure III-11. Laidback fan shape drawing detail (cm) .....	45
Figure III-12. Angled slot drawing detail (cm) .....	46
Figure III-13. Normal trench drawing detail (cm) .....	46
Figure III-14. Radial trench drawing detail (mm) .....	46
Figure III-15. Ramp drawing detail (cm) .....	46
Figure III-16. Camera viewpoint, arrow pointing from front of camera to test rig .....	49
Figure III-17. Phase II - Air injection; .....	50
Figure III-18. Phase II - Air injection; .....	50
Figure III-19. Error estimations of phase I testing – inter day, DS: variable US: offset normal w/ radial trench downstream, all other cases blank .....	52
Figure III-20. Zero-Zero plot results of phase II testing w/o ramp .....	53
Figure III-21. Zero-zero data with ramp included .....	58
Figure III-22. Adiabatic wall temperature extrapolation example .....	67
Figure III-23. Phase I: Max augmentation( $\sigma$ ) for fan configuration at $x/d_j = 25$ .....	69
Figure III-24. Phase I: Heat flux data, fan at $x/d_j = 25$ , air-coolant .....	70
Figure III-25. Phase I: Heat flux data, fan at $x/d_j = 25$ , $N_2$ -coolant .....	70
Figure IV-1. Phase I - $N_2$ injection at $x/d_j = 25$ ; .....	75
Figure IV-2. Phase I - Air injection at $x/d_j = 25$ ; .....	76
Figure IV-3. Phase I – Augmentation( $\sigma$ ) at $x/d_j = 25$ , $\phi=1.3$ , .....	77
Figure IV-4. Phase II - $N_2$ injection at $x/d_j = 25$ ; .....	79
Figure IV-5. Phase II - Air injection at $x/d_j = 25$ ; .....	80
Figure IV-6. Phase II – Augmentation( $\sigma$ ) at $x/d_j = 25$ , $\phi=1.3$ , .....	82
Figure IV-7. Phase II – From left to right: normal trench, radial trench and ramp, $\phi=1.3$ , .....	83
Figure IV-8. Phase I – $N_2$ injection at $x/d_j = 95$ ; .....	84
Figure IV-9. Phase I - Air injection at $x/d_j = 95$ ; .....	85
Figure IV-10. Phase I – Augmentation ( $\sigma$ ) at $x/d_j = 95$ , $\phi=1.3$ , .....	86
Figure IV-11. Phase II – $N_2$ injection at $x/d_j = 95$ ; .....	87
Figure IV-12. Phase II - Air injection at $x/d_j = 95$ ; .....	88

Figure IV-13. Phase II – Augmentation ( $\sigma$ ) at $x/d_j=95$ , $\phi=1.3$ , .....	89
Figure IV-14. Phase I - Heat flux for $N_2$ injection at $\phi=1.3$ , $x/d_j = 51$ , US: Offset normal, DS: $M= 2.0$ , Geometry = Variable.....	91
Figure IV-15. Phase I - Heat flux for air injection at $\phi=1.3$ , $x/d_j = 51$ , US: Offset normal, DS: $M= 2.0$ , Geometry = Variable.....	92
Figure IV-16. Phase I – Augmentation ( $\sigma$ ), at $\phi=1.3$ , $x/d_j = 51$ , US: Offset normal, DS: $M= 2.0$ , Geometry = Variable .....	92
Figure IV-17. Phase I - Heat flux for air injection, at $\phi=1.3$ , $x/d_j = 51$ , US: SLOT, DS: Variable.....	94
Figure IV-18. Phase I - Heat flux for $N_2$ injection, at $\phi=1.3$ , $x/d_j = 51$ , US: SLOT, DS: Variable.....	95
Figure IV-19. Phase I – Augmentation ( $\sigma$ ), at $\phi=1.3$ , $x/d_j = 51$ , US: Slot, DS: Variable .....	95
Figure IV-20. Phase II - Heat flux for air injection at $\phi=1.3$ , $x/d_j = 51$ , US: Offset normal, DS: $M= 2.0$ , Geometry = Variable.....	97
Figure IV-21. Phase II - Heat flux for $N_2$ injection at $\phi=1.3$ , $x/d_j = 51$ , US: Offset normal, DS: $M= 2.0$ , Geometry = Variable.....	98
Figure IV-22. Phase II – Augmentation ( $\sigma$ ), at $\phi=1.3$ , $x/d_j = 51$ , US: Offset normal, DS: $M= 2.0$ , .....	99
Figure IV-23. Phase II - Heat flux for air injection, at $\phi=1.3$ , $x/d_j = 51$ , US: SLOT, DS: Variable.....	100
Figure IV-24. Phase II - Heat flux for $N_2$ injection, at $\phi=1.3$ , $x/d_j = 51$ , US: SLOT, DS: Variable.....	101
Figure IV-25. Phase II – Augmentation ( $\sigma$ ), at $\phi=1.3$ , $x/d_j = 51$ , US: Slot, DS: Variable .....	102
Figure IV-26. Volume flow rate comparison between slot (Left) and offset normal (right): $V = 9.5$ SLPM; $\phi=1.3$ ; US: Slot or Offset normal; DS: Normal trench.....	103
Figure IV-27. Phase I - SLPM comparison at $\phi=1.3$ , $x/d_j = 51$ ,.....	105
Figure IV-28. Phase II - SLPM comparison at $\phi=1.3$ , $x/d_j = 51$ ,.....	105
Figure IV-29. Phase I - Normalized temperature at $\phi=1.3$ , US: Variable, DS: Normal trench.....	107
Figure IV-30. Phase II - Normalized temperature at $\phi=1.3$ , US: Variable, DS: Normal trench.....	109
Figure IV-31. Air and $N_2$ extrapolation zoom view at $x/d_j = 25$ ; US: Blank DS: Normal Trench - $\phi=1.3$ .....	112

Figure IV-32. Adiabatic wall temp extrapolation at  $x/d_j = 25$ ; US: Blank DS:  
Normal Trench -  $\phi=1.3$  ..... 112

<b>List of Tables</b>	<b>Page</b>
Table II-1. Factors affecting film cooling performance (subscript “c” represents coolant, subscript “∞” represents mainstream).....	11
Table II-2. List of slot cooling design parameters .....	25
Table III-1. Sensitivity analysis - heat flux.....	40
Table III-2. Phase I testing “1”: Phase II testing “2” .....	48
Table III-3. Baseline q” values and corrections w/o ramp.....	54
Table III-4. Statistical analysis - phase II data, averaged baseline values w/o ramp.....	54
Table III-5. Zero-Zero wall temperature data for all configurations .....	55
Table III-6. Statistical analysis - phase II data, averaged baseline values ramp only.....	57
Table III-7. Example Phase II – Augmentation at $y/d_j = 25$ ; .....	61
Table IV-1. Change in normalized temp with 3% increase in “h”, $\phi=1.3$ , US: Variable, DS: Normal trench.....	110
Table IV-2. Air & N2 adiabatic effectiveness at $y/d = 25$ ; US: Blank DS: Normal Trench - $\phi=1.3$ .....	113

*List of Symbols*

Symbol

A	area	Q	heat flux
atm	atmosphere	R	specific gas constant
$C_d$	coefficient of discharge	r	radius
$C_p$	Specific heat const. press.	$R_e$	Reynolds number
D	diameter	sec	second
d	diameter	q''	specific heat flux
Da	Damköhler number	T	temperature
DR	density ratio	Tu	turbulence
F	degrees Fahrenheit	U	velocity
h	convective coefficient	$V_r$	velocity ratio
I	momentum ratio	x	downstream distance
K	degrees Kelvin	Y	distance from wall
k	conductive coefficient	$\rho$	fluid density
kg	killogram	$\eta$	adiabatic effectiveness
l	characteristic length	$\phi$	equivalence ratio
$l_o$	Kolmogorov length scale	$\gamma$	ratio of specific heats
m	meter	$\alpha$	angle of inclination
$\dot{m}$	mass flow rate	$\tau$	characteristic time scale
M	mass flux ratio	$\mu$	absolute viscosity
N	number of holes	$\sigma$	standard deviation
P	pressure		
<u>Subscript</u>			
aw	adiabatic wall	f	fluid
c	coolant	j	jet
d	diameter	w	wall
s	surface	$\varnothing$	diameter
$\infty$	mainstream		

## **List of Abbreviations**

### Abbreviation

AFIT	Air Force Institute of Technology
AFRL	Air Force Research Laboratory
SLPM	Standard Liters Per Minute
TIT	Turbine Inlet Temperature
UCC	Ultra Compact Combustor
WSR	Well Stirred Reactor
US	Upstream
DS	Downstream

# **IMPACT OF TRENCH AND RAMP FILM COOLING DESIGNS TO REDUCE HEAT RELEASE EFFECTS IN A REACTING FLOW**

## **I. Introduction**

Gas turbine engines continue to provide an efficient and economical means of travel and power generation for most of the world. Significant improvements in engine efficiency, size, operational costs, emissions and engine component lifetime still exist and can provide the improvements needed to sustain future use. Component lifetime is a key area of interest especially in the engine's hot sections located near the combustor. The heat generated by the combustion process is stored in the reacting gas and transfers to the surrounding material primarily by means of convection and radiation. Hot section engine components, which come in direct contact with high temperature gas, include the combustor liner and the downstream high pressure turbine stages. Increasing the engines' gas temperature can improve engine performance by increasing thermal efficiency and specific thrust however, higher gas temperatures reduce component lifetime due to increases in thermal stress and fatigue.

Gas turbines are limited to maximum gas operating temperatures that are suitable for the materials used to keep operating costs at reasonable levels. Maximum combustor and turbine material temperatures are below the maximum possible combustion temperature for JP-8. This reduced temperature condition results in reduced engine performance. As an example, Figure I-1 shows the impact of increasing turbine operating temperature on specific power. The ideal performance line is a function of

turbine inlet temperature and depicts a 100% efficient Brayton cycle. This figure is representative of performance in a dual spool turbofan engine shown in Figure I-2.

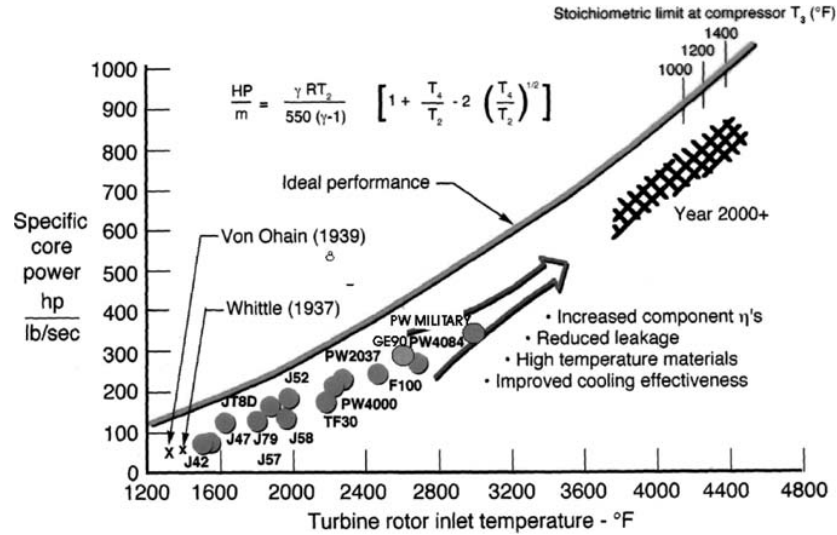


Figure I-1. Turbine inlet temperature impact on engine performance [1]

Maximum allowable temperatures along with the associated rotational and/or thermal stresses in compression, combustion, and expansion cycles limit manufacturers to specific component materials. Popular materials include nickel alloys because of their high strength properties under high temperatures and resistance to oxidation. Adiabatic flame temperatures of stoichiometric JP-8/air combustion exceed 2200 K. Oxidation occurs in most nickel alloys around 1400 K. Maintaining material integrity at high temperatures during the combustion and expansion cycles is a key focus in engine design and is the primary study of this thesis.

## **I.1 Film cooling and heat release**

Conventional cooling methods for turbine vanes, utilized in axial combustion systems, implement internal cooling channels, thin film cooling and thermal barrier coatings. The turbine blade shown in Figure I-3 demonstrates conventional thin film cooling used in high temperature turbines. The cooling air enters through the base of the blade, on the left side, and exits through the holes in the surface of the blade. After exiting the blade, the cooling air mixes with the high temperature gas near the blade surface reducing the local gas temperature. Additional heat transfers to the cooling air as it travels through the center of the blade and exits through the surface. As a result, the material surface temperature is reduced allowing for Turbine Inlet Temperatures (TIT) above the desired component material temperature.

Source air for cooling is provided by station 3, referenced in Figure I-2, which is the air exiting the high compression compressor section. Cooling air can consume as much as 20-30% of the total flow through the engine. The work needed to generate this cooling air at the pressure needed to drive flow into the mainstream turbine section reduces engine efficiency. However, there is an overall net gain in engine efficiency due to the increase in TIT provided by film cooling. Amounts of cooling air are turbine specific and depend on the desired TIT, desired material surface temperature, and the method of cooling.

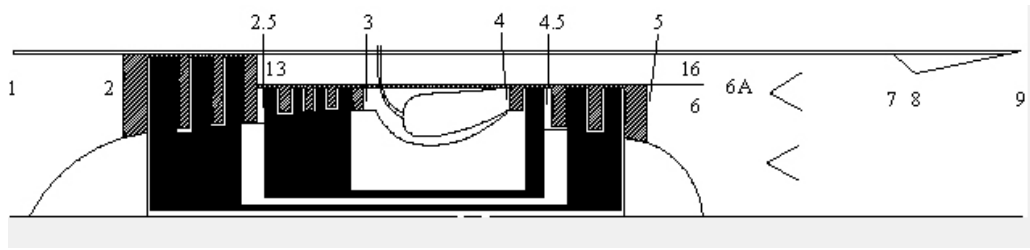


Figure I-2. Dual-spool turbofan engine with station numbers, [2]

One way to increase engine performance is to increase the TIT. This can be accomplished by raising the equivalence ratio of the combustion process. However, increasing equivalence ratio increases the heat load to the surrounding components and the probability of unburned fuel to escape the combustion section. Consequently, unburned fuel or radical species, resulting from incomplete combustion, find the oxygen rich cooling film on the surface of the turbine components resulting in secondary reactions. Completion of the combustion process near the surface of engine materials raises local gas temperature, which increases local material temperature. This condition is referred to as burning in the turbine and has become a major problem in engine design.

As provided by the following literary review, burning in the turbine is not just a combination of fuel and air. Burning in the turbine is a combination of characteristic time scales, species concentrations, blowing ratios and momentum ratios. Chemical and flow time scales can predict the probability of reactions occurring on the surface of the component. Species concentrations are a direct result of the combustion process and determine the available heat release potential in the flow. Blowing and momentum ratios produce the mixing, oxygen and local equivalence ratio necessary to facilitate near wall reactions.



Figure I-3. High pressure turbine blade

## I.2 The Ultra Compact Combustor

The Ultra Compact Combustor (UCC) is a new gas turbine combustor concept currently under development to reduce engine weight and length. The UCC uses a circumferential combustion chamber located on the outside diameter of the combustor section just before the first stage turbine rotor. The UCC has the advantage of burning in the circumferential direction as opposed to a conventional axial system.

Circumferential combustion provides an unlimited combustion length due to a continuous channel. Fuel and air enter the circumferential cavity at a high equivalence ratio. High g-loading, due to the curvature of the cavity and the fluid velocity, increases burning rates above those seen in a conventional system. As the combustion products decrease in density, they migrate to the inside diameter of the combustion channel and exit into the mainstream flow. Because of the high fuel to air ratio of the UCC combustion process, fuel or intermediate combustion products will to escape the circumferential channel. Mainstream flow provided by the high-pressure compression section, passing through the middle of the combustor channel, mixes with the high temperature gases exiting from the circumferential channel to consume the excess fuel. This environment is an ideal environment for burning in the turbine. Figure I-4 below illustrates a conventional and circumferential combustion system.

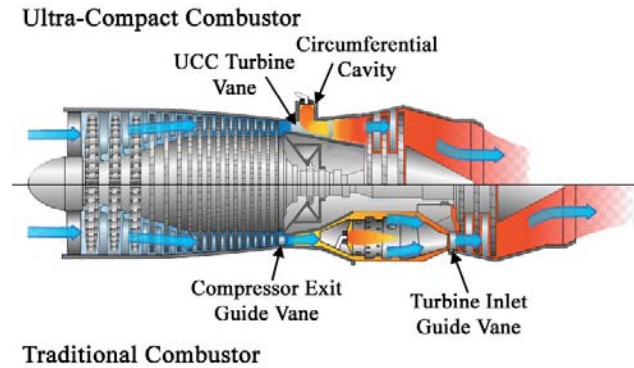


Figure I-4. Conventional and UCC circumferential cavity

As excess fuel leaves the circumferential channel, a series of vanes redirect the gas before continuing downstream. The vanes, referred to as hybrid vanes, are located directly below the circumferential combustion channel shown in Figure I-5. Flow redirection by the hybrid vane provides the inlet gas angle required by the first stage turbine rotor. The circumferential combustion cavity and the hybrid vane can shorten the combustion system by as much as 66%.

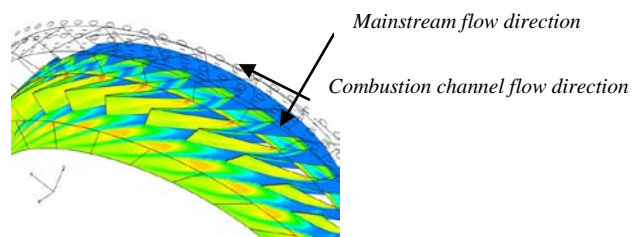


Figure I-5. UCC hybrid vane cascade, [3]

High fuel air ratio burning through the circumferential channel leaves excess hydrocarbons, carbon monoxide and other free radicals in the mainstream flow. Due to

the proximity of the hybrid vanes to the combustion channel, the reactive species exiting the circumferential cavity make burning in the turbine highly probable. Burning in the turbine must be anticipated in the design of the UCC as well as other fuel rich burning concepts. Mitigation of burning in the turbine is critical to the design and application of this fuel rich design.

### **I.3 Thesis Objective**

This thesis examines the chemical kinetic and fluid dynamic phenomena associated with burning in the turbine. Specifically, this thesis investigates different analysis methods to help compare and contrast different cooling configurations as well as identify worst-case conditions. The objective of this thesis is to identify appropriate analysis methods to find optimum and worst-case film cooling conditions. Both mitigation and identification of worst-case conditions are important to future turbine design and the future development of the UCC.

The film cooling configurations used in this investigation include a fanned, normal trench, radial trench, ramped, offset normal, and slotted. These configurations were chosen due to their relevance to current turbine application or their known relative performance. Normal cylindrical and slotted cooling configurations historically perform differently in non-reactive environments. This known difference will offer some perspective on the validity of the chosen analysis methods. The trenched configurations are relatively new designs that are used to film-cool in non-reactive environments. The fanned configuration was used in previous research by Bohan (2011) and Evans (2008)

and was found to perform poorly in reactive-flow film cooling. This investigation uses the fan to provide ideal mainstream conditions as well as for performance comparisons. The ramped configuration is a new design and is being evaluated on its performance relative to the other configurations.

The intent of this research is to learn more about film cooling in reactive flow environments. Future turbine designers must anticipate the possibility of burning in the turbine. A method of analysis and test needs to be developed to help predict what conditions contribute to burning in the turbine. This investigation is a step toward finding the tools necessary to evaluate potential film cooling strategies when burning in the turbine is probable.

Current literature provides a background in traditional film cooling, combustor design and cooling, as well as burning in the turbine. Traditional film cooling provides insight into the fluid mechanics and non-reacting environment performance. Combustor design provides current application of film cooling in combustor liners. Previous burning in the turbine research will provide information on the steps already taken in trying to solve this problem. Background information will set the stage for the subsequent analysis of test results taken as part of this investigation.

## II. Literature Review

This chapter describes the underlying physics and design theory behind thin film cooling and combustion chambers. A review of thin film cooling provides an understanding of the experimental setup and insight for the analysis of experimental results. An understanding of modern combustion chamber design provides a way forward and additional insight on experimental results. Previous studies on reactive film cooling lay the groundwork for the steps needed in this research.

### II.1 Film cooling

Reducing local gas temperature on the surface of a component reduces heat transfer potential. Shown below in the convective heat flux Equation (II-1) Newton's law of cooling, defines heat flux as being directly proportional to the convective heat transfer coefficient and the difference between the surface and fluid temperatures. The local convective heat transfer coefficient "h", measured in  $Watts/m^2 * K$ , is characteristic of boundary layer conditions including surface geometry, flow conditions, and fluid thermodynamic properties. The mainstream or driving temperature and surface gas temperatures are noted as  $T_{aw}$  and  $T_s$ , respectively.

$$q'' = h(T_s - T_{aw}) \quad (II-1)$$

Measuring heat flux is a useful film cooling analysis tool however, adiabatic performance measurements provide more detail as to the effectiveness of a particular design. Adiabatic wall temperature ( $T_{aw}$ ) represents the temperature the wall would

reach if there were no heat exchange to the surface, shown in Equation (II-2). Therefore, adiabatic wall temperature is the gas temperature directly above the wall surface if the surface were adiabatic. Because adiabatic wall temperature is a measure of free stream gas temperature above the wall, it represents the driving potential behind energy transfer between the gas and the wall. Adiabatic wall temperature provides a basis of comparison to determine the effectiveness of a cooling scheme.

Film cooling effectiveness is dependent on the difference between adiabatic wall temperature and the temperature of the ejected film cooling gas. Gas temperature at the coolant hole exit ( $T_{c,exit}$ ) is controlled by the temperature of the feed air from the compressor, stagnation potential, and heat transferred from the material to the gas while the gas is traveling through the engine component (i.e. blade, vane, combustor liner). Temperature difference between the coolant and free stream is dependent on engine operating conditions including throttle setting, component efficiencies, inlet Mach number, maximum pressure ratio, and maximum temperature at station 4. The difference between cooling and free stream gas temperature can exceed 900 K in aircraft engines operating at maximum compressor pressure ratio and maximum temperature at station 4, referenced in Figure I-2.

$$\eta = \frac{(T_{\infty} - T_{aw})}{(T_{\infty} - T_{c,exit})} \quad (II-2)$$

Table II-1 provides a list of parameters and other variables that have been proven to predict film-cooling performance or change film cooling effectiveness. Momentum and blowing ratio are the most common parameters used to predict performance. Changing the outlet shape of a film-cooling hole and the angle of the hole with respect to

the downstream surface has been proven to increase film cooling effectiveness. Surface curvature and turbulence are inherent in any film cooling application. Therefore, surface curvature and turbulence are studied to examine their effect on film cooling effectiveness.

Table II-1. Factors affecting film cooling performance (subscript “c” represents coolant, subscript “∞” represents mainstream)

Parameters	Relationship
Momentum flux ratio	$I = \frac{\rho_c U_c^2}{\rho_\infty U_\infty^2}$ (II-3)
Blowing ratio	$M = \frac{\rho_c U_c}{\rho_\infty U_\infty}$ (II-4)
Density ratio	$DR = \frac{\rho_c}{\rho_\infty}$ (II-5)
Velocity ratio	$V_r = \frac{U_c}{U_\infty}$ (II-6)
Mainstream turbulence	$Tu = \frac{u_{rms}}{U}$ (II-7)
Shape of film cooling hole	Figure II-9
Injection angle	Figure II-7
Surface curvature	Figure I-3

### II.1.1 Momentum flux

Momentum flux ratio is a measure of the coolant jet momentum compared to the mainstream momentum. Momentum ratio predicts a jet’s tendency to turn towards the surface of the blade after exiting. Coolant separation from the surface causes lower film cooling effectiveness. Figure II-1, 2, 3 illustrate the effects of a changing momentum ratio shown by Thole et al [4].

Results presented in Figure II-1, 2, 3 are respective of flat plate geometry and 35° angled cylindrical holes. The offset angle is representative of the coolant injection angle

relative to the surface. An angle of  $90^\circ$  represents perpendicular injection; an angle of  $0^\circ$  indicates parallel injection relative to the surface. Temperature controlled liquid nitrogen provides the desired fluid density to run each test case. Results indicate coolant jets remain attached when  $I < 0.4$  and fully detached when  $I > 0.8$ . When the momentum ratio is between 0.4 and 0.8 the coolant jet detaches and then reattaches further downstream. Figure II-1,2,3 demonstrate the effects of a changing momentum ratio while holding blowing ratio ( $M$ ) constant.

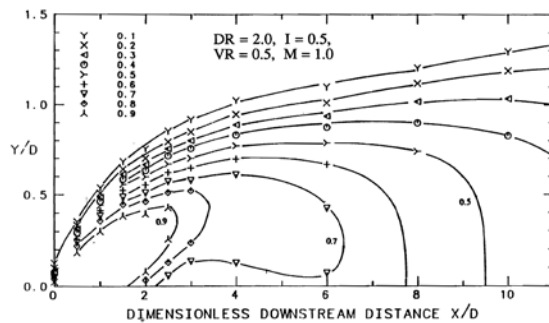


Figure II-1. Dimensionless temperature along jet centerline ( $I=0.5$ ) [4]

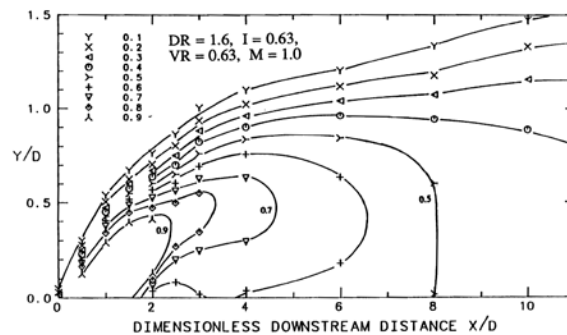


Figure II-2. Dimensionless temperature along jet centerline ( $I=0.63$ ) [4]

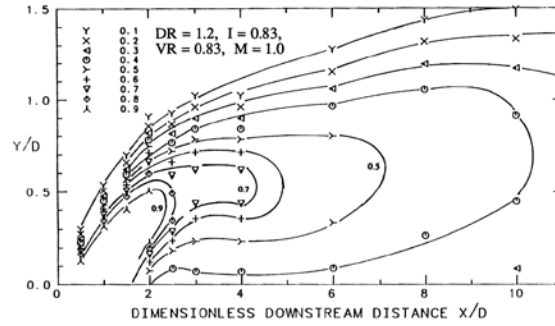


Figure II-3. Dimensionless temperature along jet centerline ( $I=0.83$ ) [4]

### II.1.2 Blowing ratio

Film cooling flows are typically defined by their blowing ratio. Blowing ratio ( $M$ ) is a function of the velocity and density ratios. Higher blowing ratios typically have a higher effectiveness in downstream locations when compared to lower blowing ratios. This is primarily due to the increase in coolant volume. Low blowing ratios produce higher effectiveness closer to the coolant exit due to a lower momentum relative to the mainstream. Several studies have shown the significance of blowing ratio on adiabatic effectiveness including Teekaram et al., [5] who used Nusselt numbers to correlate cooling performance

Teekaram's experiment uses a jet inclination angle of  $30^\circ$  and a single row of cylindrical holes on a flat plate. Teekaram's method of analysis utilizes the Nusselt number, which is a function of characteristic length, fluid conduction coefficient, and the convective heat transfer coefficient shown in Equation (II-8). Figure II-4 and Figure II-5 contain data that uses the slope ( $B$ ) and intercept ( $A$ ) of the linear Nusselt number -  $\theta$  relationship found in Teekaram [5]. The ratio of  $-B/A$  is qualitatively similar to adiabatic effectiveness.  $\theta$  represents a dimensionless wall temperature defined in Equation (II-9).

$$Nusselt \# = \frac{hl}{k_f} \quad (II-8)$$

$$\theta = \frac{(T_{t\infty} - T_{coolant})}{(T_{t\infty} - T_{wall})} \quad (II-9)$$

As indicated in Figure II-4 and Figure II-5, higher blowing ratios have better effectiveness further downstream than lower blowing ratios. Low blowing ratios produce higher effectiveness closest to the coolant exit. In addition to the effects of blowing ratio the benefit of higher density ratios also has an impact on effectiveness. Higher gas density has a higher relative effectiveness than lower gas density.

Higher coolant gas density results in a higher blowing ratio as does higher velocity. However, a higher coolant gas density at a lower velocity, to maintain the same blowing ratio, results in a lower momentum ratio due to the weight of the velocity component in the momentum Equation (II-3). Lower momentum allows the higher density coolant to stay closer to the wall. Higher density coolant closer to the surface provides better protection from mainstream gas temperature.

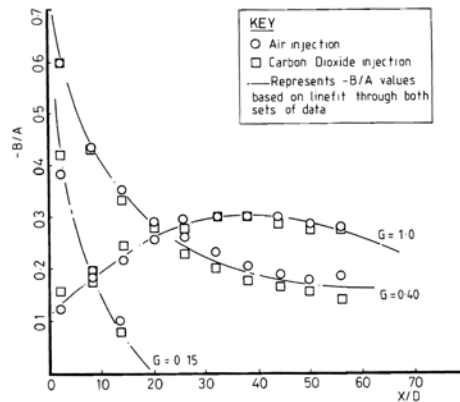


Figure II-4. Effectiveness (-B/A) with downstream distance, G=Blowing ratio, DR=1.25 [5]

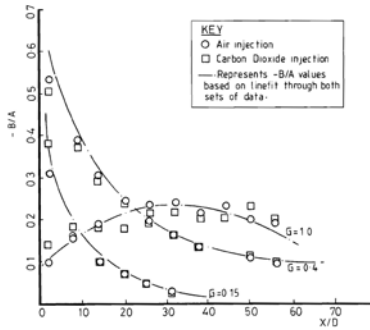


Figure II-5. Effectiveness variation ( $-B/A$ ) with downstream distance,  $G$ =Blowing ratio,  $DR=1.67$  [5]

Both momentum and blowing ratio can be used to predict film cooling performance.

Both parameters have been shown to characterize a coolant jet's performance relative to mainstream conditions. This investigation will utilize blowing ratio as the characteristic parameter.

### II.1.3 Turbulence

Increased mainstream fluid rotation near the wall's surface can increase mainstream and coolant mixing. Free stream turbulence and surface roughness both drive near wall circulation. Schmidt et al [6], examined the effects of turbulence as well as surface roughness on film cooling effectiveness. Surface roughness was used in this experiment to demonstrate the effects of a rough versus smooth surface in turbulent conditions.

Schmidt discovered that high momentum ratio coolant jets when combined with high free stream turbulence, increased adiabatic effectiveness near the coolant exit. This was due to the increase in mainstream circulation pulling coolant to the wall. Without any turbulence the jets momentum would carry the coolant off the wall and the downstream surface would be left unprotected. Schmidt's investigation also shows increased adiabatic effectiveness at high

blowing ratios when turbulent mainstream conditions are combined with high surface roughness. This is due to similar reasons however; the increased surface roughness is helping to increase local circulation increasing the probability of the coolant making it back to wall.

Low momentum flux ratios in high mainstream turbulence, reduces effectiveness substantially as shown in Figure II-6 below. Results indicate turbulent free stream conditions have a tendency to disperse low momentum jets preventing them from staying on the surface. If the coolant is quickly dispersed into the mainstream, the downstream surface will be exposed to the free stream gas temperature which decreases the adiabatic effectiveness.

Schmidt's analysis shows low momentum ratios, between 0.1 and 0.5, are optimum in low free stream turbulence conditions. Optimum momentum ratios in high free stream turbulent conditions are between 1.0 and 2.0. Note that momentum ratios between 1.0 and 2.0 equate to blowing ratios of 2 or more times higher than the optimum blowing ratio required at low turbulence levels.

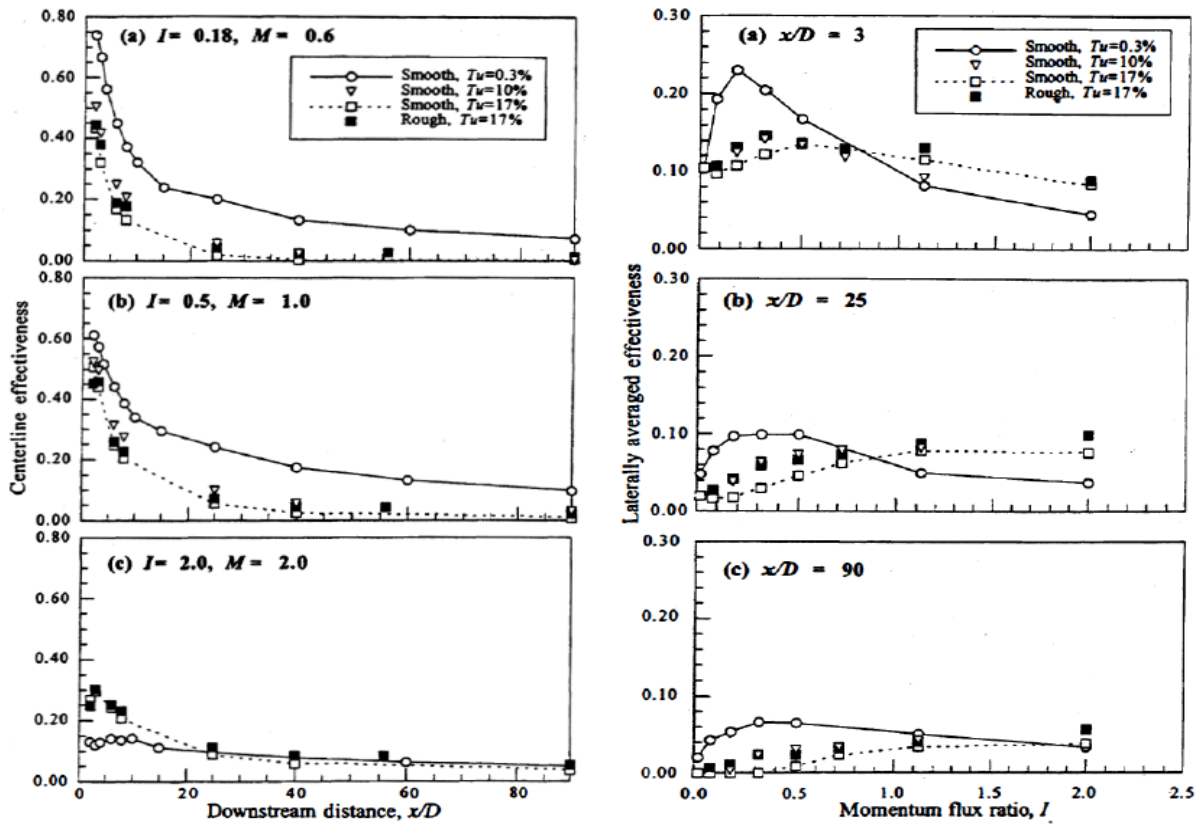


Figure II-6. Adiabatic conditions under turbulent conditions [6]

#### II.1.4 Injection angle and hole shape

Injection angle and hole shape are both significant factors in film cooling performance. Figure II-7 shows various exit geometries and hole angles tested for adiabatic effectiveness by Schmidt et al [7]. All configurations shown in Figure II-7 have the same  $35^\circ$  inclination angle in the axial direction. Two of the three hole geometries shown in Figure II-7 are compound angles due to the injection angle consisting of both a radial and axial component. Compound angle holes have a significant advantage over other angle geometries due to their ability to spread the coolant in the spanwise direction. With the addition of a forward expansion and small hole to hole spacing (pitch), the overall cooling effect of compound geometry can look like that of a slot.

Results obtained by Schmidt et al [7] shown in Figure II-7 demonstrate the advantages to compound angle geometry. Case (a) of Figure II-7 shows a cylindrical round hole inclined  $35^\circ$  in the axial direction. Results of case (a) show high centerline effectiveness decreasing quickly with increasing spanwise distance. Case (b) shows results from a  $60^\circ$  compound angle hole. Results of case (b) show a right skewed high effectiveness due to the coolant being pushed to the right of the exit. Case (c) shows a  $60^\circ$  compound angle exit with forward expansion. The effectiveness profile is much flatter in case (c) at every downstream distance. Case (c) proves the advantage of compound angle injection in film cooling when compared to cases (a) and (b).

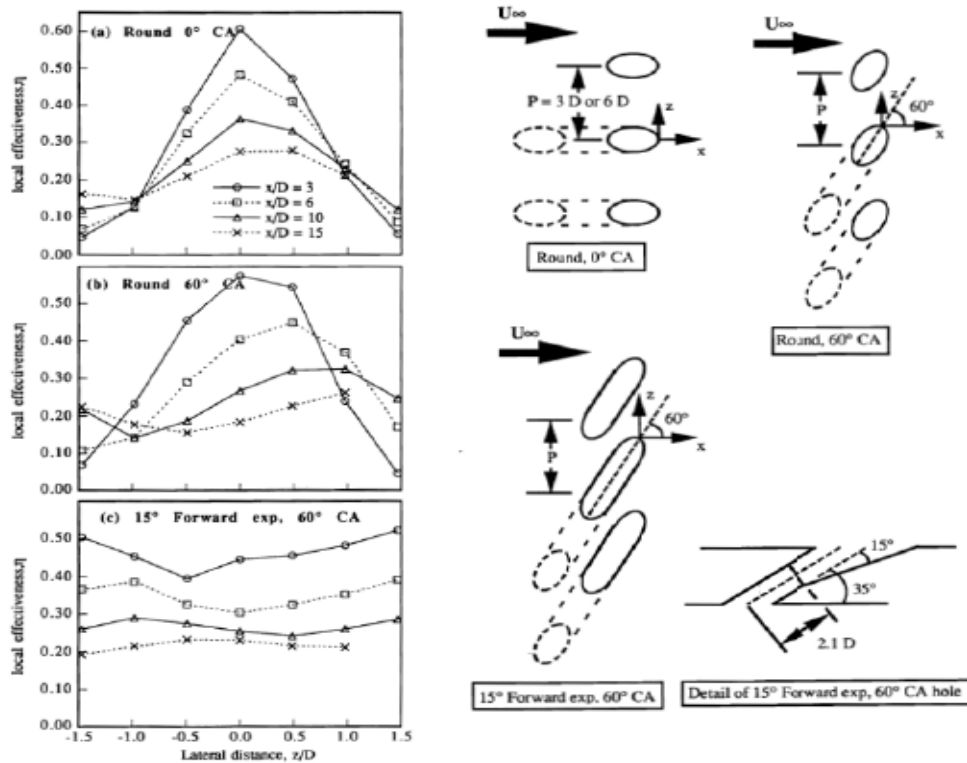


Figure II-7. Cooling hole geometries and effectiveness results [7]

Gritsch et al [8], conducted testing on expanded exit hole geometry to find potential performance improvements to adiabatic effectiveness. Expanded exits have the ability to diffuse

the coolant before entering the mainstream. Expanding in the spanwise direction is commonly referred to as fanning. Figure II-8 shows several cooling hole geometries including cylindrical, fan shaped, and laidback fan shaped.

Results shown below in Figure II-9 are 2-D effectiveness contour plots. The benefits of the laidback fan shaped hole are apparent and demonstrate the ability to keep the fluid close to the surface even at high blowing ratios. Fan shaped holes have the advantage of injecting larger quantities of mass into the mainstream without high momentum and separation from the wall.

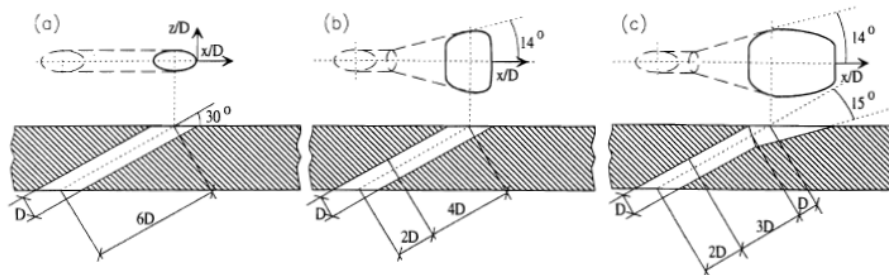


Figure II-8. Cylindrical, fan shape, laidback fan shape configurations [8]

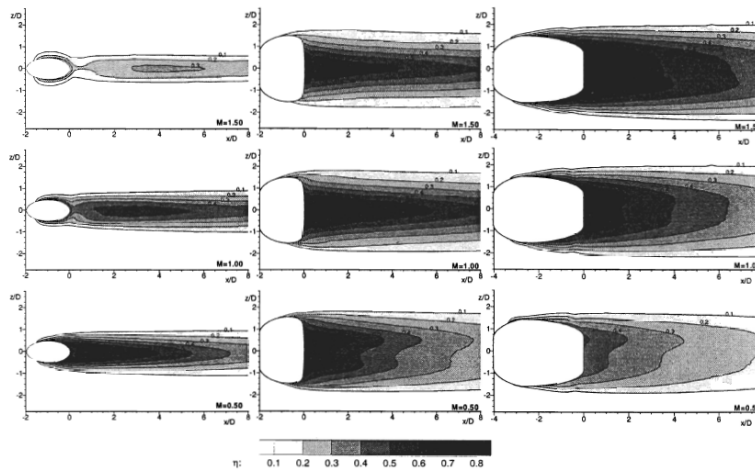


Figure II-9. 2-D adiabatic effectiveness contours[8]

### II.1.5 Surface curvature

Each of the previously reported results shows performance on a flat surface. Surface curvature has the potential to impact cooling performance due to the presence of pressure

gradients in the flow. Radius of curvature of the blade or vane surface influences pressure gradients created by the mainstream gas. Pressure gradients are balanced by the centrifugal forces in the fluid as the fluid accelerates through the curve. Equation (II-10) represents the equality between pressure and centrifugal forces where  $r_w$  is the radius of curvature of the wall and  $U_\infty$  is the velocity of the mainstream. A jet injected into the mainstream follows the same principle, shown in Equation (II-11).

$$\frac{dP}{dr} = \rho_\infty \frac{U_\infty^2}{r_w} \quad (\text{II-10})$$

$$\frac{dP}{dr} = \rho_j \frac{U_j^2}{r_j} \quad (\text{II-11})$$

Ignoring dynamic pressure effects on the jet that tend to push the jet closer to the wall, we find the equality shown in Equation (II-12). Therefore, the momentum ratio between the jet and mainstream is proportional to their respective radii of curvature. To achieve higher effectiveness, the coolant must remain attached to the wall. In the case of a convex wall, where the radius of curvature is positive from the inside of the wall to the outside of the wall, the jet's radius of curvature must be smaller than the wall's radius of curvature. The case of a concave wall requires the opposite relationship where the jet's radius of curvature must be greater than the wall's radius of curvature to stay attached to the surface.

$$\frac{r_j}{r_w} = \frac{\rho_j U_j^2}{\rho_\infty U_\infty^2} \quad (\text{II-12})$$

Experiments run by Ito et al [9] demonstrate this relationship using mass transfer principles. An injection angle, referred to as  $\alpha$ , of  $90^\circ$  indicates perpendicular injection and  $0$

indicates parallel injection. The momentum ratio shown in Equation (II-12) represents the momentum ratio of the jet and mainstream in the direction of the mainstream gas. Therefore, the momentum ratio must be modified to account for  $\alpha$  by replacing  $U_j^2$  with  $(U_j \cos \alpha)^2$ . Film cooling effectiveness on a convex wall is better than on a concave wall if  $I \cos^2(\alpha) < 1$  and worse if  $I \cos^2(\alpha) > 1$ . Figure II-10 below shows the variation in lateral effectiveness with  $I \cos^2(\alpha)$  and a density ratio of 0.95 taken from Pederson et al [10]. The variable  $\frac{x}{D}$  represents normalized distance from the point of injection.

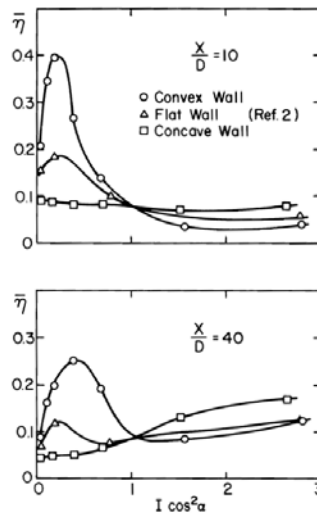


Figure II-10. Variation of lateral average effectiveness[10]

## II.2 Combustor design

Annular combustion systems are currently the mainstay of gas turbine engine design. Annular systems evolved from previous can and can annular designs. Figure II-11 and Figure II-12 show a J79 can combustor and an illustration of an annular combustion chamber, respectively. Annular combustion systems are designed using a head wall (dome), inner liners

and outer liners. Annular systems are not separated into individual chambers, like the can system. Instead, annular systems are a continuous combustion chamber that revolves around the centerline axis of the engine. The main purpose of the liner and dome are to contain and guide the fuel-air mixture from the fuel injector to the turbine inlet nozzle. Additionally, the liner and dome control airflow to the different zones within the chamber and protect the surrounding structure from the high temperature gas.

Withstanding high temperature environments is challenging and extremely important to the longevity of the combustion system. Peak gas temperatures can reach as high as adiabatic flame temperatures of the fuel used. Gas temperatures in a combustor operating at 30 atmospheres, with an inlet temperature of 800 K, can exceed 2500 K as shown by Mattingly (2002), [2]. Nickel alloy materials offer the best oxidation resistance and can sustain operation up to 1150 K. Liner materials oxidize above 1400 K and melt above 1550 K which is also shown by Mattingly (2002), [2]. Maintaining temperatures below 1150 K demands a large cooling air supply. However, cooling air is in short supply due to the demand for reduced pollution and higher efficiency engines.

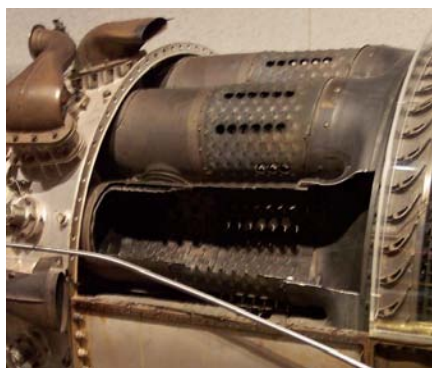


Figure II-11. J79 combustor can

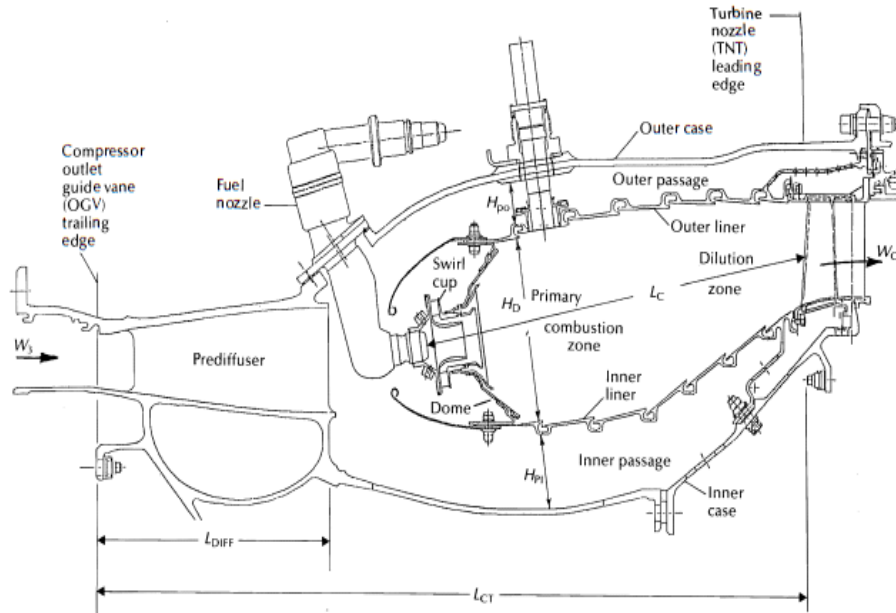


Figure II-12. Annular combustor illustration (GE CF6-80C)

Louvered liners, like those shown in Figure II-11, are fabricated using sheet metal perforated with a series of indentations. The amount of cooling airflow is controlled by the gap between the elevated surface and the surrounding surface and the pressure difference through the liner. Manufacturing tolerances make this method undesirable due to the unpredictable impacts of uneven coolant distribution on the interior of the liner as shown by Mellor (1990), [11]. Additionally, stress concentrations on the sheared surface are prone to cracking after prolonged cycle time. Louvered liners are no longer used in modern combustor designs due to these known flaws.

Cooling slots prevail in the majority of current combustor designs. Placed in intervals in the axial direction, cooling slots provide a thin layer of cooling air to protect liner walls from the high temperature gas as shown by Mellor (1990), [11]. Figure II-13 shows various slot cooling configurations. Each hole feeding into the slot, except for the wiggle strip, is drilled or laser cut

in sequence along the spanwise direction of the slot. Slot types a-d in Figure II-13 are manufactured using sheet metal that is brazed or welded together. Brazed or welded joints have the potential to trap gas or create small voids known as porosity. As a result, local hot spots and stress concentrations form and shorten the lifespan of the joint. Slots, machined from one piece or cold rolled into shape, have significant structural advantages like those shown as e-g. Slot types e-g are more difficult to manufacture however, they provide increased structural integrity.

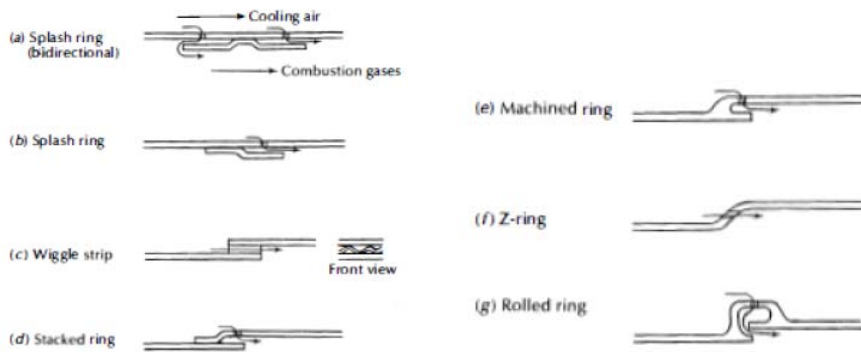


Figure II-13. Various slot configurations [11]

Liner construction and cooling methods are dependent on expected component lifetime and operational temperatures. Burrus et al [12], provides initial estimates of coolant flow for combustor liner cooling at approximately  $0.75 \frac{kg}{sec * m^2 * atm}$ . This is only an estimate but it provides a starting point in the design process. One can approximate the cooling hole exit area required using the above specified mass flow in combination with density, discharge coefficient and liner pressure drop shown in Equation (II-15). Equation (II-13) provides the number of holes required assuming one knows the optimum hole area required for their particular design. Hole diameters range from 0.5 – 2.5 mm; typically hole sizes near the bottom of this range are

better due to the increase in surface area resulting from an increased number of holes to meet total hole area in Equation (II-13).

Discharge coefficient ( $C_d$ ) is approximated at 0.8 for initial estimates. Discharge coefficient is a percentage of theoretical airflow based on Bernoulli's principle of incompressible flow.  $A_2$  is the hole entrance area,  $P_1$  and  $P_2$  are the upstream and downstream pressures, and  $d_1$  and  $d_2$  are the mainstream diameter and the hole entrance diameter respectively. Hole diameter, liner metal thickness and passage cross flow direction relative to hole entrance all affect discharge coefficient. The incompressible assumption limits application of Equations (II-13) and (II-15) to liner pressure drops between 3-5% of inlet pressure due to the increasing significance of compressibility.

$$A_{hole} = \frac{\dot{m}}{C_d * \sqrt{2 * \rho * \Delta P}} \quad (II-13)$$

$$d_{hole} = \sqrt{\frac{4 * A_{hole}}{\pi * N_{hole}}} \quad (II-14)$$

$$\dot{m} = A_2 C_d \frac{\sqrt{2\rho(P_1 - P_2)}}{\sqrt{1 - \left(\frac{d_2}{d_1}\right)^4}} \quad (II-15)$$

The above design criteria provide a starting point and do not encompass all slot cooling design variables. Other parameters include but are not limited to hole pitch, angle of injection into the slot-mixing chamber, slot exit area, coolant velocity and stream wise mixing length. Figure II-14 shows a schematic of some of the design parameters considered when designing a slot cooled combustor liner. Table II-2 lists each design parameter and its associated notation.

Table II-2. List of slot cooling design parameters

Notation	Dimension
$\delta_w$	Lip trailing edge thickness
S	Slot outlet height
$A_s$	Slot outlet area (geometric)
$U_H$	Coolant velocity from axial holes
$V_H$	Coolant velocity from normal holes
$A_H$	Total coolant metering area
$\theta$	Angle of axial metering holes to cooled wall
D	Height of mixing chamber at coolant inlet
D	Metering port diameter
P	Metering port pitch (axial/normal)
L	Mixing chamber length
$\epsilon$	Downstream position of leading edge of impingement

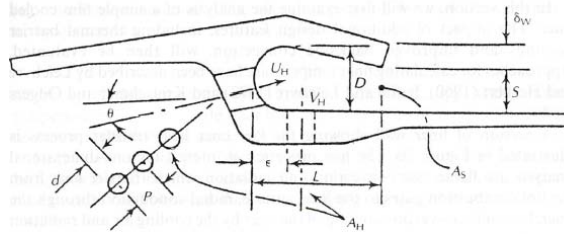


Figure II-14. Slot parameter diagram [13]

### II.3 Perpendicular jet injection

Perpendicular jet injection used in modern combustor design increases reaction rates as shown by Lilley [14]. Reactions come to completion faster as mainstream mixing and turbulence increases due to the interaction between the perpendicular jet and mainstream fluid. Without the additional mixing due to the perpendicular jet, reactions in the combustor would

take longer to complete also shown by Lilley [14]. The amount of turbulence and mixing generated is dependent on jet velocity, momentum ratio, and injection angle. Perpendicular jets are also useful for producing areas of recirculation providing an area for reactions to stabilize.

Jet velocity, momentum ratio, and injection angle affect the jet's trajectory into the mainstream flow. Several studies including Lilley [14], have provided relationships, like the one shown in Equation (II-16), which describe the position of the jet using momentum ratio and jet diameter. Maximum jet height is found by solving (II-16). Sine  $\theta$  is added to the equation as a modifier to momentum ratio as the jet injection angle changes the component of the jet velocity relative to mainstream velocity.

$$Y_{\max} = 1.15 * d_j * I^{0.5} * \sin(\alpha) \quad (\text{II-16})$$

As each jet penetrates into the mainstream, the high-pressure stagnation point on the upstream side of the jet and the opposing low-pressure area on the downstream side of the jet push the jet towards the wall. The opposing pressure zones, additional oxygen, and mixing created within the mainstream enhance the combustion process. Modern combustors use perpendicular jets within the primary and intermediate combustor zones to increase reaction rates. Perpendicular jets are also used in the dilution zone to reduce and evenly distribute gas temperature before the mainstream leaves the combustor cavity, shown in Figure II-15.

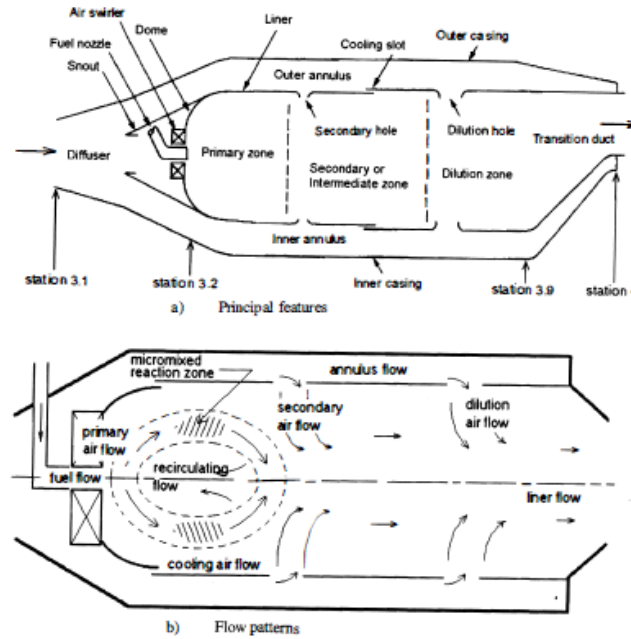


Figure II-15. Lateral jet injection into combustion chamber [2]

## II.4 Reaction rates and potential heat release

Several studies have shown the impacts of different film cooling geometries in reacting flows. One study in particular, performed by Polanka et al [15], included an experimental and computational investigation on the effects of three different cooling geometries in reacting flows. Configurations included rows of normal cylindrical, angled cylindrical, and laidback fanned shape holes. In these investigations, fanned holes perform better than the other two configurations in a non-reacting environment due to little to no separation and the ability of the jet to spread in the lateral direction. However, fanned holes perform the worst and have the highest heat flux augmentation to the wall in a reacting environment. This is attributed and shown by Stouffer et al [16], to be the result of reactions occurring near or on the surface of the wall increasing local gas temperature and heat flux to the surface. The fanned configuration allows reactions to occur over a wider region and closer to the surface. This is due to the same

reasons that make this a beneficial configuration without reaction, namely lower jet separation and higher lateral spreading than the other geometries.

Lin et al [17], characterized the species present downstream of a fan shaped hole in a reacting flow. Results were obtained computationally to find temperature profiles, CO<sub>2</sub>, CO, and C<sub>3</sub>H<sub>8</sub> concentrations at various downstream distances. In Lin's study, the conversion of CO and remaining C<sub>3</sub>H<sub>8</sub> to CO<sub>2</sub> accounted for the heat release mechanism. Due to the close proximity of the coolant ejection from the fanned holes, this chemical reaction occurred very near the surface. This investigation also revealed that increasing the blowing ratio can elevate the secondary combustion zone higher above the flat surface decreasing additional heat transfer to the surface. While this does not reduce the extent of the reaction, it does shift where the reaction occurs. This can be an alternative for mitigation of the impact of heat release in turbines.

Studies performed by Bohan [3], represent the first investigation into the effects of series injection on downstream heat flux. Series injection includes an upstream coolant ejection and a second downstream coolant ejection. In this study fan shaped holes were used in the same test rig as built and described by Evans [18], however two different injection geometries were inserted into the upstream location including an offset normal and slotted geometry. Results show a small reduction in heat flux when using the offset normal in the upstream plenum compared to fan only results. This suggests an effect of reducing the local equivalence ratio by injecting coolant in series. Slot cooling proved to be the better of the two upstream series inputs tested producing zero heat flux augmentation under certain test conditions. Additionally, Bohan determined flame ignition location was constant and did not change with increases in blowing ratio. This led to an understanding of the consistency of the characteristic flow and chemical times associated with the ignition process.

The Damköhler number establishes when flames can be sustained in a particular location. Sustained burning in the turbine is possible when the appropriate characteristic flow and chemical time ratios result in a Damköhler number, shown in Equation (II-17), greater than one. Gas temperatures predominantly determine these chemical times as shown by Waitz et al [19] and Lukachko et al[20]. With the onset of increasing combustion temperatures, there is an increasing chance for favorable Damköhler numbers and burning in the turbine.

Lukachko shows an increasing chance of secondary reactions when combustor temperatures increase due to the decrease in characteristic chemical time. Lukachko imposes increasing pressure and temperature on a fuel air mixture in a simulation program to show increasing Damköhler numbers. As temperature increases the resulting characteristic chemical time decreases resulting in an increased Damköhler number. Ultimately, burning in the turbine will become an increasing problem as designers push for higher efficiency by increasing combustor temperature.

Lukachko also explains the potential relationship between adiabatic effectiveness and local equivalence ratio. His research indicates that as adiabatic effectiveness decreases the local equivalence ratio between oxidizer (coolant) and reactive species (predominantly carbon monoxide) increases. Lukachko explains the potential for a threshold adiabatic effectiveness required for additional heat release. Note that centerline adiabatic effectiveness is not synonymous with averaged or lateral effectiveness. This means that at any point in the jet – mainstream interface where the threshold equivalence ratio is reached, a secondary reaction can occur.

$$Da = \frac{\tau_{\text{flow}}}{\tau_{\text{chem}}} = \frac{l_o}{u_{\text{rms}} \tau_{\text{chem}}} \quad (\text{II-17})$$



### **III. EXPERIMENTAL SETUP**

#### **III.1 Test Setup**

This chapter contains the experimental methodology, test setup, and experimental setup analysis used to characterize testing conditions. Testing was within Test Cell 153 located in building 490. This facility is managed by the Combustion Branch of the Propulsion Directorate at Wright Patterson Air Force Base. This research follows similar research conducted by Capt Brian Bohan and Navy LT David Evans. Bohan and Evans used the same test rig and set up as used in this investigation. Their documents contain more detail on the specifics of the test set up than will be explained in this section. However, a brief overview of the test rig and test methodology will be presented in this section to provide the details required to understand the following investigation. Additional information can be found in Bohan's thesis [17] as well as Evans's thesis [18]. Detailed setup and design specific details of the well stirred reactor are explained in the reference provided by Stouffer et al [15]. In addition to this information, Appendix A contains drawing details of the cooling configurations under investigation.

The Well Stirred Reactor (WSR) exhaust fed a flat plate test section fitted with two cooling slot bays and nine thermocouples as shown in Figure III-1. One thermocouple is located at the entrance to the test section to determine the entrance reacting flow gas temperature. Eight more thermocouples were placed downstream of the cooling bays in the flat plate at different depths from the surface. Four thermocouples are located 4mm from the surface to measure shallow temperatures. Four more thermocouples are directly behind the shallow thermocouples at 19mm from the surface to measure deep temperature. Each thermocouple location (A,B,C,D) holds two thermocouples, shallow and deep, which provided a direct calculation of the heat flux

through the wall when using material conduction properties for Hasteloy-X. Equation (III-1) shows the details of the calculation used to find heat flux at a downstream location, reference Evans [18].

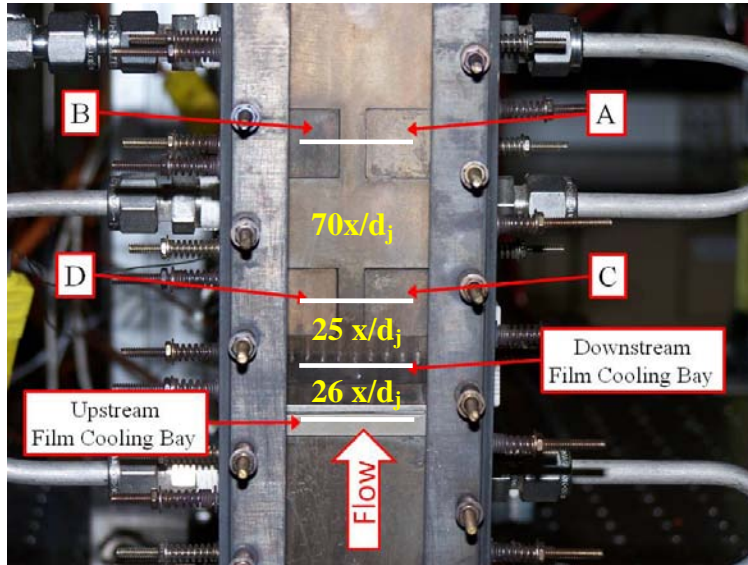


Figure III-1. Front view of test rig

Air and propane are injected into the WSR where they react before traveling downstream to the test section. Air and fuel are injected with a radial velocity component into the reactor to promote mixing and combustion. The reactor is made of ceramic material and encloses the air and fuel injector ring described by Stouffer [15]. Figure III-2 shows the partial assembly layout of the reactor core and housing. The combustor outlet temperature and fuel species concentration present in the WSR exhaust is dependent on equivalence ratio in the WSR. Changing the equivalence ratio requires manipulation of the fuel and air mass flow into the reactor. Manipulation of fuel and air mass flow are controlled by calibrated flow meters displaying flow rate in Standard Liters Per Minute (SLPM) as described by Evans [18].

After air and fuel mix and exit the combustor core, they travel through a flow conditioning section. Flow conditioning must take place to reduce the swirl velocity component

due to injection and transition from the circular combustor outlet to rectangular test section inlet. To reduce the impact of swirl in the test section, flow straighteners are placed between the reactor outlet and the test section inlet. A flow straightener is a ceramic insert placed in the transition section of the test setup shown in Figure III-3. A picture of a flow straightener is included below in Figure III-4. Bohan [17] describes several designs and an analysis of each flow-straightening scheme used in this experiment. Two different flow straighteners were used to conduct this investigation. Bohan depicts the first straightener, used during the first phase of testing, as design 5. Design 4 was used during the second phase. Both designs reduce swirl in the flow to help ensure a vertical mainstream once entering the test section. The transition/flow straightener section contains two straighteners. The first is located near the combustor outlet with the second placed just above the first.

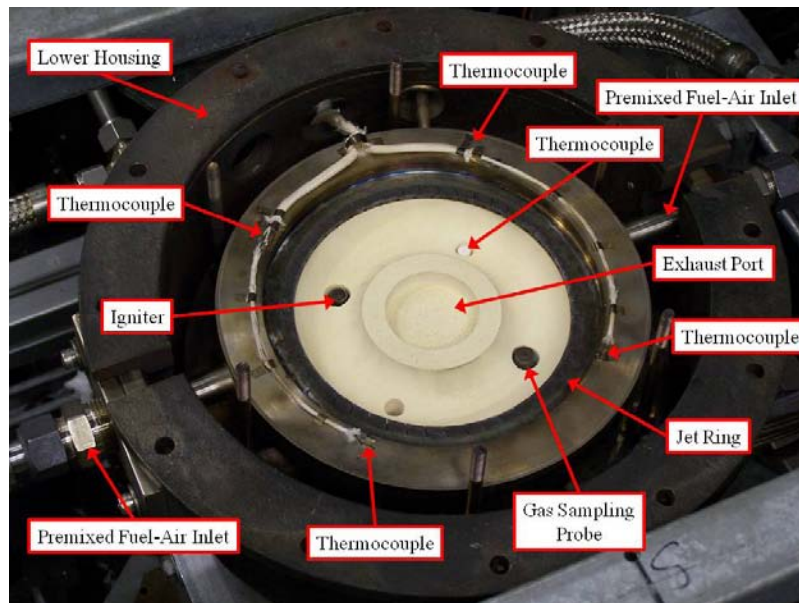


Figure III-2. Lower half of reactor core with jet ring inside WSR housing

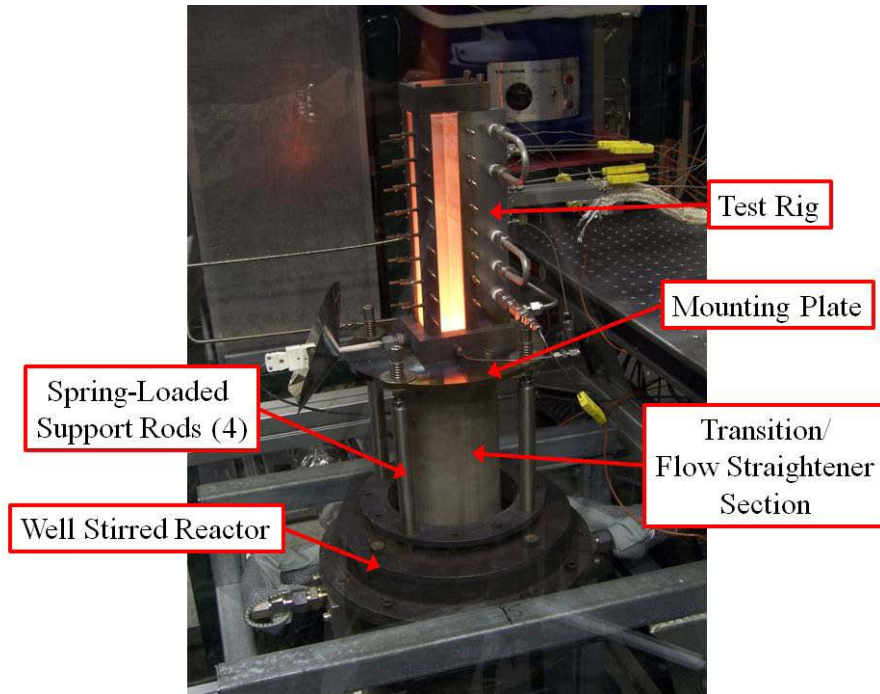


Figure III-3. Experimental test setup

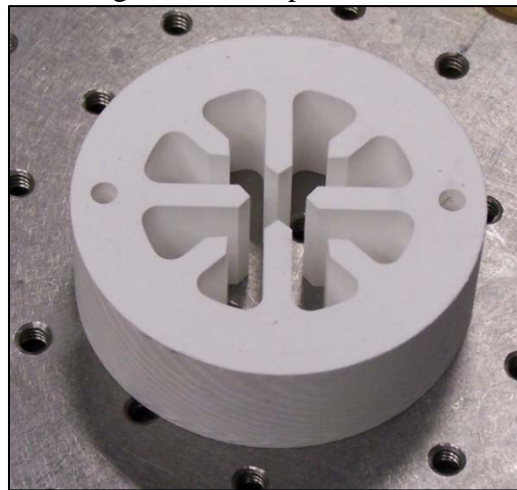


Figure III-4. Flow straightener

Also shown in Figure III-3 are the u-shaped cooling tubes running in to and out of the backside of the test plate. These tubes circulate the coolant from top to bottom cooling the backside of the test plate to maintain reasonable material temperatures during testing. Water or oil can cool the test rig depending on the results desired. AFRL facility water is supplied

through a Dwyer model RMC-141-SSV flow controller to provide the desired cooling. Oil is provided by a MOKON model HC 4118-RC control unit, which provides heated oil at a specific outlet pressure.

Water was used as the cooling fluid during phase I of testing. The Dwyer flow meter is dialed to indicate 0.5 gallons per minute during testing. Water inlet temperature to the test rig is uncontrolled however; it remains constant around ~65 F. Water inlet pressure is dependent on the other systems in the building using the same water supply. However, the gage indicated flow rate is recorded periodically during testing to ensure the water flow rate is consistent.

Oil cooling is used in phase II of testing because of the potential error associated with various water coolant inlet temperature and pressure conditions. Oil is supplied to the test rig at an outlet pressure of 89 psig at a temperature of 300 F. When the pump is running steady state at a constant outlet pressure and temperature the mass flow through the test section is constant. This same oil pressure and temperature is maintained from condition-to-condition and day-to-day to ensure minimal error in results due to varying coolant conditions. Further heat sink analysis is provided in section III.3.

## **III.2 Test method**

Test methods are presented in the previous two theses by Bohan [17] and Evans [18]. The test method used to conduct experimentation for this thesis follows a similar format. Procedures described were conducted on every test day except where noted. General methodology on when to take data and what defines steady state test conditions is consistent throughout all experimentation.

Equation (III-1) is used to calculate heat flux at any given test condition. The numerator uses conductive coefficients  $a_1$  ( $0.0197 \frac{W}{mK^2}$ ) and  $a_0$  ( $3.7164 \frac{W}{mK}$ ) of Hastelloy-X, [21] as well as shallow ( $T_1$ ) and deep ( $T_2$ ) temperatures to calculate the heat flux at a particular downstream location (A,B,C,D). The denominator contains the distance between the two temperature measurement points  $x_1$  and  $x_2$  which are 4.0 and 19.0 mm, respectively. Because we are using calculated heat flux as our analysis tool, one must be confident the test rig has reached equilibrium at the particular test condition.

$$q'' = \frac{a_1/2 * (T_1^2 - T_2^2) + a_0(T_1 - T_2)}{x_1 - x_2} \quad \text{(III-1)}$$

A real time temperature trace of each thermocouple is available on a LabVIEW® user interface located on the local computer in the test lab. The temperature trace of each thermocouple is tracked until the user is satisfied that the steady state response has been reached. Data is taken continuously by the LabVIEW® program leaving the user to decide the appropriate time frame, of recorded data, to consider for the given test condition. Figure III-5 shows an example data sheet that contains a series of test conditions. Test conditions run down the sheet from row to row; test condition variables run left to right from column to column. As each test condition is completed, the mass flow, blowing ratios, equivalence ratios and the test points, corresponding to the recorded data, are recorded. The far right hand of the test sheet shows pressures and temperatures of the oil cooling system's outlet conditions. Oil outlet conditions are the conditions feeding the heat sink on the back of the test plate during the second phase of testing.

The test setup used to create Figure III-6-7 include: the offset normal configuration in the upstream bay and the normal bay trench in the downstream bay. Mainstream conditions are at an equivalence ratio of 1.3 with blowing ratios in the upstream bay transitioning from 3.0 to 7.0. Downstream blowing ratio is held constant at 2.0. Total time for step response to complete before taking data was limited to ~ 6 min as shown by the horizontal axis in Figure III-6. The zero point on each time scale shown in Figure III-6,7 and 8 represents the beginning of the step response.

Figure III-5. Example test spread sheet – Phase II, normal trench – Dec-15-2011

Before taking data on a particular test day the WSR is heated for about an hour to allow the test setup to warm to steady state conditions. Steady state mainstream conditions for any given test day is around 2700 F (1760 K) on the mainstream thermocouple. This temperature is

achieved at an equivalence ratio of 1.3. Once the author was satisfied the rig had reached a steady state condition, about an hour after start up, testing begins. Each test point changes the temperature of the wall and the thermocouples behind it. Sufficient time must be provided for the plate to communicate the temperature change from the flame side surface to the back of the test plate. The amount of time required is dependent on the magnitude of the temperature change. Changing from an air-cooled condition to another air-cooled condition takes around 5-10 minutes. Changing from an air-cooled condition to a nitrogen-cooled condition can take up to 15-20 minutes depending on the previous air-cooled blowing ratio. This is because higher air-cooled blowing ratios typically produce higher wall temperatures

Steady state can be difficult to determine due to the nature of a step response. One must make a determination as to when steady state is reached. Therefore, steady state is defined in terms of a temperature rate of change, 1 degree F per minute, or when a 95% response has been reached. The following analysis uses both criteria to determine when steady state is reached. An example is used to show actual data taken during testing.

The following example explains the importance of both criteria and is somewhat experienced based. Figure III-6 shows a temperature time trace on the C-shallow thermocouple. Time at zero seconds represents the beginning of the step response. In Figure III-8, the rate of change in temperature went below 1 degree F per minute around 100 seconds leaving another one degree F of temperature change. In some cases, successive test conditions vary by 1 degree F. As such, the determination of steady state is a combination of both the timed response of temperature change as well as an experience-based determination of the 95% response. Steady state for each condition is held for at least one minute, data is recorded every two seconds

resulting in 30 data points in one minute. This provides a reasonable amount of data to represent a given condition.

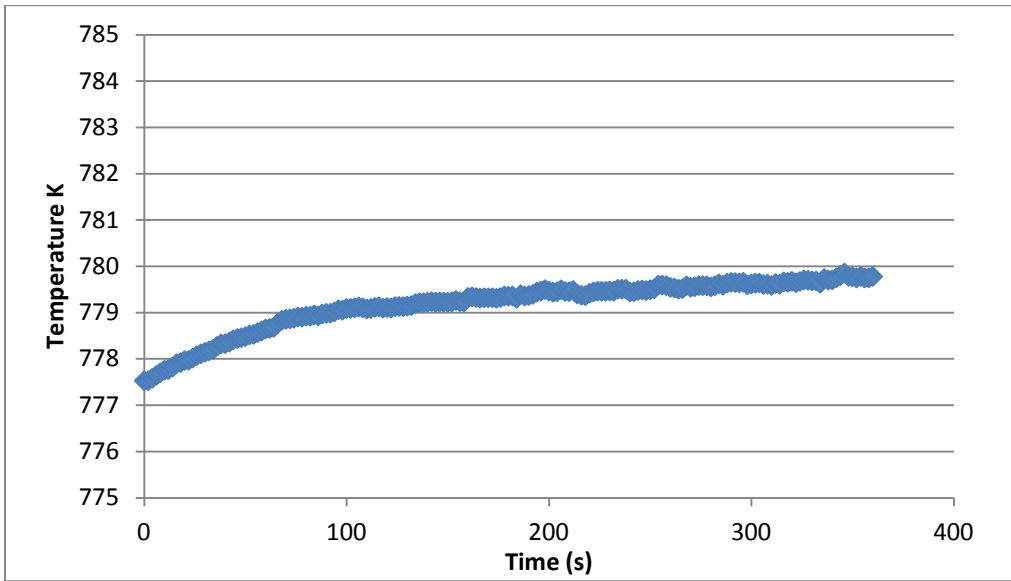


Figure III-6. Phase II - Time response - C shallow thermocouple –  $\phi=1.3$  US: Offset normal DS: Normal trench

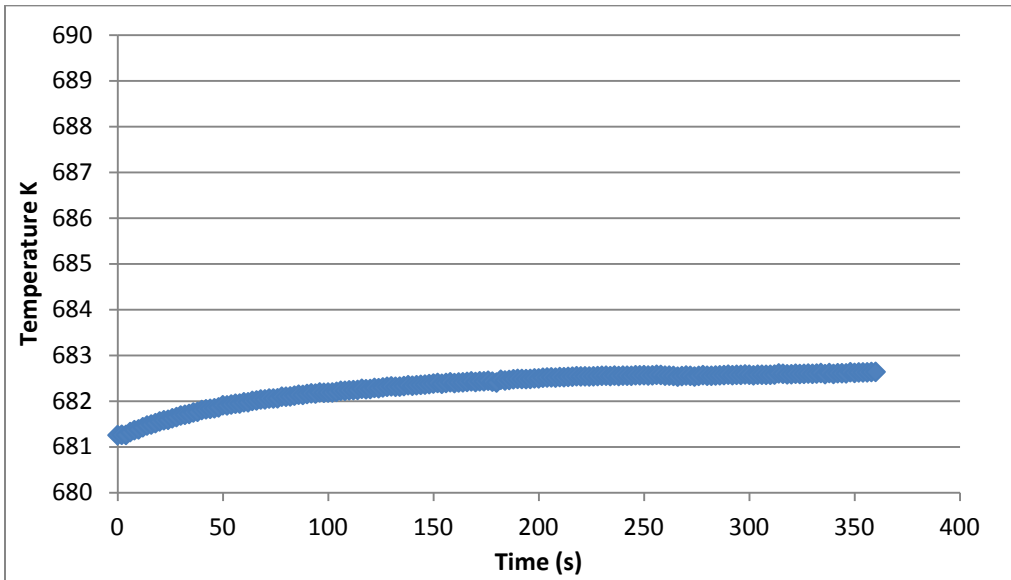


Figure III-7. Phase II - Time response – C deep thermocouple –  $\phi=1.3$  US: Offset normal DS: Normal trench

The dominating factor in Equation (III-1) is the difference of squares in the numerator. For example, a shallow temperature measurement of 777 K (940 F) and a deep temperature measurement of 681K (766F) result in a heat flux of  $116075 \frac{W}{m^2}$ . Even though the  $a_1$  coefficient is smaller by two orders of magnitude when compared with  $a_0$ , the first term in the numerator takes up 67.1% of the calculated heat flux. This is significant to note before taking data due to the sensitivity of the difference in temperature.

To demonstrate the significance in temperature change, Table III-1 shows the consequence of taking data too early. Example data is representative of the test case shown in Figure III-6 and Figure III-7. Data is shown in 100 second intervals to demonstrate changes in heat flux. Temperature data is shown in degrees K although temperature is tracked in English units during testing. Ultimately, error is represented as a percentage of the initial value at the beginning of the step response, therefore the percent change in Table III-1 at time zero is equal to zero.

Table III-1.Sensitivity analysis - heat flux

Time	T(1) F	T(1) K	T(2) F	T(2) K	q" W/m <sup>2</sup>	BTU/sec*ft <sup>2</sup>	% change
0.00	939.88	777.53	766.59	681.26	116075.10	36880.96	0.00
100.00	942.69	779.09	768.27	682.19	116993.67	37172.82	0.79
200.00	943.37	779.47	768.82	682.50	117117.90	37212.29	0.90
300.00	943.64	779.62	768.97	682.58	117220.94	37245.03	0.99

Taking data too early creates an error due to the magnitude of change in heat flux from the beginning of the step change to the end of the step change. For example, if a one percent difference exists from beginning to the end of the step response and the user takes data too soon (100 seconds), the calculated heat flux is off by 0.2% where the total change is only 0.99% (300 seconds), as shown in the right hand column of Table III-1. Although this may seem insignificant, this error increases as the percent change in heat flux from the beginning to the end

of the step response increases. Additionally, this example test case does not reach steady state conditions as indicated by Figure III-8. However the rate of change in temperature, shown in Figure III-8, reaches near zero values around 300 seconds indicating the step response has neared its completion. The author advises that any future experiments use a more refined temperature time to respond method. Without experience, one can assume 10 minutes for changes between blowing ratios while using the same cooling fluid and 20 minutes when changing between cooling fluids. The time required to reach steady state after changing the equivalence ratio in the reactor can take up to 45 minutes.

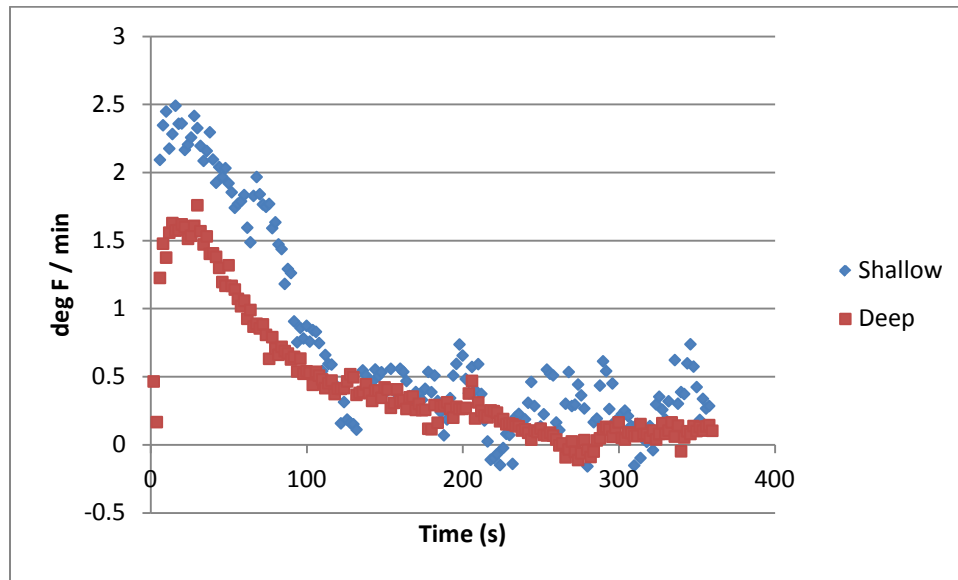


Figure III-8. Time rate of change in temperature - C deep & shallow thermocouple –  $\phi=1.3$  US: Offset normal DS: Normal trench

### III.3 Heat sink

A heat exchanger, located in the back of the test plate, maintains wall temperatures below 900 K. Figure III-1 shows several cooling channels that route cooling fluid through the backside of the plate removing additional heat beyond free convection and radiation. The amount of heat

removed is dependent on the fluid used, mass flow rates, temperature differences, and convection coefficients between the cooling fluid and the tube running through the plate. Two separate phases of testing allows one to separate the use of two different heat exchanger coolants. Specifically, phase I testing uses water and phase II testing uses oil as the cooling fluid. The main motivation behind using two different fluids is the advantage of being able to control wall temperature by changing heat flow to the exchanger.

Water has a higher specific heat and lower inlet temperature than the oil used in phase II of testing. Phase I wall temperatures are lower as compared to phase II due to higher heat flux to the water coolant. Care must be taken when using the existing water source for coolant. The author suspects inconsistency in mass flow and temperature due to other building demands on the water source. Some of the sources of error in the collected data taken during phase I are believed to be due in part to inconsistent inlet temperature and mass flow of the water source. Equation (III-2) shows the first law of thermodynamics applied to a heat exchanger in steady state condition. Changes in temperature and mass flow change the resulting heat rate  $Q$ .

$$Q = \dot{m} * C_p(T_{out} - T_{in}) \quad (III-2)$$

Phase II testing uses a mineral based oil as the cooling fluid. The oil is provided by an oil heater, which maintains the test plate inlet temperature and source pressure at 300° F and 89 psig, respectively. A higher consistency, from condition to condition or day to day, in heat flux to the exchanger is suspected due to controlling both the inlet temperature and the source pressure of the oil feed.

### III.4 Configurations tested

Several film-cooling designs, shown in Figure III-9, are examined alone and in series with one another to examine downstream heat release effects. Configurations include the fan, normal trench, radial trench, and ramp in the downstream location and an offset normal and slot in the upstream location. The fan, normal trench, ramp and slot all have 30° inclination angles in the streamwise direction. The offset normal configuration injects fluid normal to the surface. The radial trench injects fluid at a 60° inclination angle in the spanwise direction. Hole diameter is maintained at 0.5mm for the fan, ramp, normal, and trench designs. Each cooling insert uses 0.5mm holes except the slot. The slot width was cut to 0.5mm and the slot length is 38.1mm. The following drawings are in centimeters

The offset normal configuration represents two close packed rows of vertical holes, shown in Figure III-10, as used in a typical combustor effusion liner. The offset normal configuration represents an upstream condition where the coolant ejects farther into the mainstream. In theory, the offset normal configuration would reduce the local free radical concentration present and thus local heat release potential by consuming the reactive species prior to reaching the downstream film coolant.

Used in combustion chambers, normal jets help bring the combustion process to completion and pull heat from the surrounding surfaces as the gas moves downstream. Normal jets create a region where reactions can stabilize and complete away from the wall of the liner. If reactions do not occur close to the surface, the heat release will not significantly increase the components' surface temperature. Strategically locating a row of these holes in the location where reactions are desired, serves to significantly decrease the local downstream equivalence

ratio below one. This condition makes further secondary reactions improbable in the downstream coolant due to completion of the reactions upstream.

The laidback fan shaped configuration is the same used in previous investigations by Bohan and Evans, including a  $10^\circ$  axial expansion and a  $10^\circ$  lateral spread at the outlet as shown in Figure III-11. Fanned outlet holes have already shown to be poor cooling configurations in a reacting environment by Polanka et al [14]. The fan configuration is used to provide an estimation of worst-case mainstream equivalence ratio. Determining worst-case equivalence ratio provides the ideal mainstream condition for this experiment.

Figure III-12 provides the details of the angled slot. The angled slot is a continuous extrusion through the face of the plenum. The slot has a film ejection area equal to  $\sim 4.7$  times the exit area of the other plenums. The fan configuration has the smallest exit area at  $2.04\text{E-}6 \text{ m}^2$  followed by the offset normal at  $3.88\text{E-}6 \text{ m}^2$ . The ramped and trenched configurations all have the same exit area at  $4.08\text{E-}6 \text{ m}^2$ . The slot has the largest exit area which is  $1.94\text{E-}5 \text{ m}^2$ . Configuration exit areas are displayed in Table III-2. Slots present the ideal case for film cooling in both reacting and non-reacting mainstream conditions. Slot testing provides the best-case conditions which sets the benchmark to compare with other configurations.



Figure III-9. Cooling configurations

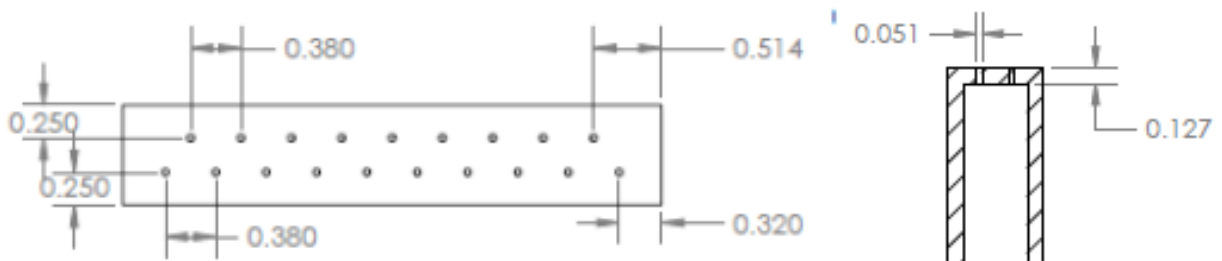


Figure III-10. Offset normal drawing detail (cm)



Figure III-11. Laidback fan shape drawing detail (cm)

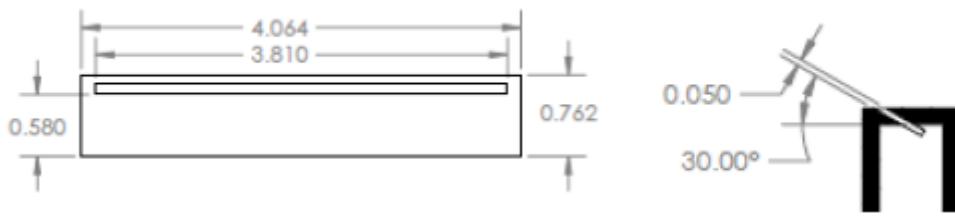


Figure III-12. Angled slot drawing detail (cm)

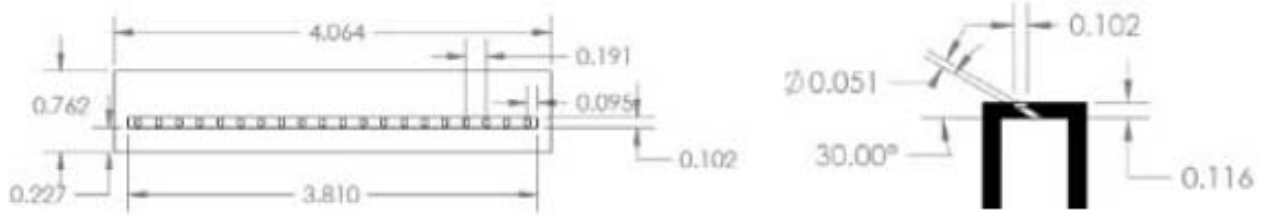


Figure III-13. Normal trench drawing detail (cm)

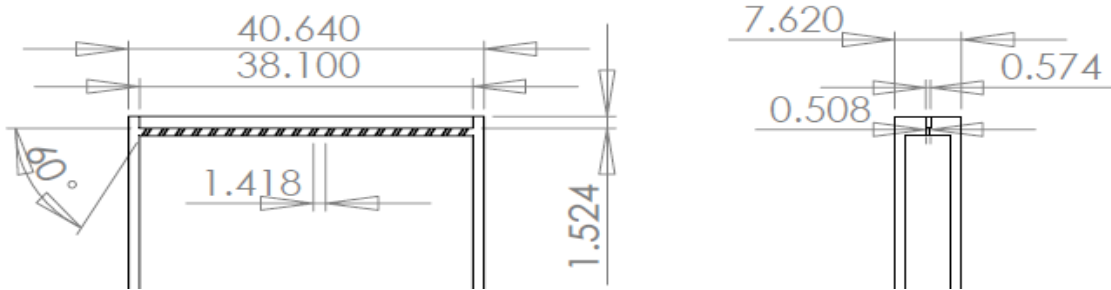


Figure III-14. Radial trench drawing detail (mm)

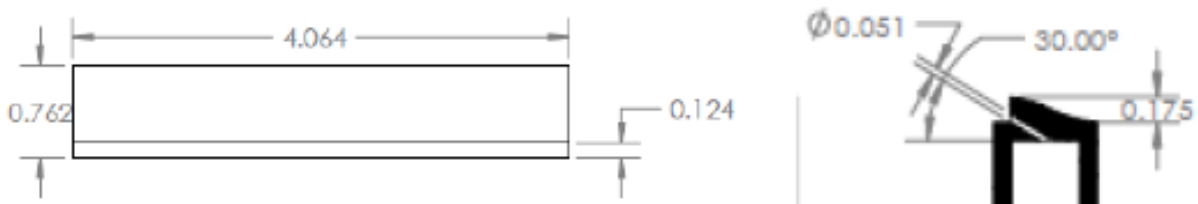


Figure III-15. Ramp drawing detail (cm)

Bunker et al [22], and Harrison et al [23], investigated the effectiveness of holes embedded in a transverse surface slot or trench. Trenches have the benefit of distributing the coolant more uniformly across the span. Trench designs more closely replicate slot cooling by reducing streamwise vortices resulting from individual orthogonal jets. These effects are a result of recirculation in the trench cavity by the coolant before entering the mainstream flow. The trench shown in Figure III-13 represents one of the configurations tested by Harrison et al and is referred to as a normal trench. Figure III-14 shows a similar configuration however, the holes inject in the spanwise direction into the trench; this configuration is referred to as the radial trench. One goal of this study aimed to understand how reacting flow fields interact with these types of cooling designs.

The ramped plenum extends into the mainstream flow, as shown in Figure III-15. This design replicates some of the features found in a combustor liner by pushing the free stream fuel rich gases off the surface, replacing them with coolant behind the backward facing step. The ramp configuration is inspired by previous backward facing step experimentation completed by Waitz et al [19]. One of the goals in this study is to understand if the ramped design could mitigate the effects of turbine burning by pushing the reactions off the surface.

Table III-2 indicates the test matrix accomplished as part of this investigation. The three new designs, namely the ramp and the trenches, occupy the downstream film-cooling bay to enable a comparison of film cooling performance. The offset normal or the slot is inserted in the upstream bay to investigate the effects of an upstream cooling row. It is noted that the upstream bay is located approximately 26 film cooling hole diameters upstream of the downstream bay. The downstream bay is located approximately 25 diameters from the upstream thermocouples

(C,D) and 95 diameters from the downstream thermocouples (A,B). This orientation is shown in Figure III-1.

Air is always used in the upstream cooling bay in series configurations (slot and offset normal). The downstream cooling bay switches between air and nitrogen. Switching between inert and reactive gasses provides the information needed to calculate augmentation, shown later as an analysis tool. Each test configuration is evaluated at a WSR equivalence ratio of 1.3 using propane ( $C_3H_8$ ) and air. This equivalence ratio was determined using the fan configuration as shown in Figure III-23 and discussed in section III.8.

Table III-2. Phase I testing “1”: Phase II testing “2”  
(Tested configurations with exit area displayed in  $m^2$ )

Upstream → Downstream ↓	Blank	Offset Normal (3.88E-6)	Slot (1.94E-5)
Fan (2.04E-6)	1	1	1
Ramp (4.08E-6)	1 2	1 2	1
Radial Trench (4.08E-6)	2	2	2
Normal Trench (4.08E-6)	1 2	1 2	1 2

### III.5 Pictures of different blowing conditions

Photographs were taken during testing for reference purposes and to get a visual understanding of the test results. Photographs provide confirmation of reactions occurring or not

occurring at different blowing conditions. Bohan [17] analyzes photographs to estimate reaction length and distance. The following pictures were taken during phase II testing. Photographs were taken looking through the right hand side of the test rig, reference Figure III-1 and Figure III-16. Each photograph represents a specific blowing condition using one of the phase II configurations. Phase II configurations consist of the radial trench, normal trench, and ramp alone and in series with the slot and offset normal cooling plenums.

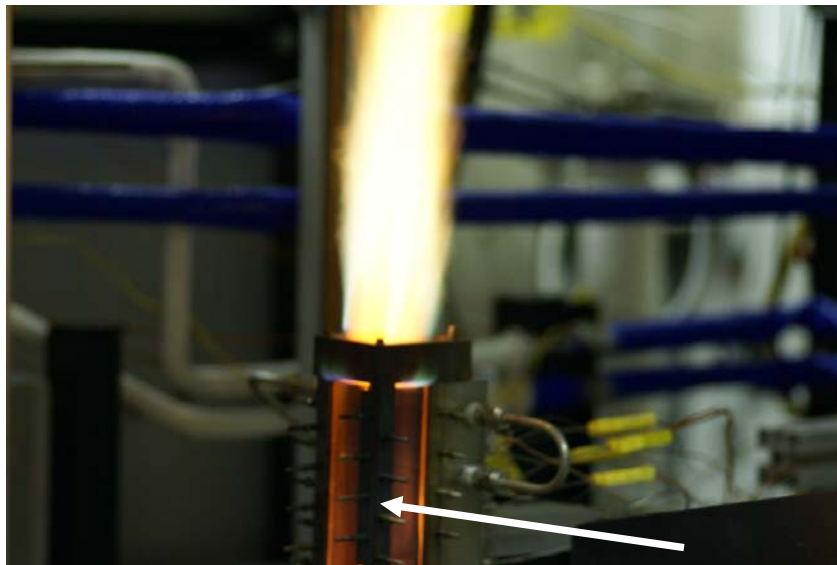


Figure III-16. Camera viewpoint, arrow pointing from front of camera to test rig

Figure III-17 is an example of the normal trench in the downstream bay at a blowing ratio of 1.0. Both upstream and downstream bays are shown as well as the approximate location of the 25-diameter distance downstream. If one were to zoom in on Figure III-17 on a small portion of the wall located near the tip of the 25-diameter arrow, a small black line would appear on the surface showing the bottom ledge of the thermocouple block.

The blue flame emitted from the downstream bay is a result of the cooling air mixing with the mainstream and reacting. As the blowing ratio increases from 1.0 to 3.0, the length of the

flame increases as seen when comparing Figure III-17 and Figure III-18. The presence of the flame is evidence of additional reactions occurring in the mainstream due to the introduction of air coolant.

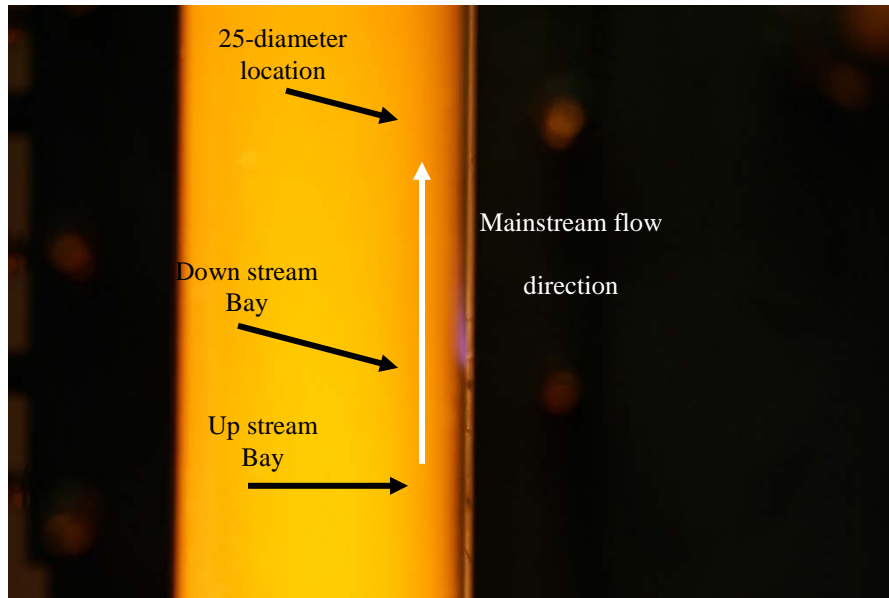


Figure III-17. Phase II - Air injection;  
US: Blank, DS: Normal trench,  $M=1.0$ ,  $\phi=1.3$

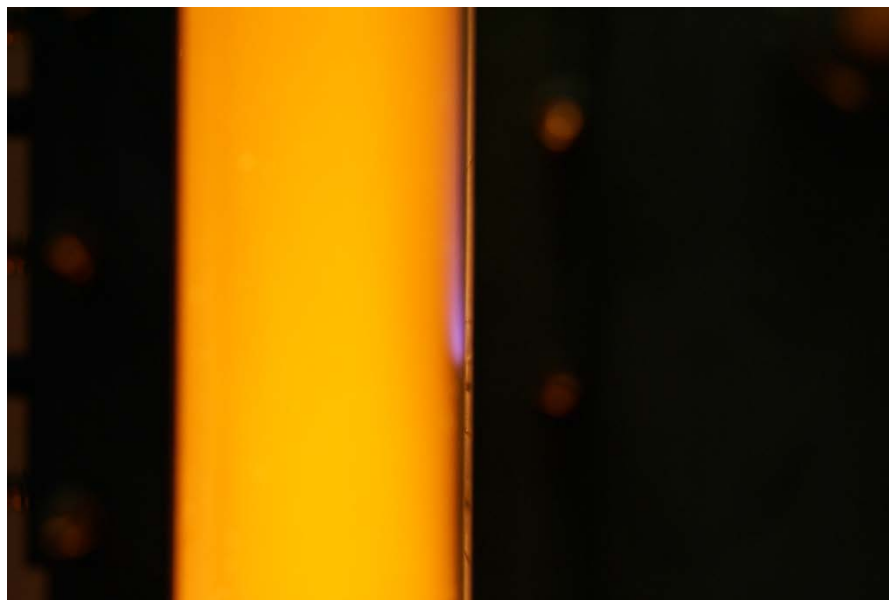


Figure III-18. Phase II - Air injection;  
US: Blank, DS: Normal trench,  $M=3.0$ ,  $\phi=1.3$

### III.6 Correction factors and error analysis

Slight variations in mainstream conditions exist due to the nature of the materials used in this experiment. Heating and expansion of the ceramic material in the reactor core changes downstream conditions. Reactor core dimensions change as the WSR core expands and contracts due to the heating and cooling from warm up to shut down and from day to day. Analysis of mainstream conditions provides further insight into the transient aspect of the reactor.

Phase I mainstream analysis is performed by taking repeatability data at different reference conditions from the beginning to the end of a test day. Phase II mainstream analysis is performed by taking repeatability data at a zero-zero blowing condition throughout each test day. Phase I data provides error associated within a particular day while phase II data shows error associated within each day as well as day-to-day.

Phase I repeatability results show large error when comparing reference conditions from beginning to end of a particular test day. Each configuration shown in Figure III-19 was tested on a different day, therefore each configuration has its own error estimation. This is evident in Figure III-19 showing error of each phase I configuration. Error is calculated by finding the difference between beginning and ending heat flux reference conditions. Meaning, at the beginning and ending of each test day a set blowing condition is repeated to find the error from beginning to end. The reference conditions, used to find error, are taken at the 25-diameter location. Error is shown as a percentage and is calculated using Equation (III-3).

Phase I reference conditions are set at a blowing ratio of 1.0 and 2.0 at a mainstream equivalence ratio of 0.6. Phase I normal trench data indicates an error of less than 2%, ramp data indicates an error of ~8%, and the radial trench indicates an error of ~15% from beginning to end

of the test day. Phase I radial trench data is not shown in the results section due to a large error of ~15%. The large negative errors are caused by larger  $q''_{ending,ref}$  values than  $q''_{beginning,ref}$  values resulting in a ratio, shown in Equation (III-3), of less than 1.0. The error between each configuration is unknown as the reference conditions from one configuration cannot be compared to the others due to dissimilar configuration performance.

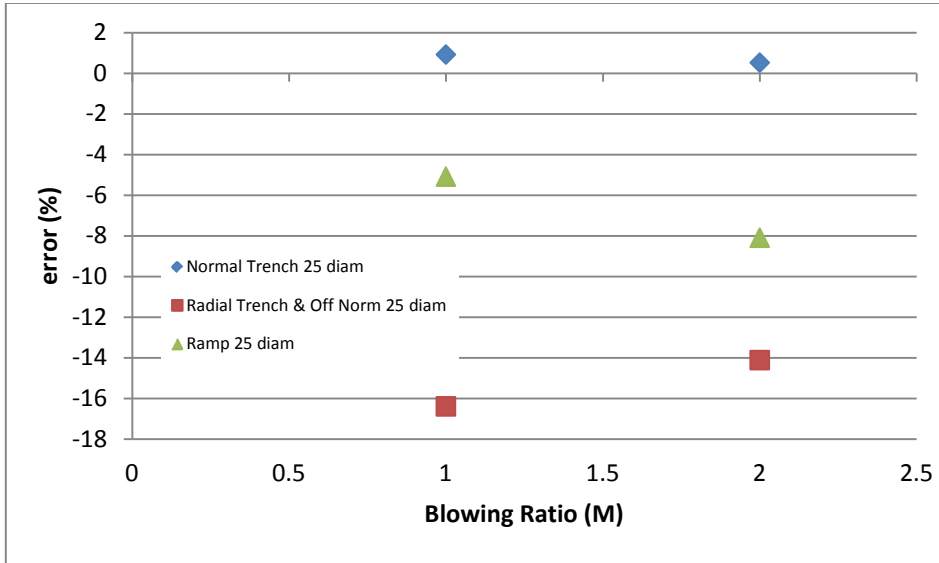


Figure III-19. Error estimations of phase I testing – inter day, DS: variable US: offset normal w/ radial trench downstream, all other cases blank

$$error (\%) = \left( \frac{q''_{beginning,ref}}{q''_{ending,ref}} - 1 \right) * 100 \quad (III-3)$$

To allow for better interpretation of results and error, phase II testing included a number of zero-zero testing conditions taken throughout the testing period. Testing without injection of air or nitrogen from either cooling bay allows one to track changes in mainstream conditions. Changing mainstream conditions is the expected cause of the error seen in phase I of testing. A zero-zero test point refers to a zero blowing condition from both bays while at steady state

mainstream conditions. This allows for inter day and day-day error calculations and correction factors. Figure III-20 represents a series of zero-zero test points taken during phase II of testing.

Figure III-20 data is used to correct phase II test results to eliminate error.

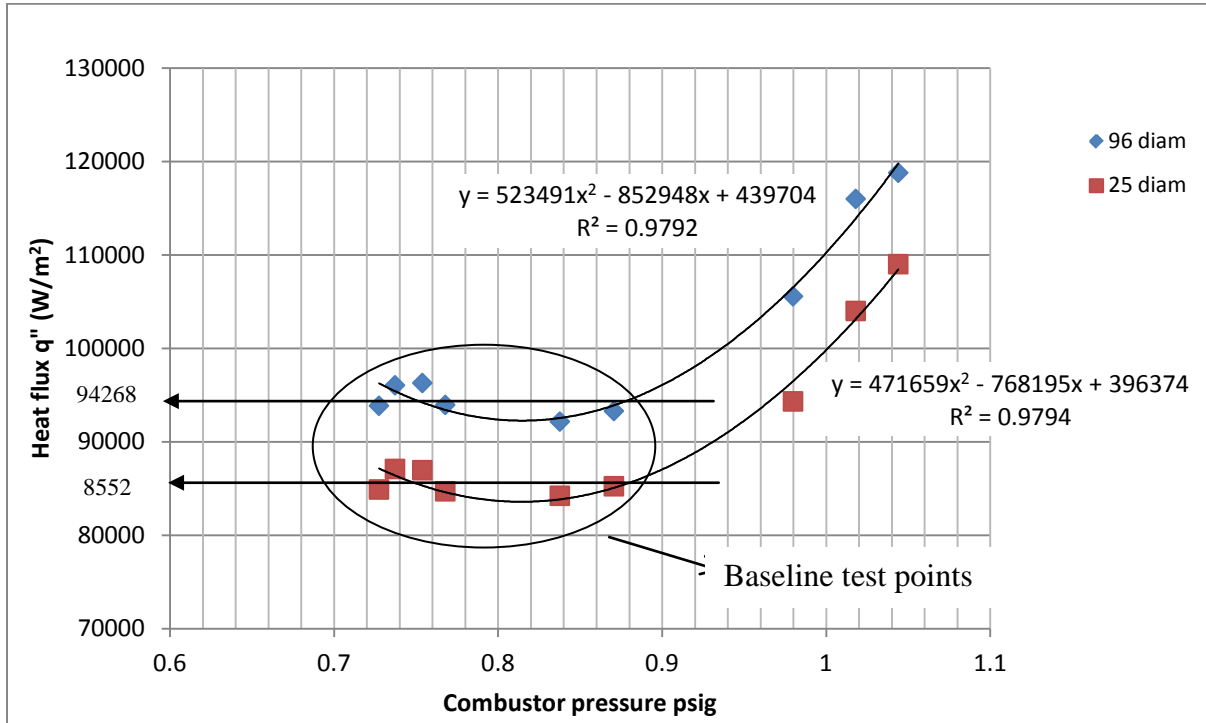


Figure III-20. Zero-Zero plot results of phase II testing w/o ramp.

Table III-3 displays the zero-zero values used to calculate baselines, statistical results, and correction factors.  $T_{stack}$  represents the measured mainstream temperature in degrees K entering the test section.  $P_{combustor}$  represents the measured pressure in psig inside the combustion chamber.  $WSR_{temperature}$  represents the temperature in degrees K inside the combustion chamber. Columns labeled with “AB” or “CD” represent the average value from the preceding two columns. Columns labeled with “corrected” represent the preceding columns corrected value.

Table III-3. Baseline  $q''$  values and corrections w/o ramp

Tstack	PCombustor	WSR Temp	$q''A$	$q''B$	Average $q''AB$	Corrected $q'' AB$	$q''C$	$q''D$	Average $q''CD$	Corrected $q''CD$
K	psig	K	W/m <sup>2</sup>	W/m <sup>2</sup>	W/m <sup>2</sup>	W/m <sup>2</sup>	W/m <sup>2</sup>	W/m <sup>2</sup>	W/m <sup>2</sup>	W/m <sup>2</sup>
1751	1.04	1863	118021	119577	118799	93279	109485	108549	109017	86089
1755	0.98	1834	110699	100446	105573	93296	101450	87199	94325	83347
1747	1.02	1857	120055	111950	116003	96353	109579	98430	104004	86373
1752	0.74	1813	96971	95134	96053	94913	89013	85170	87092	86221
1773	0.75	1852	96833	95757	96295	96360	88557	85368	86962	87173
1759	0.73	1843	93352	94364	93858	91874	85459	84332	84895	83268
1758	0.77	1880	93184	94712	93948	94801	84837	84570	84704	85620
1759	0.84	1887	87003	97328	92165	93890	79407	89039	84223	85904
1753	0.87	1899	86951	99637	93294	93656	79136	91350	85243	85686

Data correction consists of adjusting all data points to the same baseline. Baseline conditions are calculated using the average value from the bottom six test points circled in Figure III-20. Two baselines are calculated, one for the 95-diameter data and one for the 25-diameter data. To justify the data used as the baseline value, a statistical analysis is performed and shown in Table III-4. Confidence levels are calculated using the student-t distribution with a 95% confidence level and a sample size of 6. The upper critical value is equal to 2.571. Also shown in Table III-4 are the wall temperature baselines and statistical analysis.

Table III-4. Statistical analysis - phase II data, averaged baseline values w/o ramp

Calculation of 6 baseline points	$q''$ (W/m <sup>2</sup> ) T (K) Average	Standard deviation $\sigma$	95% confidence in mean ( $\pm$ )	$T_{wall}$ (K)	Standard deviation $\sigma$	95% confidence in mean ( $\pm$ )	$\bar{h}$ (W/m <sup>2</sup> K)	95% confidence in mean ( $\pm$ )
95 dia base	94268.8 (W/m <sup>2</sup> )	1608.54 (1.71%)	1688.1 (1.79%)	697.23	3.85 (0.55%)	3.08 (0.44%)	88.768	1.72 (1.94%)
25 dia base	85519.9 (W/m <sup>2</sup> )	1213.63 (1.41%)	1273.6 (1.49%)	732.75	3.97 (0.54%)	3.17 (0.43%)	83.316	1.41 (1.69%)
T entrance	1759.2 K	7.26 (0.41%)	7.618 (0.43%)	-	-	-	-	-

Wall temperature is calculated by extrapolating the temperature measurements taken during testing. Wall temperature calculation is included in Evans [18] and repeated here for understanding. Using the heat flux equation shown in Equation (III-1) one can solve for  $q''$  at a

particular test condition. Insert this value into Equation (III-4) and solve for the constant C. Then plug q'' and the previously calculated C into Equation (III-5) and solve for T<sub>(wall)</sub> by setting x equal to zero. T<sub>wall</sub> is representative of the surface temperature in a specific test condition.

$$\frac{a_1}{2} * T_1^2 + a_0 * T_1 + q'' * x_1 - C = 0 \quad (III-4)$$

$$\frac{a_1}{2} * T_{wall}^2 + a_0 * T_{wall} + q'' * x - C = 0 \quad (III-5)$$

The same process shown previously to calculate baseline heat flux is used to calculate baseline wall temperatures shown in Table III-4 and Table III-6. Table III-5 shows a list of zero-zero wall temperatures including the ramp data on the right hand side. Baseline wall temperatures are calculated using the data points that correspond to the combustor pressure range of 0.7-0.9. Baseline wall temperature, heat flux and the convective coefficient, shown in Table III-4 and III-6 will be used in the results section to calculate augmentation and normalized temperature for phase II results.

Table III-5. Zero-Zero wall temperature data for all configurations

Clean Configurations						Ramp Configuration						
Zero-Zero test points	PCombustor	TwallA	TwallB	TwallC	TwallD	Zero-Zero test points	PCombustor	TwallA	TwallB	TwallC	TwallD	
	psig	K	K	K	K			K	K	K	K	
	1.04	744	751	789	792			0.84	721	730	749	763
	0.98	726	716	763	744			0.81	715	724	744	751
	1.02	749	743	791	778			0.76	718	730	746	752
	0.74	699	701	736	734			0.76	722	736	756	760
	0.75	701	704	739	738			0.86	725	739	755	761
	0.73	694	699	731	731			0.66	711	733	745	754
	0.77	694	701	732	734							
	0.84	682	701	719	735							
0.87	684	707	722	742								

Now that the baselines have been established, one can use the second order polynomial curve fit shown in Figure III-20 to normalize all data to the baseline values. An example of 95-

diameter data correction is shown in Equation (III-6). A similar correction is done for 25-diameter data using the respective polynomial found in Figure III-20 above. The correction is made based on the calculated polynomial value of  $q''$  corresponding to the measured combustor pressure. The calculated  $q''_{\text{measured}}$  value is normalized by subtracting the difference between the polynomial calculation of  $q''_{\text{poly}}$  and the baseline  $q''_{\text{baseline}}$ . This correction method is used to correct each heat flux data points in phase II testing.

$$q''_{\text{correct}} = q''_{\text{measured}} - (523491 * P_{\text{comb}}^2 - 852948 * P_{\text{comb}} + 439704 - q''_{\text{baseline}}) \quad (\text{III-6})$$

Convective heat transfer coefficient “h” values are calculated using 1759.2 K for mainstream temperature. Mainstream temperature is calculated by averaging the values of  $T_{\text{stack}}$  over the same zero-zero test points shown in Table III-3. Variations in  $T_{\text{stack}}$  could be the primary cause of the variation seen in mainstream conditions. However, the mainstream thermocouple is subjected to the same fluctuation in mainstream conditions and the test section. Therefore, variation in test section heat flux may be a flow phenomena associated with the convective coefficient.

The ramp zero-zero data is excluded from Figure III-20, Table III-3 and Table III-4. This is due to a significant offset in the ramp’s zero-zero data from the other data. All zero-zero ramp data shows significantly higher heat flux for both the 25-diameter and 95-diameter measurements at the tested combustor pressures. This indicates a disturbance to the flow field due to the presence of the ramp. This disturbance is understandable due to the ramp’s protrusion into the mainstream. Any protrusion into the mainstream will trip the flow creating turbulence. The increase in turbulence is the reason for the ramp’s higher  $q''$  values due to the increase in the

convective heat transfer coefficient. This is the reason for exclusion from the above baseline and curve fit calculations. Figure III-21 below shows the ramps zero-zero values.

A higher convective coefficient will not exclude the ramp data from our comparative analysis. The ramp data is treated the same as the other configurations. Treating the ramp data like the other configurations assumes the same relationship between combustor pressure and calculated heat flux. The baseline values for the ramp at the 25 and 95-diameter distances require a separate statistical analysis shown in Table III-6.

Table III-6. Statistical analysis - phase II data, averaged baseline values ramp only

Calculation of 6 ramp points	$q''$ (W/m <sup>2</sup> ) Average	Standard deviation $\sigma$	95% confidence in mean ( $\pm$ )	$T_{\text{wall}}$ (K)	Standard deviation $\sigma$	95% confidence in mean ( $\pm$ )	$\bar{h}$ (W/m <sup>2</sup> K)	95% confidence in mean ( $\pm$ )
95 dia base	108403.4 (W/m <sup>2</sup> )	2221.9 (2.04%)	2331.7 (2.15%)	725.45	4.71 (0.65%)	4.94 (0.68%)	104.86	2.435 (2.32%)
25 dia base	97482.7 (W/m <sup>2</sup> )	1260.1 (1.29%)	1322.36 (1.35%)	753.11	4.84 (0.64%)	5.08 (0.67%)	96.89	1.58 (1.63%)

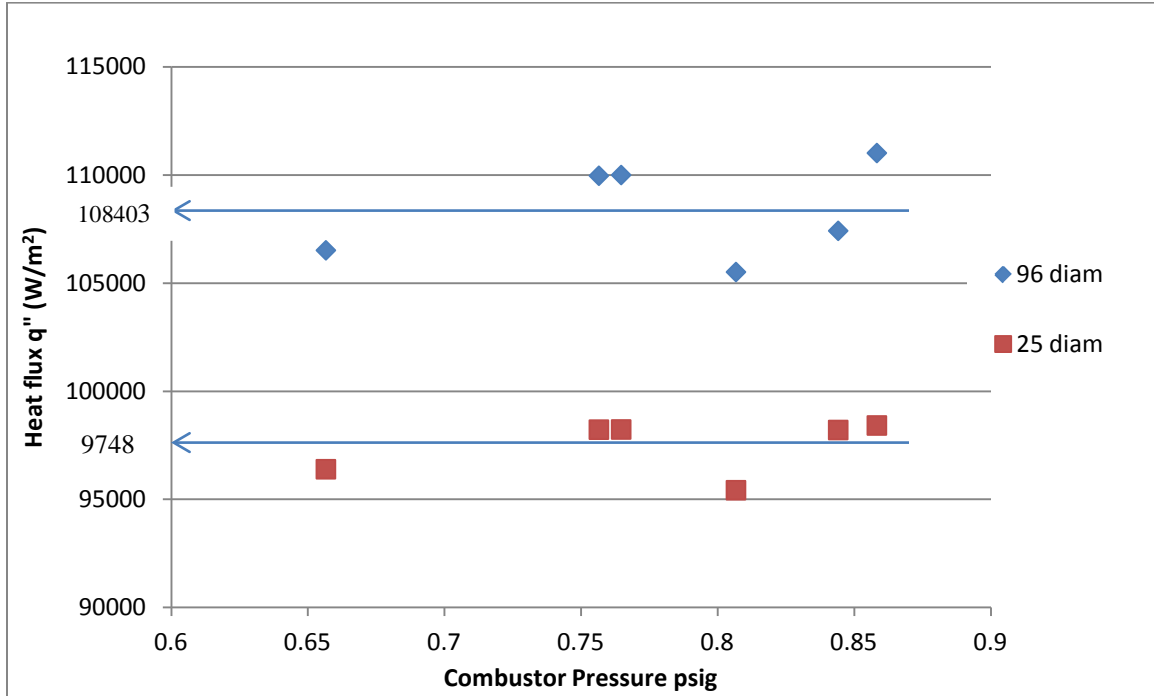


Figure III-21. Zero-zero data with ramp included

Over time, the combustor pressure drops due to the heat load from the reactions in the chamber. Therefore, one would assume the reactor to produce sequential points of decreasing combustor pressure from day-to-day or condition-to-condition. However, each point is not sequential; the data point taken at the lowest shown combustor pressure in Figure III-20 was not the last zero-zero point taken on the third day. In fact, the lowest shown zero-zero data point was taken at the end of the second day. This fact adds merit to the baseline and curve fit calculations due to the repeatability of the combustor pressure data points.

### **III.7 Methods of analysis**

Heat flux, as shown above in Equation (II-1), consists of two independent variables including the convective heat transfer coefficient and adiabatic wall temperature. Several different analysis tools were used to examine the changes to adiabatic wall temperature and/or the convective coefficient. Analysis methods included examining raw heat flux and temperature data, heat flux augmentation, and adiabatic wall temperature calculations. Augmentation and raw heat flux data will help identify the optimum film cooling configuration using a direct comparison method. Adiabatic wall temperature calculations will help identify methods of determining worst-case film cooling conditions. Augmentation results are presented first followed by adiabatic wall temperature calculations. Each analysis method is applied to phase I and II data.

The following analyses use averaged heat flux results of the left and right sides at the 25 or 95-diameter locations. Averaging the left and right sides eliminates some of the side-to-side or asymmetric error during testing. However, the data for the radial trench must be presented as both left and right sides to show the intended asymmetric cooling performance for this case. The legends and figure labels represent averaged data unless specifically designated as left and right. Deviations from averaged values are pointed out in the following analysis.

Non-dimensional distance is used to show the distance of the measurement location from the downstream bay. Non-dimensional distance is calculated using Equation (III-7). Downstream distance is equal to the distance measured from the outlet of the cooling hole to the measurement location ( $x$ ) divided by the diameter of the jet used in the film cooling

configuration. This is the typical method of presenting downstream distance as presented previously in Chapter 2.

$$\text{downstream distance} = x/d_j \quad (\text{III-7})$$

### III.7.1 Augmentation

Augmentation calculations result from comparing heat flux measurements using air and nitrogen as the injected cooling fluid. Nitrogen does not create additional reactions, as it is an inert fluid. Air may create additional reactions by increasing the local oxygen concentration. Increasing the local oxygen concentration allows reactive species in the free stream to find their stable forms namely, CO<sub>2</sub> and H<sub>2</sub>O. Therefore, by comparing nitrogen test results to air test results under similar conditions from the same cooling configuration, one can determine the amount of additional reactions occurring in the mainstream.

$$\text{Augmentation}(\sigma) = \left( \frac{q_{air}}{q_{nitrogen}} - 1 \right) * 100 \quad (\text{III-8})$$

Comparing the downstream heat flux measurements for the reacting case (air) with the non-reacting case (nitrogen) reveals the augmentation due to the additional secondary reactions. Specifically, finding the increase in heat flux as a percentage over the baseline nitrogen case allows one to estimate the increase in local gas temperature due to the injection of air. This percentage comparison is made by dividing the heat flux results from the air and nitrogen test cases. Heat flux results used to calculate augmentation are obtained by using the same blowing

conditions from the same configuration and switching between inert (nitrogen) and reactive (air) gases as the coolant. Heat flux augmentation is calculated using Equation (III-8). An augmentation of zero represents similar performance to nitrogen. A negative augmentation would represent better performance than nitrogen and a positive augmentation would represent worse performance than nitrogen. An example augmentation calculation is presented in Table III-7.

Table III-7. Example Phase II – Augmentation at  $y/d_j = 25$ ;  
US: Blank, DS: Normal Trench,  $\phi=1.3$

DS: Blowing Ratio	$q''$ air	$q''$ N2	Augmentation
0.5	98797	79884	23.7
1	106357	74623	42.5
1.5	111017	69630	59.4
2	113513	67935	67.1
3	109020	65897	65.4

Raw heat flux data will also be presented along with the augmentation data to provide a quantitative comparison tool. Augmentation represents the additional reactions and heat flux represents the actual heat load on the surface. Raw heat flux data can provide some additional insight into the trends and magnitudes of a particular configurations' performance. To find the best-case cooling configuration both augmentation and raw heat flux must be considered. Heat flux plots consist of the heat flux data presented in example Table III-7 and are labeled with nitrogen or air in the caption.

### III.7.2 Normalized wall temperature

The second method of analysis presented in this study uses a normalized wall temperature to determine cooling effectiveness. Normalized wall temperature provides a ratio of tested adiabatic wall temperature to maximum adiabatic wall temperature. Tested adiabatic wall

temperature is what was experienced in each downstream location during testing and is partly responsible for the increased heat flux to the surface. Maximum adiabatic wall temperature is equal to the temperature reached when all chemical potential in the flow is released near the surface of the wall. Normalized wall temperature applies the same concept as adiabatic effectiveness with a modification for a reacting boundary layer. Comparing tested adiabatic wall temperature with maximum adiabatic wall temperature will help determine worst-case cooling conditions.

Mainstream chemical potential controls maximum adiabatic wall temperature. Adiabatic flame temperature, being the upper limit on potential energy generated in a combustion reaction, sets a limit on maximum adiabatic wall temperature. Therefore, the potential to drive heat to the wall for any given blowing ratio is limited by the maximum adiabatic wall temperature. Species type and concentration determine the adiabatic flame temperature due to the enthalpy of formation and local equivalence ratio. An assessment on total potential energy release of the flow allows one to make a comparison to tested conditions leading to a potential worst-case configuration.

Potential energy release was calculated using Chemical Equilibrium with Applications (CEA) provided by NASA's Glenn Research Center [24]. The equilibrium code uses standard atmosphere temperature and pressure inlet conditions to the WSR at an equivalence ratio of 1.3 using propane and air. The result of this simulation provided the species concentrations present in the mainstream flow of the test rig. A second case was run with additional air combined with the residuals from the previous calculation to create an equivalence ratio of 1.0 to simulate worst-case blowing conditions near the wall. CEA input temperatures for the air coolant (550 K) and mainstream (1759 K) match the measured mainstream and coolant conditions present

during testing. Reaching an equivalence ratio of 1.0 requires 0.255 moles of additional air to the mainstream concentrations, reference appendix B. The calculated maximum adiabatic flame temperature is 2086 K ( $T_{max}$ ) at an equivalence ratio of 1.00. This maximum adiabatic flame temperature is the theoretical maximum temperature in all conditions because it is primarily dependent on mainstream chemical potential. An equivalence ratio of 1.0 represents the appropriate stoichiometric proportions of oxygen from the coolant and reactive species in the mainstream. Appendix B provides the CEA simulation summaries including test conditions and resulting species concentrations.

Normalized temperature calculates the ratio of achieved versus maximum total heat release potential present in the flow. Results are presented in terms of a non-dimensional value theta, shown in Equation (III-9). The upper limit of normalized temperature ( $\theta$ ) is theoretically equal to 1.0. A normalized temperature of 1.0 represents a reaction occurring at the adiabatic flame temperature near the surface of the wall. To calculate theta one needs a good estimation of the tested adiabatic wall temperature ( $T_{aw}$ ) present in the test section at every blowing condition. Correct adiabatic wall temperature estimations will provide the corresponding amount of achieved heat release.

$$\theta = \frac{T_{aw} - T_{stack\ entrance}}{T_{max} - T_{stack\ entrance}} \quad (III-9)$$

This section contains two different methods of finding tested adiabatic wall temperature. Method I adiabatic wall calculations utilize the convective heat transfer coefficient found in the corresponding nitrogen case. Method II adiabatic wall calculations utilize the mean value of the convective heat transfer coefficient. Mean heat transfer coefficient values are found using the

mean values of wall temperature and heat flux found in the baseline zero-zero calculations in Table III-4. The convective coefficient assumption is critical to calculating the subsequent tested adiabatic wall temperature.

Method I normalized temperature results calculate adiabatic wall temperatures ( $T_{aw}$ ) by assuming similar convective coefficients between nitrogen and air cases. The convective coefficient from the corresponding nitrogen case is found by inserting the nitrogen coolant temperature (~550K), test rig entrance temperature (~1760K), calculated wall temperature and heat flux into Equation (II-1) and solving for “h”. Changes to the local turbulence and rotation in the fluid due to either air or nitrogen injections are approximately the same, minus the effects due to the combustion process. Assuming similar fluid mechanics between nitrogen and air allows one to assume similar heat transfer coefficients. Equation (III-10) shows an example calculation of the nitrogen specific heat transfer coefficient.

$$h_{N2} = \frac{q''_{N2}}{(T_{\infty(\text{mainstream})} - T_{\text{wall}(N2)})} \quad \text{(III-10)}$$

Notice the use of  $T_{\infty}$  instead of  $T_{aw}$  in the denominator. Since the adiabatic wall temperature, when using nitrogen, is unknown the mainstream temperature must be inserted to take its place if one wants to approximate the convective coefficient. This means the calculated convective coefficient is off by an amount equivalent to the ratio between measured heat flux and the difference between mainstream and actual adiabatic wall temperature. The calculated nitrogen convective coefficient assumes more error as the adiabatic wall temperature decreases with an increase in nitrogen blowing ratio. Equation (III-11) shows the subsequent adiabatic

wall calculation for the air-cooled case using the previously calculated nitrogen convective coefficient.

$$T_{aw(air)} = q_{air}'' / h_{N2} + T_{wall(air)} \quad (III-11)$$

Method II adiabatic wall temperature calculation uses the corrected values for wall temperature and heat flux to calculate an average convective heat transfer coefficient as shown in Table III-4. Using corrected values minimizes the error in the tested results by eliminating the effects due to changing mainstream conditions. Using an averaged heat transfer coefficient found in the zero-zero case (Table III-5), yields a slightly different approximation of adiabatic wall temperature. The example calculation shown below in Equation (III-12) assumes a constant convective coefficient regardless of the blowing condition.

$$T_{aw} = q'' / \bar{h} + T_{wall} \quad (III-12)$$

Method II uses a constant convective coefficient to calculate the adiabatic wall temperature. Assuming a constant convective coefficient introduces error when the blowing ratio is increased. This is due to the changes in the local flow field created by the injection process. Any injection process or disturbance to the local flow field will create turbulence. This turbulence creation is shown by Bunker et al [25], and dissipates with increasing downstream distance. However, the turbulence created will not dissipate within the tested 25-diameter distance and will increase the mean heat transfer coefficient. Using the data presented by Bunker, increases to the convective coefficient at the 25-diameter distance are small ~3%. This will be considered when presenting the normalized temperature plots in Section IV.4.

### III.7.3 Extrapolating to adiabatic wall temperature

Adiabatic wall temperature can also be calculated by using an extrapolation technique similar to the method presented by Smith et al [26]. Smith's method presents a graphical solution to finding the convective heat transfer coefficient. This graphical method requires one to find heat flux and total temperature in the mainstream over a given set of test conditions. This type of analysis requires one to vary two parameters instead of just the blowing ratio. The two parameters that are varied in Smith's method include wall temperature and blowing ratio.

In Smith et al [26], adiabatic wall temperature is a known value and is used to determine the convective heat transfer coefficient. This cannot be done in the current investigation due to the unknown value of adiabatic wall temperature. However, Smith's extrapolation method presents a powerful tool that can be used to find an adiabatic wall temperature. Figure III-22 is similar to the graphical method shown by Smith and presents an example extrapolation to the adiabatic wall temperature.

To obtain the data needed for the extrapolation one needs to change the wall's temperature. Changing the wall's temperature will change the resulting heat flux if all other dependent variables are held constant. The dependent variables in this investigation include mainstream conditions and blowing ratio. Smith changes the wall's temperature by changing the heat sink on the flat test plate used in his experiment. Variable wall temperature is possible in the current investigation by switching between oil and water as the heat sink. One can extrapolate from the known data (heat flux and wall temperature) to the desired adiabatic wall temperature, which is coincident with the zero heat flux point. When heat flux is zero, the wall is effectively adiabatic and the wall temperature is the adiabatic wall temperature.

Water-cooling provides the upper resultant heat flux and the first data point. Oil-cooling provides a lower heat flux and contributes the second point. A linear extrapolation is performed to solve for the x-axis intercept. The temperature at which heat flux goes to zero is local gas temperature or adiabatic wall temperature. The example shown in Figure III-22 shows a hypothetical test point, which is used to determine an adiabatic wall temperature and convective heat transfer coefficient.

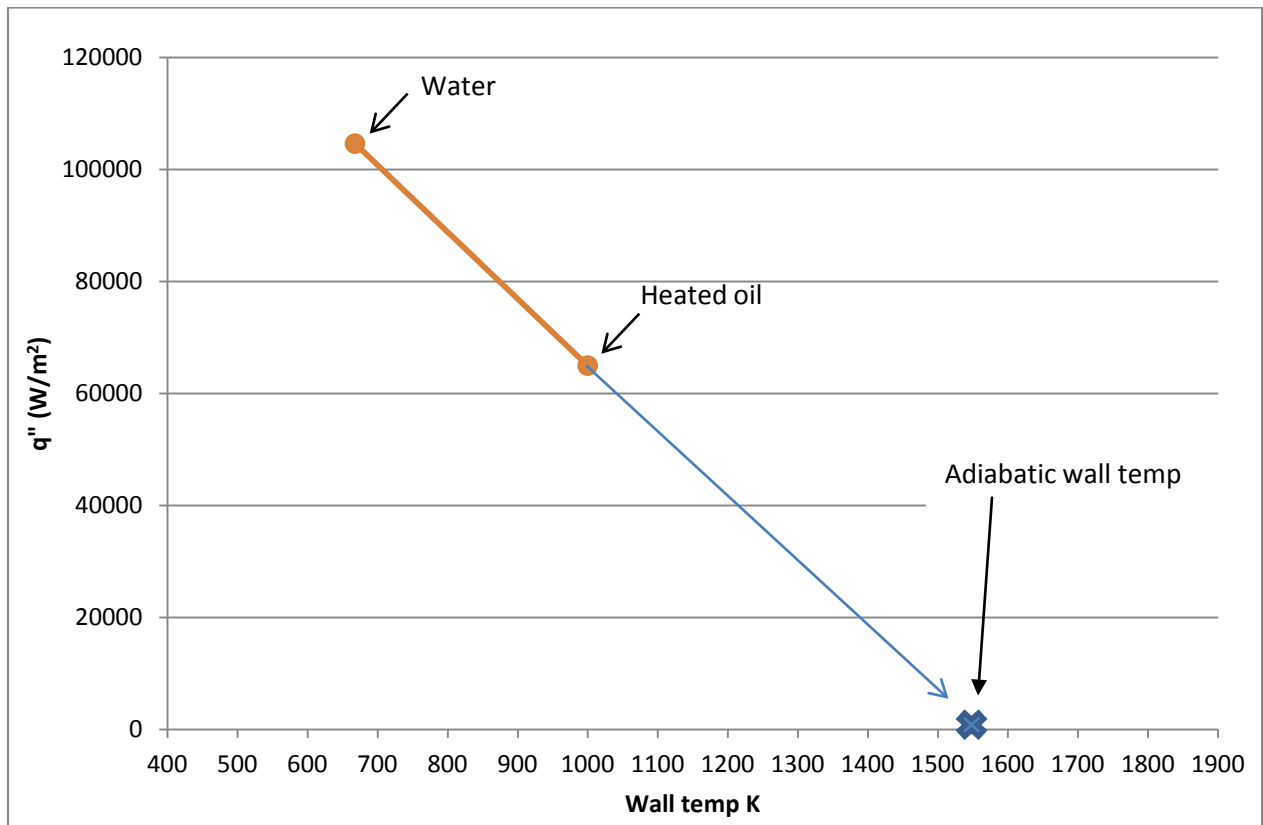


Figure III-22. Adiabatic wall temperature extrapolation example

### III.8 Determination of WSR Equivalence Ratio

The WSR equivalence ratio used in this investigation is significant to the results obtained. Mainstream conditions are critical to finding the best and worst-case cooling configurations and

blowing ratios. Mainstream conditions dictate quantities of reactive species, temperatures and pressures of the fluid as well as turbulence levels. Finding the best and worst-case cooling conditions is specific to mainstream properties. A determination must be made, prior to testing, on what mainstream conditions should be.

Mainstream radical concentrations are the key aspect of the mainstream condition and depend on the proportions of fuel and oxidizer in the WSR. Higher WSR equivalence ratios will yield higher concentrations of mainstream free radicals. Therefore, a separate test was performed to determine what WSR equivalence ratio yields the highest augmentation. The WSR equivalence ratio that yielded the highest augmentation, under test representative blowing conditions, was considered the optimum WSR equivalence ratio. The laid-back fan shape configuration was used to run the equivalence ratio test due to known poor performance in reactive environments as shown by Polanka et al [14].

Figure III-23 shows augmentation results for the laidback fan configuration at blowing ratios of 1.0 and 2.0. Blowing ratios of 1.0 and 2.0 represent the ideal range of blowing ratios tested in the following investigation. Figure III-23 indicates the highest potential for heat release occurring between a WSR equivalence ratio of 1.2 and 1.3. The data also suggests that increasing the blowing ratio results in both larger augmentations as well as peak augmentation at a higher equivalence ratio. Figure III-23 indicates the ideal worst-case equivalence ratio for the fan configuration around an equivalence ratio of 1.3. All experimentation conducted during phase I and II will use an equivalence ratio of 1.3.

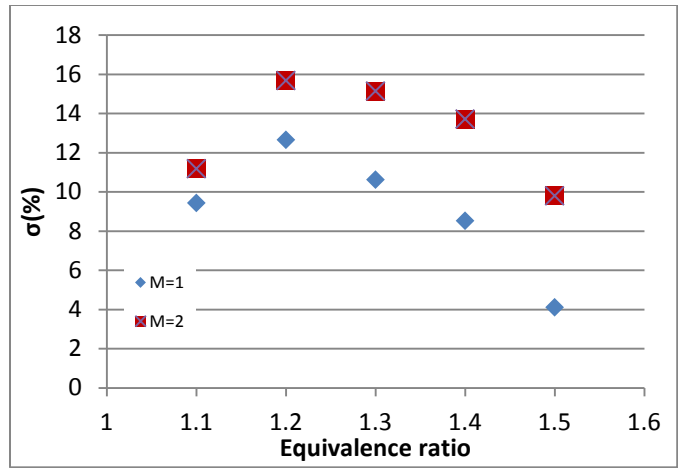


Figure III-23. Phase I: Max augmentation( $\sigma$ ) for fan configuration at  $x/d_j = 25$

In addition to the augmentation plot, the associated raw heat flux values provide a relative comparison of local wall heat loading as shown in Figure III-24 and Figure III-25. The data shown in Figure III-24 and Figure III-25 is the data used to calculate augmentation shown in Equation (III-8). The raw heat flux values, both air and nitrogen, provide a quantitative measurement tool to support the augmentation analysis. Figure III-24 and Figure III-25 indicate a higher heat load, in both air and nitrogen conditions, at a blowing ratio of 2.0 than at 1.0. This is not always the case as will be shown in the following analysis.

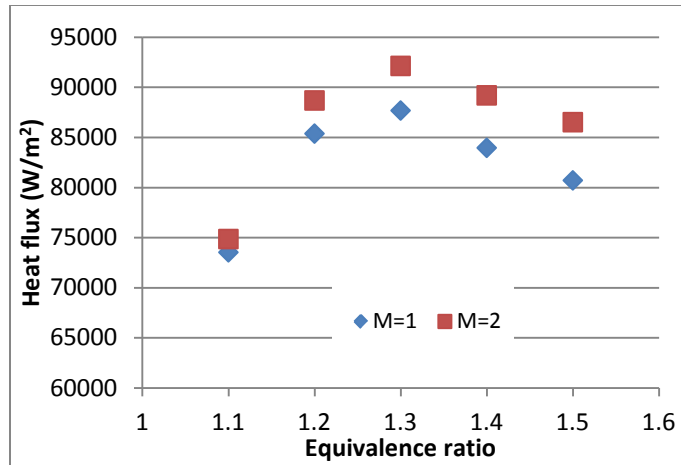


Figure III-24. Phase I: Heat flux data, fan at  $x/d_j = 25$ , air-coolant

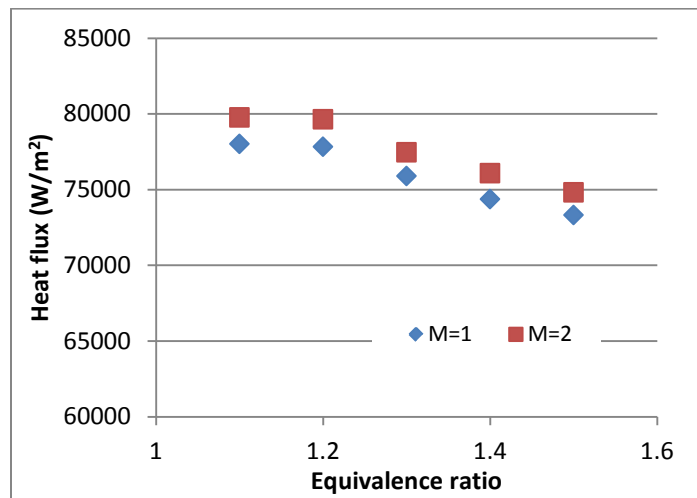


Figure III-25. Phase I: Heat flux data, fan at  $x/d_j = 25$ , N<sub>2</sub>-coolant

## **IV. Results and Analysis**

This investigation intends to find appropriate methods of evaluating film cooling performance in a reacting flow. As such, the trenched designs were evaluated to determine their ability to reduce secondary reactions. Trenched designs create a more even distribution of flow like that of a slot; therefore, trenched designs should provide better performance than fanned or normal hole configurations. The ramp design was also evaluated on its ability to push reactions off the surface. Although it may increase the downstream turbulence and heat flux, it has the potential to reduce downstream reactions by lifting the reactions further from the wall. The series injection testing seeks to find the potential to decrease downstream reactive species by consuming them with upstream coolant injection. Series configurations will be evaluated on their ability to reduce downstream secondary reactions.

### **IV.1 Test Matrix for Phase I and Phase II**

Phase I augmentation and heat flux compares the normal trench, fan and ramp configurations with and without upstream input. For series configurations, upstream input varies between offset normal and the slot. Fan results were taken from Bohan [17] and are repeated here for comparison purposes. Phase II compares the normal trench, radial trench and ramp configurations with and without coolant flow in the upstream bay. Results are presented in terms of heat flux, augmentation and normalized temperature. Phase II analysis uses corrected heat flux data, as shown in Section III-6, to compensate for changes in mainstream conditions.

One point of note to keep in mind when viewing augmentation and heat flux data is the averaging method used with presenting calculated heat flux. Due to the test setup and the

unsteadiness of the flow, lateral or side-to-side asymmetry exists in the mainstream. Asymmetry can be minimized by averaging left and right side thermocouple data. All ramp, fan and normal trench data are presented as averaged values consisting of both the left and right sides at the 25 and 95-diameter distances. Radial trench injection inherently produces asymmetry due to its compound angle geometry. The radial trench impinges on the flow from right to left when referencing Figure III-1. Radial trench data is presented as right and left from the point of view shown in Figure III-1. Side-to-side deviation caused by the radial trench is not presented at the 95-diameter distance because the deviation was not significant

#### **IV.2 Data Analysis Techniques for Phase I and Phase II**

Results are presented in the same order as they are discussed in the previous section. Augmentation and heat flux will be presented first to determine if augmentation and heat flux are suitable methods for finding the best cooling configuration in a reacting flow. Normalized temperature is presented next to show worst-case conditions using the normal trench as the example configuration. Adiabatic wall temperature extrapolation is presented last to determine if this graphical method is a viable solution to find the adiabatic wall temperature.

Augmentation results are presented in series starting with phase I results which are immediately followed by phase II. Phase I and II results are not separated into different sections allowing for a trend comparison. A direct comparison of augmentation and heat flux values between phase I and II is not practical due to significant differences in wall temperatures as a result from changing heat sink properties. Phase II oil-cooled testing results typically show lower heat flux than the Phase I water-cooled testing. However, both testing methods should

show similar trends in performance with respect to each of the different cooling configurations. All figures and graphs indicate either phase I or II in the caption.

Phase I augmentation and heat flux compares the normal trench, fan and ramp configurations with and without upstream input. For series configurations, upstream input varies between offset normal and the slot. Fan results were taken from Bohan [17] and are repeated here for comparison purposes. Phase II compares the normal trench, radial trench and ramp configurations with and without upstream input. For series configuration, upstream input varies between offset normal and the slot. Phase II analysis uses corrected data, as shown previously, to compensate for changes in mainstream conditions.

Normalized wall temperature calculations are presented after the augmentation and heat flux analysis. Normalized wall temperature calculations are shown for the normal trench only. The normal trench does not change the mainstream conditions in the zero-zero case, as does the ramp, nor does it exhibit asymmetry as shown by the radial trench. Therefore, the normal trench is the ideal case to test the two methods for calculating normalized temperature.

Literature reviewed in the previous section shows data for film cooling within 25-diameters from the injection point. Most thin film cooling designs space injection locations within 95-diameters of one another. Therefore, the downstream thermocouples located at 95-diameters from the downstream cooling bay are not a primary focus of this thesis. Results for the 95-diameter distance are displayed only when significant. The majority of the following analysis will focus on the results from the 25-diameter distance.

### **IV.3 Augmentation**

Augmentation is the first analysis tool used to determine the impact of secondary reactions due to air injection. Augmentation allows one to find worst-case and best-case air cooling scenarios as compared to nitrogen. Nitrogen being inert, allows one to find the ideal cooling result with no secondary reactions. An air-cooled testing condition resulting in nitrogen cooling performance reveals best-case performance. All other augmentation results show the increase in heat flux above nitrogen as a relative indication of performance. Augmentation data contributes to the first and second objectives of this thesis. These objectives were specifically to identify appropriate analysis methods to find optimum film cooling conditions and to determine a method to minimize burning in the turbine under high fuel air ratio conditions

#### **IV.3.1 Phase I - Single Row Injection at 25 Hole Diameters**

Nitrogen is used to find performance without additional reactions. Nitrogen provides the baseline for the augmentation of heat flux for the fan, ramp, and normal trench configurations at an equivalence ratio of 1.3. For these investigations, blowing ratio is used as a parameter of interest in determining the changes in heat flux to the wall. Figure IV-1 provides this baseline nitrogen heat flux for the fan, ramp, and normal trench. These results are consistent with the general trends seen by previous researchers in this facility with other cooling hole configurations. Reference Bohan [17] and Evans [18] for comparison.

Switching to air as the coolant enabled the secondary reaction to occur. A significant increase in heat flux was experienced for all blowing ratios at an equivalence ratio of 1.3. As the blowing ratio increased Figure IV-2 reveals a steady incline in the heat flux. This was an

expected result as the increase in air supply near the wall added oxygen to the free stream. Increasing the air supply decreased the local equivalence ratio. As the local equivalence ratio approaches 1.0 the local adiabatic flame temperature increases causing the driving temperature for heat flux to increase. This subsequently results in a local increase in the heat flux to the surface.

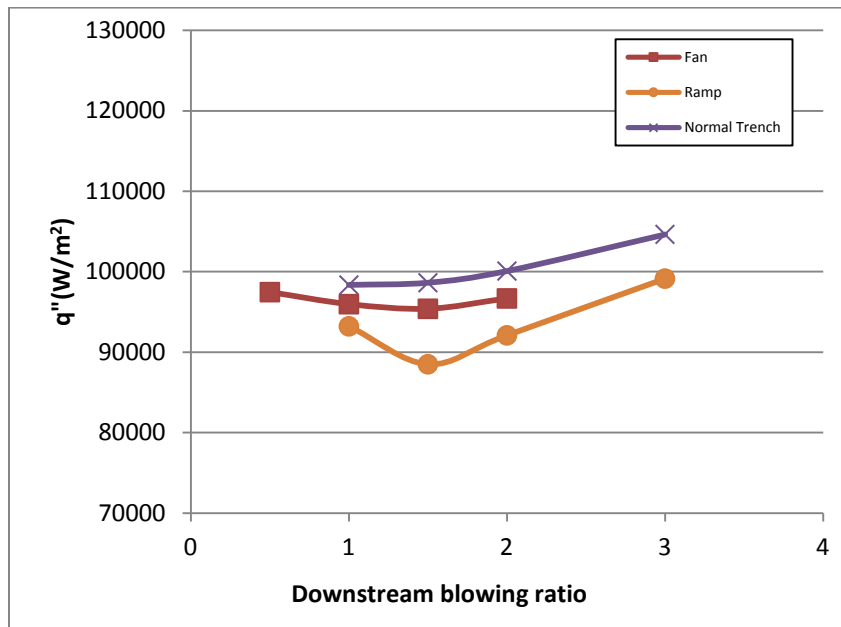


Figure IV-1. Phase I - N<sub>2</sub> injection at  $x/d_j = 25$ ;  
US: Blank, DS: Variable,  $\phi=1.3$

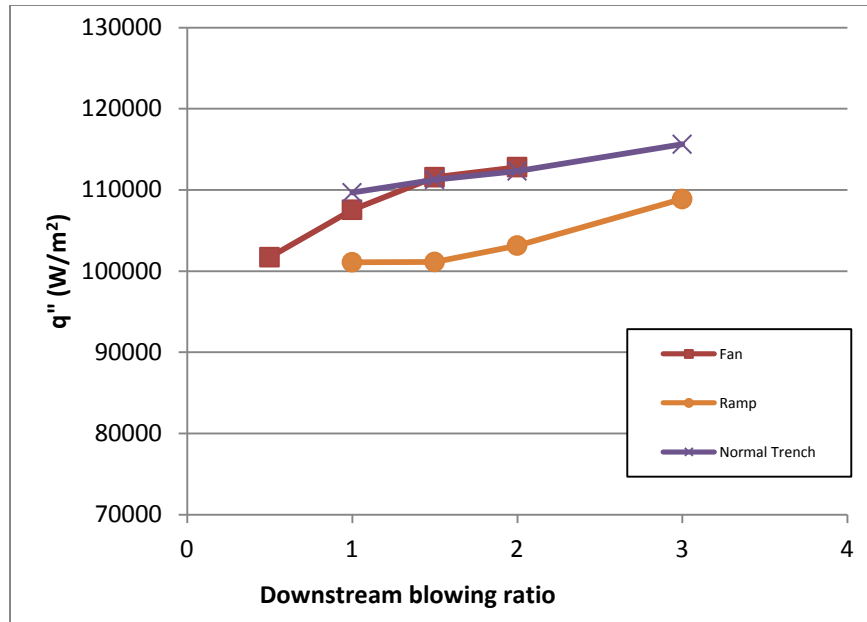


Figure IV-2. Phase I - Air injection at  $x/d_j = 25$ ;  
 US: Blank, DS: Variable,  $\phi = 1.3$

Investigating this data in the form of augmentation reveals the impact of the secondary reaction (Figure IV-3). The augmentation of heat flux for the fan configuration was substantial as shown previously by Polanka [14]. This sharp increase in augmentation indicated an increase in mixing causing the radical species to react within the 25-diameter distance. The ramp configuration shows a similar augmentation result. The ramp design intends to lift hot gases away from the surface causing secondary reactions to occur above the surface. The results shown in Figure IV-3 suggest that the ramp was unsuccessful at accomplishing this goal. It is believed this was due to the discrete holes used in both the ramp and the fan shaped row still enabling hot gases to penetrate between the holes and mix along the shear layers. For reference the hole pitch in the ramp and fan configuration is 7.6 and 3.8mm, respectively.

The normal trench case was relatively insensitive to blowing ratio resulting in nearly consistent heat generation between the nitrogen to air cases. A consistent heat flux augmentation

of nearly 12% illustrates the trenched design. Overall, the normal trench did a better job of spreading the coolant laterally and blocking the mainstream gas protrusion to the wall reducing the probability of secondary heat release.

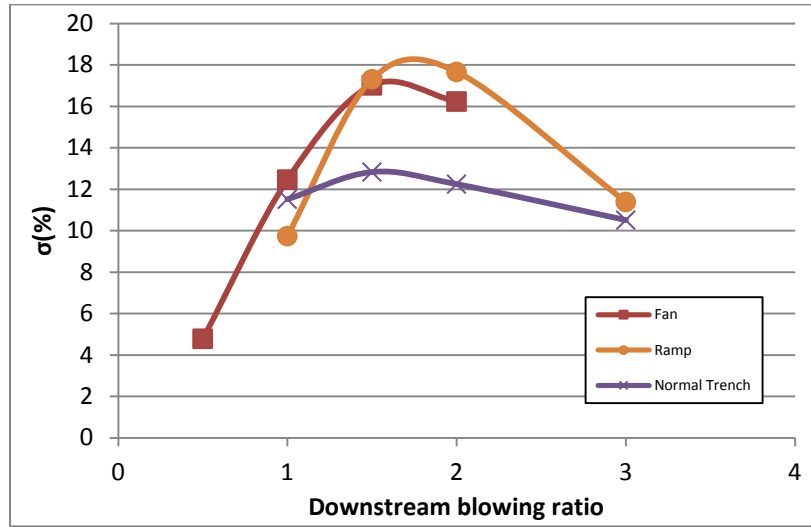


Figure IV-3. Phase I – Augmentation( $\sigma$ ) at  $x/d_j = 25$ ,  $\phi = 1.3$ ,  
US: Blank, DS: Variable

For all three designs, as the blowing ratio nears three the augmentation started to decline. This decrease is significant for the ramp configuration indicating fewer reactions taking place near the wall. This effect is a result of a local reduction in radical concentration due to the protection of the thicker coolant layer. Furthermore, with each configuration emitting a larger quantity of oxygen the local equivalence ratio may have decreased below 1.0 to a lean mixture reducing adiabatic flame temperature.

### **IV.3.2 Phase II - Single Row Injection at 25 Hole Diameters**

Phase II used corrected values and zero-zero data to normalize calculated heat flux minimizing the error in the test due to changing mainstream conditions. Phase II single row augmentation will show results using the ramp, normal trench, and radial trench. The objectives of phase II augmentation and heat flux analysis are the same as phase I. Phase II testing uses heated oil to cool the test plate instead of the water source used during phase I. The switch from water to oil was done primarily to minimize the error created by an uncontrolled inlet water temperature and pressure.

Figure IV-4, 5 and 6 compare heat flux for the radial trench, ramp, and normal trench configurations at an equivalence ratio of 1.3. Nitrogen and air are used as the coolants to provide a direct comparison as well as to find augmentation. Figure IV-4 presents increasing blowing ratio using nitrogen as the coolant with the ramp, radial trench and normal trench. The radial trench is positioned such that the fluid is pushed to the left side of the flat plate when referencing Figure III-1.

As a result of the coolant traveling from right to left, the radial trench-left side experiences a significantly lower heat flux than the radial trench – right side. A lower heat flux is an indication of a lower local gas temperature due to the coolant exiting to the left. The relative aspect of the radial trench left and right sides is not as important as the direction of change in heat flux. The radial trench and ramp show an increase in heat flux between a blowing ratio of 2 and 3 indicating coolant separation and/or an increase in the convective coefficient. The normal trench continues to decrease heat flux with increased blowing ratios and shows the lowest overall heat flux.

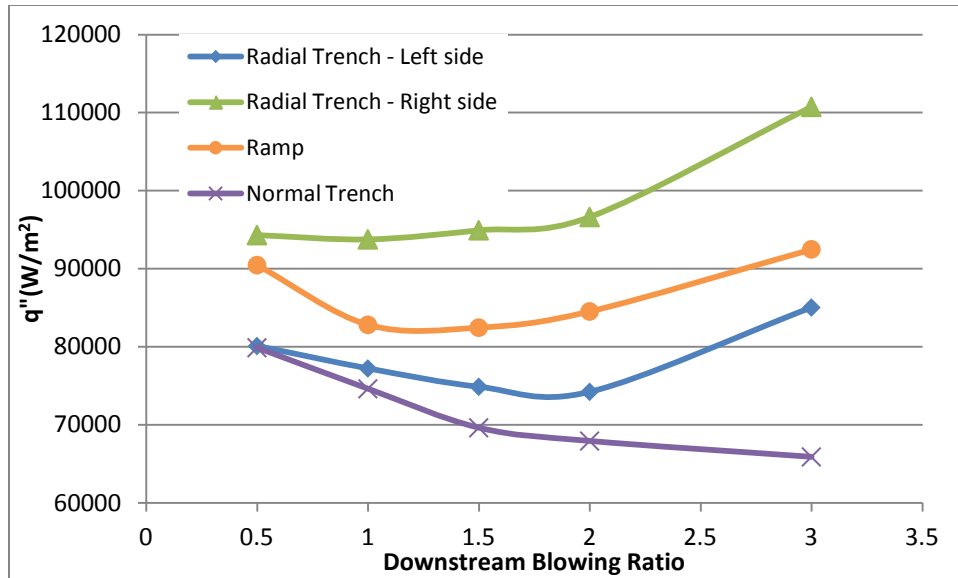


Figure IV-4. Phase II - N<sub>2</sub> injection at x/d<sub>j</sub> = 25;  
US: Blank, DS: Variable, φ=1.3

As discussed previously in section III.6, zero-zero data is used to correct all Phase II data. Figure IV-5 shows an example of the difference between corrections made on the ramp and the normal and radial trenches. The correction factors intend to minimize the error seen in phase I testing by correcting for the offset in mainstream conditions due to fluctuations in the combustor pressure. Zero-zero conditions are shown in Figure IV-5 to discuss the differences between baseline configuration results.

Figure IV-5 shows the heat flux for the air injection case for the ramp and trenched conditions. As indicated in the figure, for a blowing ratio of zero, the ramp displays a significantly higher base heat flux level. This is consistent with the zero-zero data shown in Section III.6. The ramp's higher convection coefficient, due to the ramp's protrusion into the mainstream, is the primary cause of the increased heat flux in the zero-zero condition. However, the ramp's increased starting heat flux is overtaken by the other configurations as the blowing ratio increases. The radial and normal trenches both exhibit an increase in heat flux as the

blowing ratio increases. The slight decrease in the normal trench performance between a blowing ratio of 2 and 3 could be another indication of reaching the range where peak adiabatic flame temperature is possible. Figure IV-5 shows the ramp as the best performing configuration between a blowing ratio of 1.0 and 2.0. Additionally, each configuration seems to approach the same heat flux as the blowing ratio approaches 3.0.

Another interesting observation, in Figure IV-5, is the side-to-side variation in radial trench heat flux. There exists a left to right deviation in the zero-zero condition as indicated by the left most data points on the vertical axis. This shows the mainstream conditions are asymmetric and not just a product of the radial trench injection. Asymmetry in the mainstream must be considered in the analysis of the radial trench.

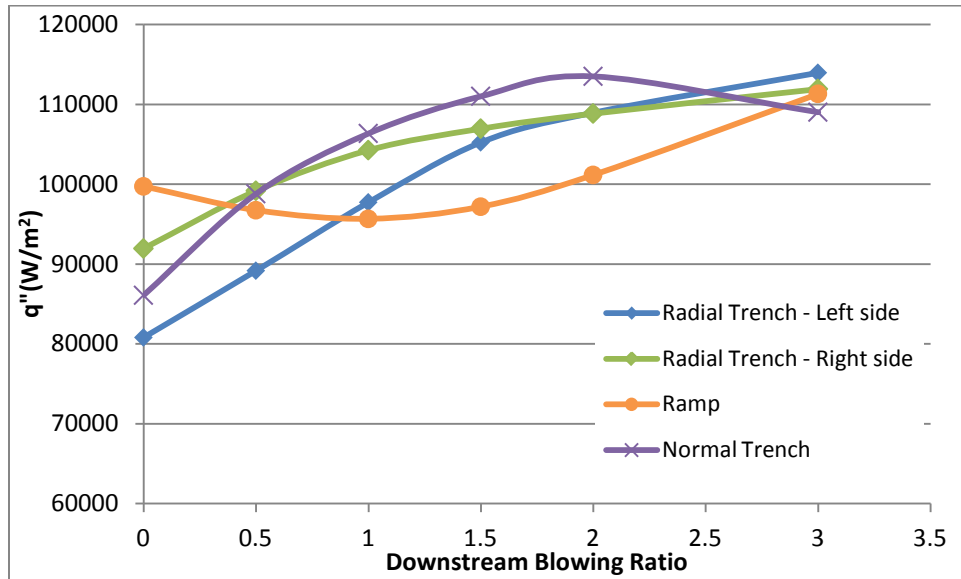


Figure IV-5. Phase II - Air injection at  $x/d_j = 25$ ;  
US: Blank, DS: Variable,  $\phi = 1.3$

Figure IV-6 shows augmentation for the radial trench, normal trench and ramp configurations. The normal trench has the highest augmentation of any configuration. The

highest augmentation is a direct result of the normal trench having the highest performance in the nitrogen case and the worst performance in the air case. This is in contrast to the phase I results. Phase I showed the normal trench as having the best augmentation results and the worst performance in both the air and nitrogen cases. This contrast speaks to the value of a correction factor. Additionally, Figure IV-6 shows the radial trench, normal trench and ramp all hitting a peak augmentation between a blowing ratio of 2.0 and 3.0. This corresponds with the initial result of a worst-case  $\phi$  near 1.3 at a blowing ratio of 2.0.

Additionally, the normal trench is similar to the fan in regards to the secondary reactions. The normal trench configuration applies a good film cooling layer which minimizes the heat flux for the nitrogen case. Since the oxygen is maintained close to the wall, the reaction occurs close to the wall. This effect elevates the heat flux for air higher than the ramp where the oxygen is pushed off the wall. This effect results in high augmentation as shown previously with the fan configuration.

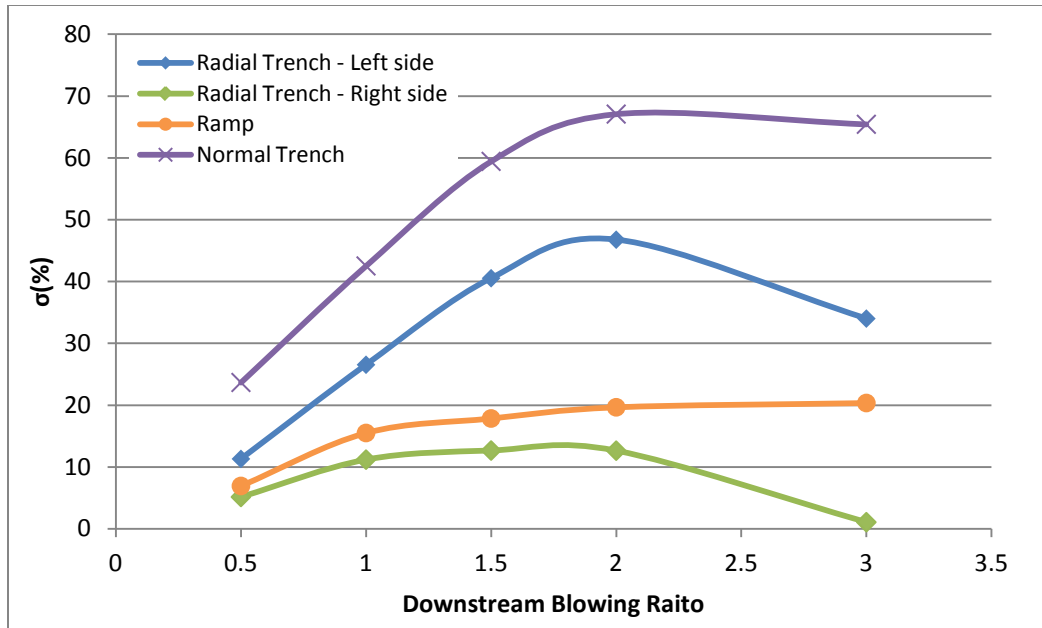


Figure IV-6. Phase II – Augmentation( $\sigma$ ) at  $x/d_j = 25$ ,  $\phi = 1.3$ ,  
US: Blank, DS: Variable

A visual comparison can also be made between the three configurations (normal trench, radial trench, and ramp) using photographs taken during phase II of testing. Figure IV-7 shows photographs of the normal trench, radial trench and ramp from left to right, respectively. The blue flame is an indication of the reactions taking place. When comparing the trenched cases to the ramped case it appears that the ramped configuration creates downstream reactions that are lifted off the surface and are further from wall. This may indicate why the ramp has a lower augmentation than the other two configurations.

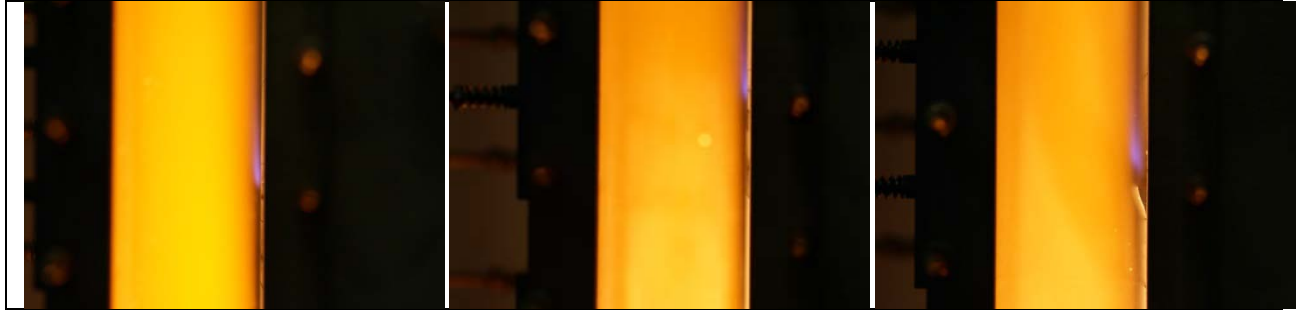


Figure IV-7. Phase II – From left to right: normal trench, radial trench and ramp,  $\phi=1.3$ , US: Blank, DS: Variable

### IV.3.3 Phase I - Single Row Injection at 95 Hole Diameters

After looking at the augmentation at 25-diameters, the heat flux at the downstream location (95-diameter) was analyzed. Figure IV-8 shows the nitrogen coolant data at this location. Subsequently, Figure IV-9 shows the data for the same three geometries using air as the coolant. Results shown in both figures indicate little change in heat flux with additional coolant flow. The literature has shown that coolant is typically not effective at this large a distance from the hole. Additional distance allows more mainstream air to mix with the coolant flow and even the temperature distribution prior to reaching the 95-diameter distance. The flame has ended well upstream of this location as shown in Figure III-17 and 18. Therefore, the primary impact of the secondary reaction was to raise the freestream temperature at the 95-diameter distance and thus the overall heat flux.

Testing at 95-diameters indicates the ramp and normal trench increase downstream local fluid temperature. Elevated downstream temperatures could be a result of the increased volume flow rate from the ramp and normal trench due to twice the additional exit area over the fan. However, it is unlikely that this is the only contributing factor to the elevation in temperature or convective coefficient. Repeatability is believed to play a large role in this test resulting in the

large difference in heat flux. Phase I augmentation results at 95-diameters look inconclusive when trying to compare configuration to configuration. Large differences between the three tested configurations should not exist at this distance. A difference of ~15% between the fan results and the normal trench suggest the possibility of different mainstream conditions.

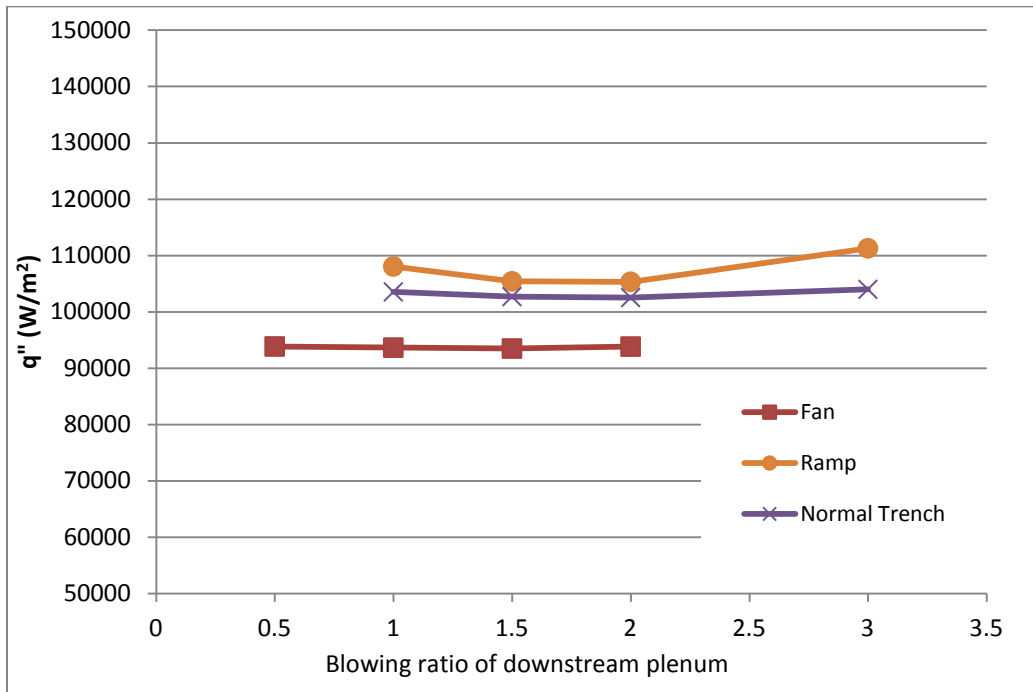


Figure IV-8. Phase I – N<sub>2</sub> injection at  $x/d_j = 95$ ;  
 US: Blank, DS: Variable,  $\phi = 1.3$

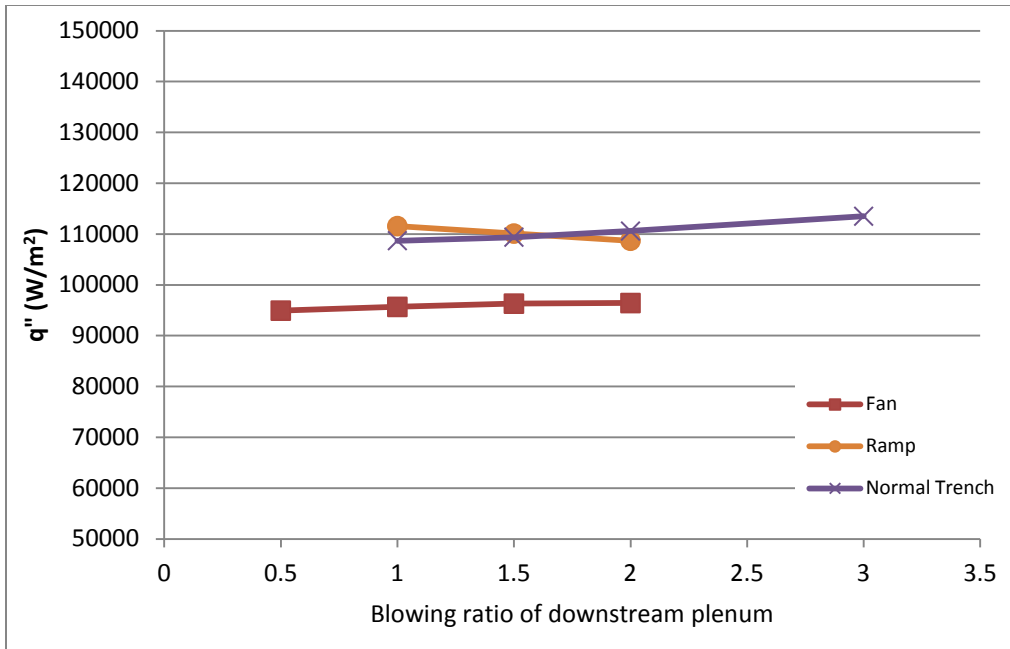


Figure IV-9. Phase I - Air injection at  $x/d_j = 95$ ;  
 US: Blank, DS: Variable,  $\phi = 1.3$

Phase I augmentation results, shown in Figure IV-10, at 95-diameters reveal significantly lower augmentation levels as compared to the 25-diameter distance, shown in Figure IV-3. All three configurations reveal a general trend of increasing augmentation as the blowing ratio increased. As discussed earlier, this was expected due to a higher upstream heat release with more coolant interacting with the fuel rich freestream resulting in a higher downstream temperature. Differences in volume flow rates may be a contributing factor due to the fan having half of the number of holes and thus a smaller total exit area than the ramp and trench.

The reduction of the level of augmentation for the ramp with respect to the normal trench was attributed to the ramp lifting the hot gases off the surface, thus mixing with the hot gases further from the surface. Both the normal trench and ramp create similar surface temperatures of 630 K at the 95-diameter distance indicating that the driving temperature for the normal trench increased more during the switch from nitrogen to air.

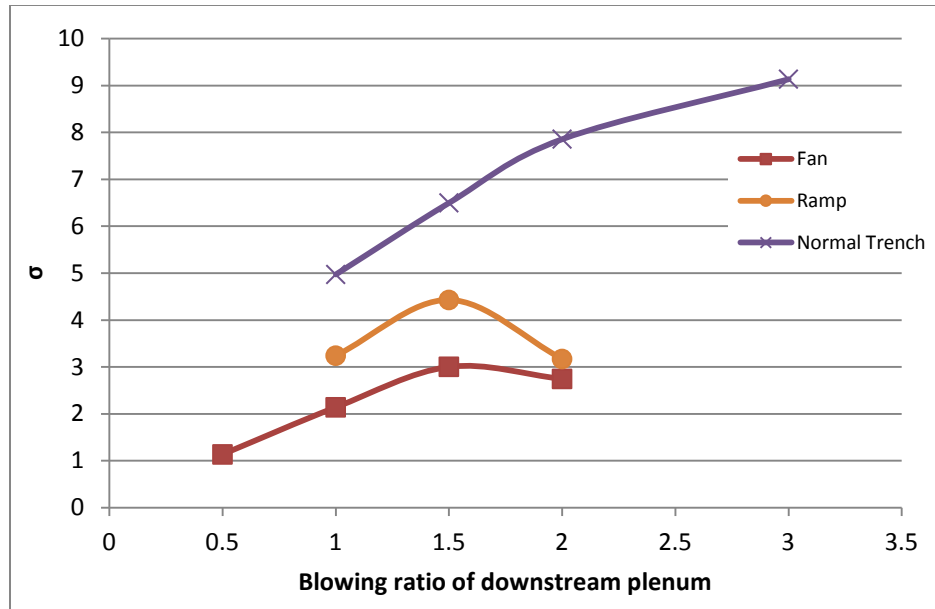


Figure IV-10. Phase I – Augmentation ( $\sigma$ ) at  $x/d_j = 95$ ,  $\phi = 1.3$ ,  
US: Blank, DS: Variable

#### IV.3.4 Phase II - Single Row Injection at 95 Hole Diameters

Phase II data at 95-diameters will now be examined. Figure IV-11 shows nitrogen testing results for the normal trench, radial trench and ramp configurations tested during phase II. Figure IV-12 shows air results for each of the three configurations tested during phase II. As discussed previously, large changes or differences in heat flux are not expected at this distance due to the dissipative effects caused by the additional distance downstream. Expected results should consist of relatively small changes in heat flux between blowing ratios of a particular configuration, as shown in phase I data at 95-diameters.

Figure IV-11 shows the normal trench as having a significant reduction in heat flux over the range of tested blowing ratios. This is not an expected result and is attributed to uncorrected error. However, the ramp's resulting heat flux over the range of blowing ratios appears flat with a slight decrease in heat flux with increasing blowing ratio. Both air and nitrogen testing reveal a

downward trend in heat flux when using the ramp configuration. It is proposed that the additional flow does serve to cool the downstream wall with the reactions lifted for this geometry.

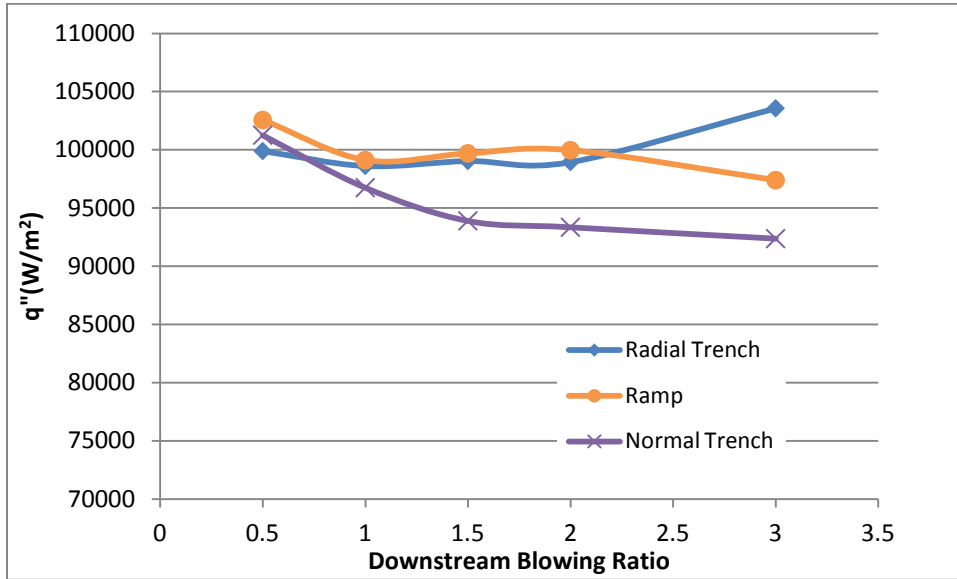


Figure IV-11. Phase II – N<sub>2</sub> injection at x/d<sub>j</sub> =95;  
US: Blank, DS: Variable, φ=1.3

Figure IV-12 shows similar heat flux magnitudes between the normal trench and the other configurations. Figure IV-12 shows the radial trench exhibiting an increase in heat flux while the ramp and normal trench show a decrease in heat flux as the blowing ratio increases. Each of the configurations shows similar performance between a blowing ratio of 1.5 and 2. Figure IV-12 results show good agreement between the different configurations. As stated previously results shown at 95-diameters should be relatively flat with small differences between configurations.

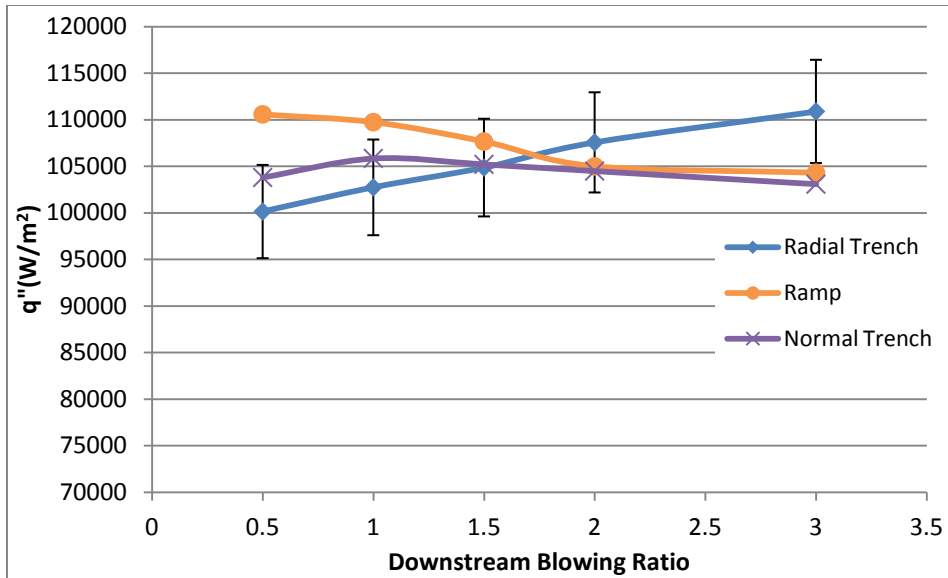


Figure IV-12. Phase II - Air injection at  $x/d_j = 95$ ;  
 US: Blank, DS: Variable,  $\phi = 1.3$

The error potential for each data point is shown on Figure IV-12 for the radial trench only. The error bars shown are calculated using the standard deviations and the 95% confidence in the mean at the 95-diameter location, shown in Table III-4. The majority of the data (95%) should fall within two standard deviations of the mean assuming standard distribution. The upper variance in the mean, using the 95% confidence level, represents the potential error in the mean due a small data sample. As a percentage, two standard deviations added to the upper end of the variance in the mean yields a potential error of around 5%. The error bars shown in Figure IV-12 correspond to an error of 5% for the radial trench only. Phase I results yielded much flatter heat flux profiles but with large differences between configurations. Phase II results yielded flat profiles without large differences between configurations.

Figure IV-13 shows augmentation for each configuration at the 95-diameter distance. The ramp and radial trench exhibit the best augmentation performance above a blowing ratio 1.0. The normal trench keeps the fluid closest to the wall allowing for the highest augmentation and

heat flux. The normal trench has proven to be the worst performer in augmentation and heat flux, when using air, at both the 25 and 95-diameter locations.

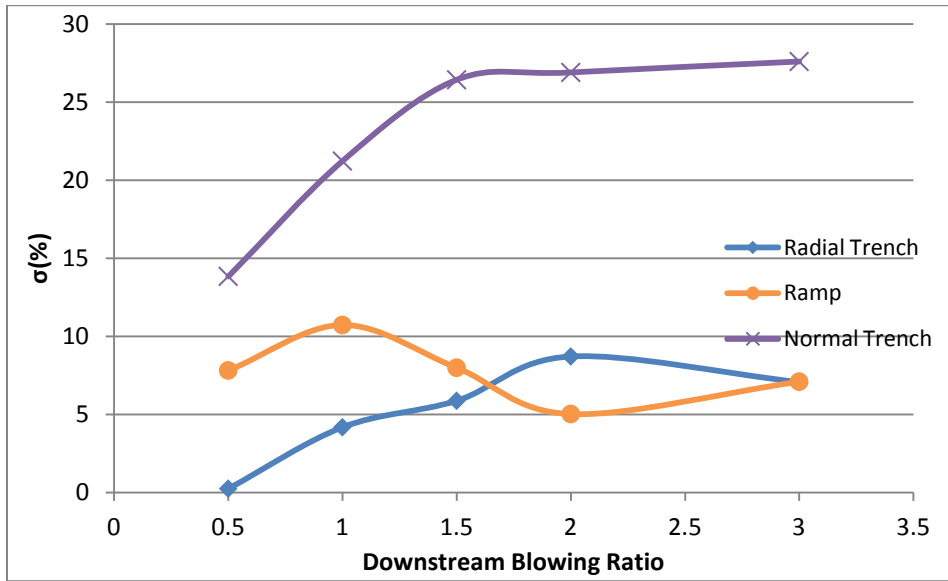


Figure IV-13. Phase II – Augmentation ( $\sigma$ ) at  $x/d_j = 95$ ,  $\phi = 1.3$ ,  
US: Blank, DS: Variable

#### IV.3.5 Phase I - Series Injection Data at 25 hole diameters

Augmentation and heat flux data analysis will now be applied to series film cooling. Series film cooling uses both upstream and downstream bays to test different configurations at various upstream blowing ratios. For all series testing the upstream blowing ratio is varied while the downstream blowing ratio is held constant at 2.0. The upstream row injects air in all cases while the downstream switches between nitrogen and air. Phase I series configurations consist of the offset normal configuration and slot upstream of the fan, normal trench and ramp. The upstream coolant designs selected simulate the extremes of boundary conditions that could affect the downstream film coolant row. These upstream cooling bays are a slot and an offset normal design. Phase I series configuration consist of the offset normal configuration or the slot

upstream of the fan, normal trench and ramp. The following phase I data will be evaluated using augmentation and heat flux to determine the differences in performance of each configuration.

The upstream cooling bay is physically 25-diameters upstream from the downstream bay and results for the cases with the upstream coolant are referenced to the upstream row. With the measurement locations in the same physical position, the results for this testing are now located at  $x/d_j$  equal to 51 and 125-diameters, reference Figure III-1. The upstream coolant bay, slot or offset normal, injects air in all cases while the downstream bay injects either air or nitrogen. For all series testing the downstream bay is held at a constant blowing ratio of 2.0. Switching the downstream coolant between air and nitrogen allows one to determine if additional reactions are present due to the additional downstream oxygen. Augmentation is now a representation of how much mainstream fuel is making it past the offset normal's or slot's injected air to find the ramp's, radial's or normal trench's coolant. Therefore, augmentation will help determine the effect of upstream coolant ejection on downstream performance.

During initial offset normal testing, results indicated small changes as shown in Figure IV-15 and Figure IV-16. As the upstream (offset normal) blowing ratio was changed and the downstream blowing ratio held constant at two, heat flux and augmentation remained nearly constant in each configuration. The fan experienced the lowest overall heat flux accompanied by the highest overall augmentation. This is an expected relationship due to the relative aspect of the measurement taken. Since augmentation is on a percentage basis, if all cases raise the temperature of the local gas the same amount, the cooling configuration with the lowest overall heat flux in the nitrogen case will have the highest overall augmentation. This relationship is also apparent when referencing Figure IV-15 and Figure IV-14.

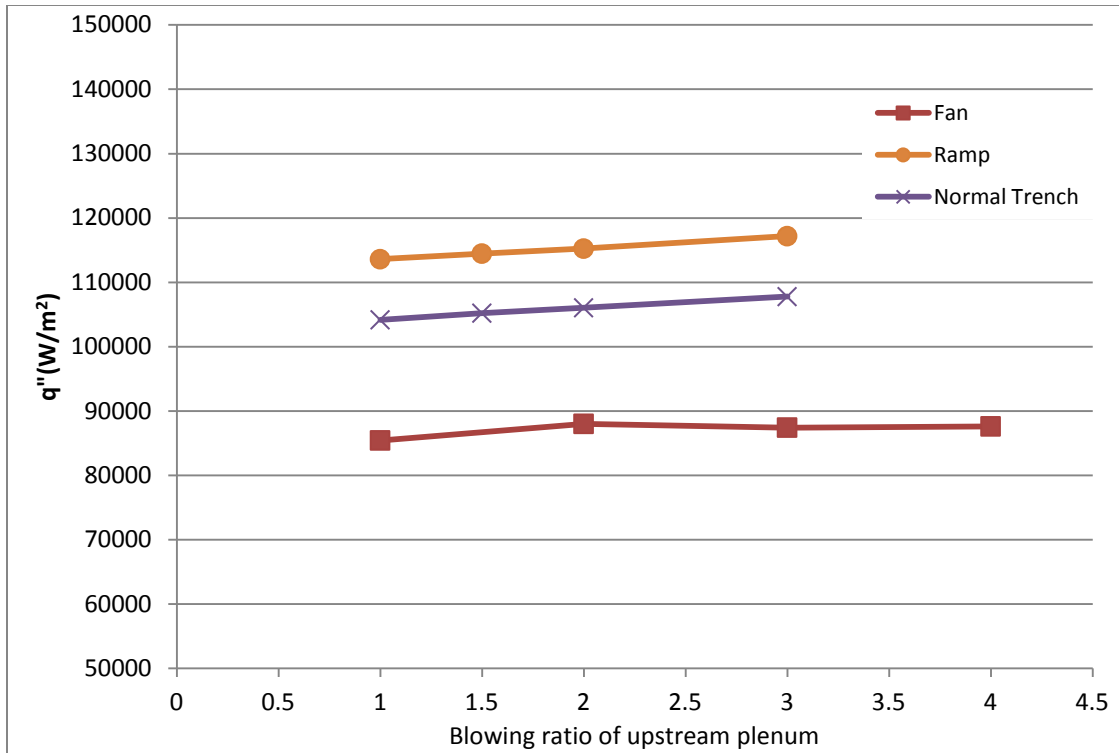


Figure IV-14. Phase I - Heat flux for N<sub>2</sub> injection at  $\phi=1.3$ ,  $x/d_j = 51$ , US: Offset normal, DS: M=2.0, Geometry = Variable

A relatively constant augmentation trend in each configuration indicated the insignificance of coolant volume of the upstream offset normal holes. Since this coolant was ejected off the surface it does not shield the downstream row. However, increasing the amount of oxygen ejected from the offset normal plenum should change the local free radical concentrations. For an upstream  $\phi = 1.3$ , the relatively small amount of increased oxygen served only to reduce the local free radical concentration by a small amount. This oxygen was also spread vertically away from the wall. Not enough oxygen stays close to the surface to decrease the local downstream equivalence ratio. In a typical combustor liner several rows of these holes are used to increase the total mass of coolant. In this study, two offset rows may not introduce

enough oxygen to significantly decrease the quantity of reactive species. This possibility influenced the decision to eject higher blowing ratios from these holes in phase II testing to increase the overall oxygen content as will be seen in Section IV.3.6.

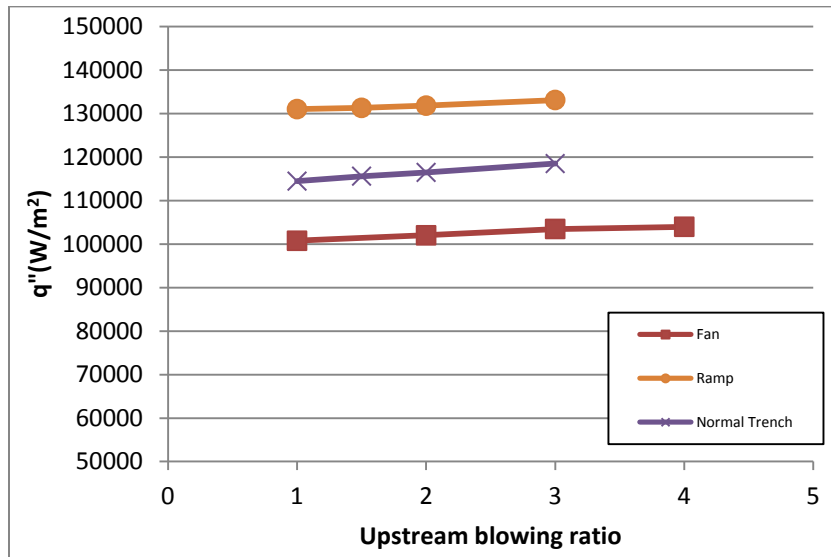


Figure IV-15. Phase I - Heat flux for air injection at  $\phi=1.3$ ,  $x/d_j = 51$ , US: Offset normal, DS:  $M=2.0$ , Geometry = Variable

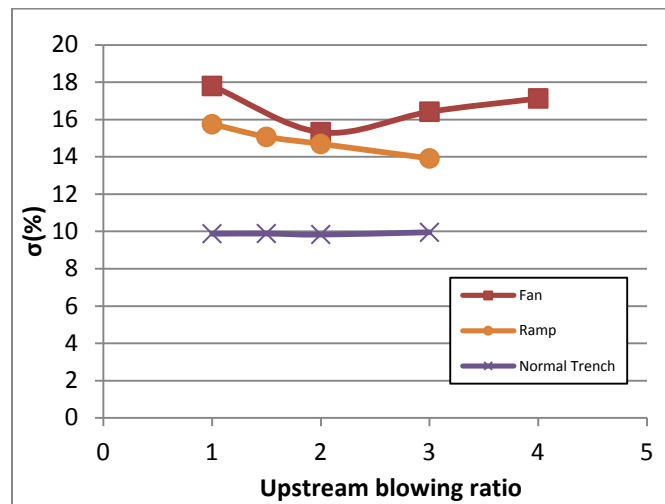


Figure IV-16. Phase I – Augmentation ( $\sigma$ ), at  $\phi=1.3$ ,  $x/d_j = 51$ , US: Offset normal, DS:  $M=2.0$ , Geometry = Variable

The second upstream cooling configuration tested was a slot. Slot cooling is used in the majority of modern combustor design. Angled slots, like the one used in this test, provide a low orthogonal velocity component and stay close to the wall. Slot testing is performed in a similar fashion to the offset normal testing with a downstream blowing ratio held constant at two and a variable upstream (slot) blowing ratio. Figure IV-17 shows the results for the three downstream geometries investigated. As the blowing ratio of the slot is increased, significant reductions in heat flux were experienced. Data shows the fan and normal trench have the lowest overall heat flux and the greatest positive impact due to the upstream slot. For these configurations, the slot is providing a protective layer of coolant that is reducing the heat load to the surface. This combination of an upstream slot with a downstream low momentum ratio ejection configuration, results in a highly effective strategy for mitigation of the turbine burning problem.

However, for the ramp configuration, the cool fluid from the slot is lifted away from the surface. Mainstream and slot fluid are now subject to the same circulation produced by the upstream facing step and opposing low-pressure region on the downstream side of the step. This pressure gradient serves to pull fluid from the mainstream enhancing the mixing process, hence the increase in the convective coefficient. Increasing the blowing ratio of the slot reduced the heat flux for the ramp configuration but not to the same extent as the other cooling geometries.

The ramp data, when in series with the slot, reveals an interesting characteristic. All configurations produce zero augmentation when the slot is at a blowing ratio of one. However, the ramp has the highest heat flux in all blowing conditions. The data suggests the significant impact of the ramped protrusions' effect on local mixing. If a higher heat flux is present yet no additional reactions are occurring due to the injection of air at the 25-diameter distance, as indicated by zero augmentation, then the local fluid temperature and/or the convective heat

transfer coefficient must be greater. This becomes more clear when comparing Figure IV-17 and 18. We know the fluid temperature can rise due to the increase in circulation however, additional mainstream air would create additional reactions with the air injected from the downstream ramp. This indicates that the increased heat flux experienced when using the ramp is primarily due to the increase in the convective heat transfer coefficient.

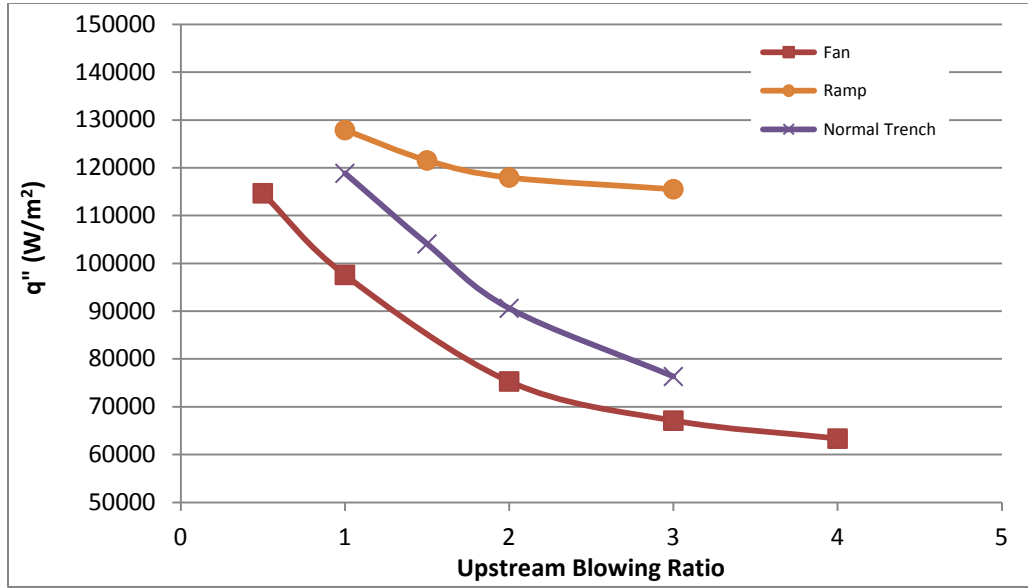


Figure IV-17. Phase I - Heat flux for air injection, at  $\phi=1.3$ ,  $x/d_j = 51$ , US: SLOT, DS: Variable

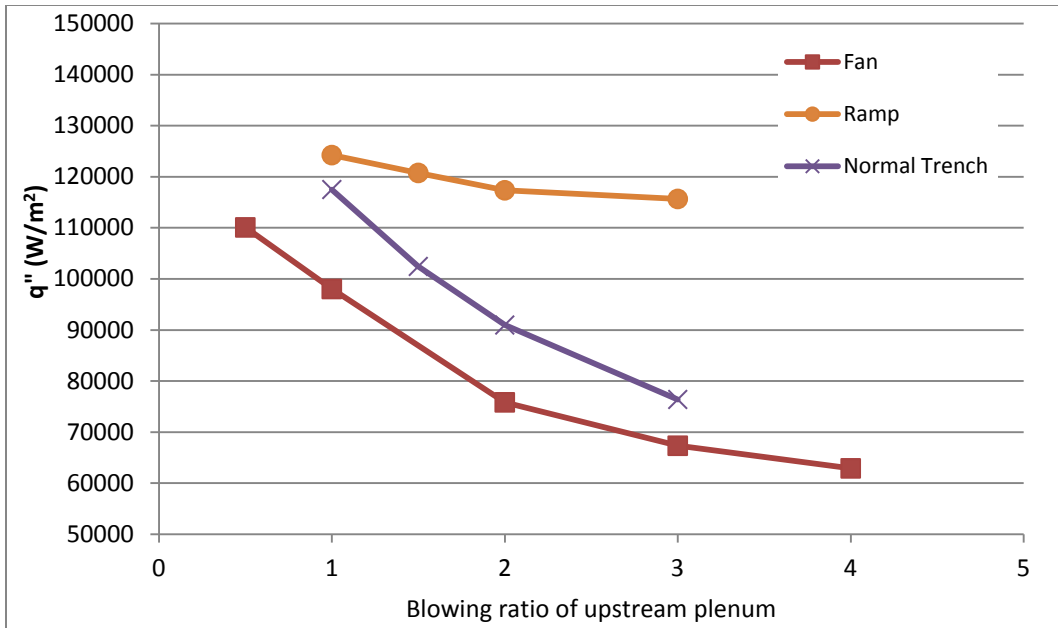


Figure IV-18. Phase I - Heat flux for N<sub>2</sub> injection, at  $\phi=1.3$ ,  $x/d_j = 51$ , US: SLOT, DS: Variable

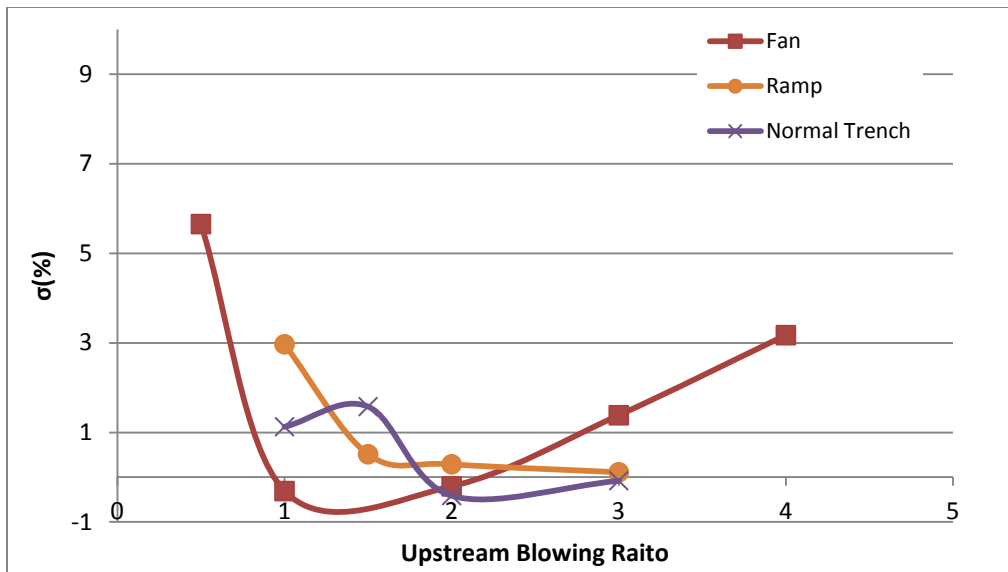


Figure IV-19. Phase I – Augmentation ( $\sigma$ ), at  $\phi=1.3$ ,  $x/d_j = 51$ , US: Slot, DS: Variable

#### **IV.3.6 Phase II - Series Injection Data at 51 hole diameters**

Phase II series injection data at 51-diameters is obtained using the same process as Phase I. For all series testing the upstream blowing ratio is varied while the downstream blowing ratio is held constant at 2.0. The upstream row injects air in all cases while the downstream switches between nitrogen and air. Phase II configurations tested include the ramp, normal trench and radial trench in the downstream location with either the offset normal or slot in the upstream location. Results are presented the same as phase I with calculated heat flux, using air as the coolant in the downstream bay, followed by augmentation. The upstream coolant bay, slot or offset normal, injects air in all cases while the downstream bay injects either air or nitrogen. Switching the downstream coolant between air and nitrogen allows one to determine if additional reactions are present due to the additional downstream oxygen.

Figure IV-20 shows phase II testing results for series injection using the offset normal configuration upstream of the ramp, normal trench and radial trench. Radial trench is split between the left and right to show the lateral offset present due to the coolant being blown to the left side. Data was taken between a blowing ratio of 0.5 to a blowing ratio of 10. This blowing ratio range was chosen primarily to provide similar volume flow rates when comparing offset normal results to the slot.

Figure IV-20 shows little asymmetry in radial trench data at a blowing ratio of 2.0 with an upstream offset normal blowing ratio of 0.5. This was noticed previously in Figure IV-5 at a blowing ratio of 2.0 from the radial trench. As the upstream blowing ratio increases the lateral offset in the radial trench case increases. One would think the increased upstream air would act to level the side-to-side variation because of a more even distribution. However, the radial velocity component may be creating a local radial velocity gradient, which is entraining the

upstream air from the offset normal. This local radial velocity gradient is overloading the left side of the test section. The additional air is creating a decrease in heat flux on the left side but not on right side of the test section. When the blowing ratio increases above three, the radial velocity effects are overcome due to the upstream coolant separating from the wall. As blowing ratio increases, momentum ratio also increases and the downstream velocity gradient no longer entrains the offset normal coolant.

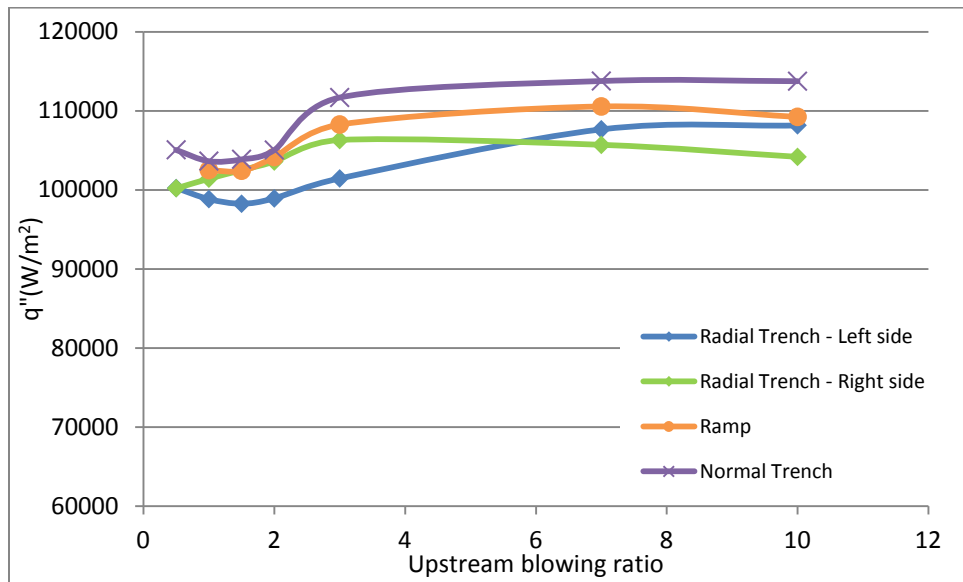


Figure IV-20. Phase II - Heat flux for air injection at  $\phi=1.3$ ,  $x/d_j = 51$ , US: Offset normal, DS:  $M= 2.0$ , Geometry = Variable

Again, the normal trench data shows the worst performance in both Figure IV-20 and Figure IV-22. This was noted before in the individual comparisons of phase I and phase II. This is attributed to the normal trench keeping the coolant close to the wall allowing reaction to complete near the surface. This trend persists through each portion of both the Phase I and II analysis sections with exception to the phase I, 25-diameter data shown in Section IV.3.1.

Another interesting feature of Figure IV-20 is the initial decrease in heat flux between upstream blowing ratios of 0.5 and 1.5 for ramp, normal trench and radial trench-left side. This

data suggests the upstream injection from the offset normal having a positive effect on downstream performance by reducing local heat flux. This initial decrease is also shown as augmentation in Figure IV-22.

Additionally, Phase I series data, using the offset normal upstream shown in Figure IV-15, does not agree with phase II series data shown in Figure IV-20. Phase I normal trench series data shows better performance relative to the ramp configuration. Phase II data shows the normal trench having worse performance than the ramp configuration. The offset shown in Figure IV-15, between the normal trench and ramp, shows significant differences in heat flux. This suggests dramatic performance improvements when using the normal trench. However, the phase II corrected data shows the normal trench as having the worst performance of any of three configurations. This inconsistency is mostly likely due to the unknown day-to-day offset error in the phase I results. Figure IV-21 shows the corresponding nitrogen plot for the offset normal upstream injection at 51-diameters.

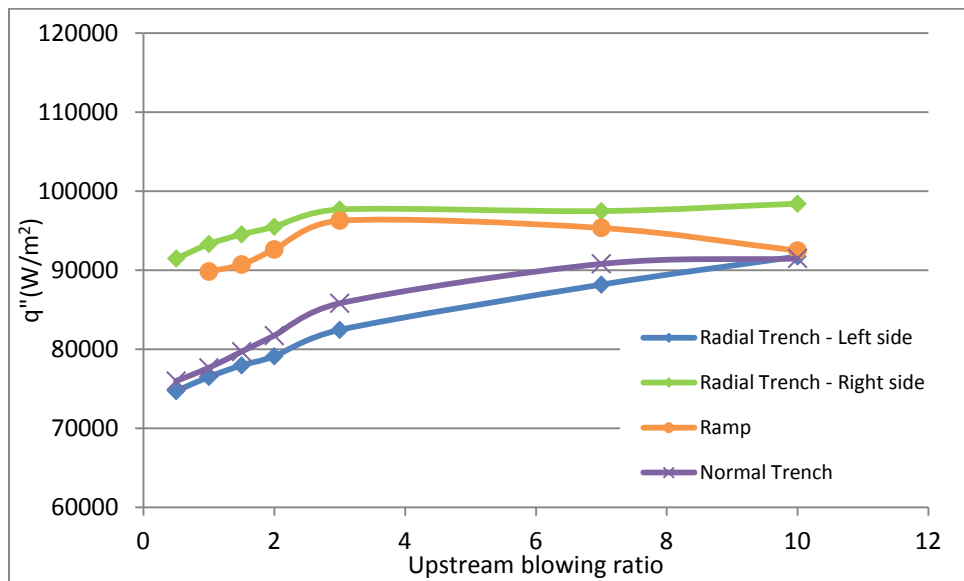


Figure IV-21. Phase II - Heat flux for N<sub>2</sub> injection at  $\phi=1.3$ ,  $x/d_j = 51$ , US: Offset normal, DS: M= 2.0, Geometry = Variable

The ramp data, shown in Figure IV-22, shows an increasing augmentation at blowing ratios greater than three suggesting a slightly worse performance at higher upstream blowing ratios. This indicates the heat flux generated in the air case is growing faster with increasing blowing ratio than the respective nitrogen case. As a result the augmentation is increasing above an upstream blowing ratio of three. Earlier discussion and results of the ramp indicated a higher convective coefficient and mixing due to the protrusion into the mainstream. The increase shown in Figure IV-22 could be the result of the increased mixing causing a higher heat load to the surface.

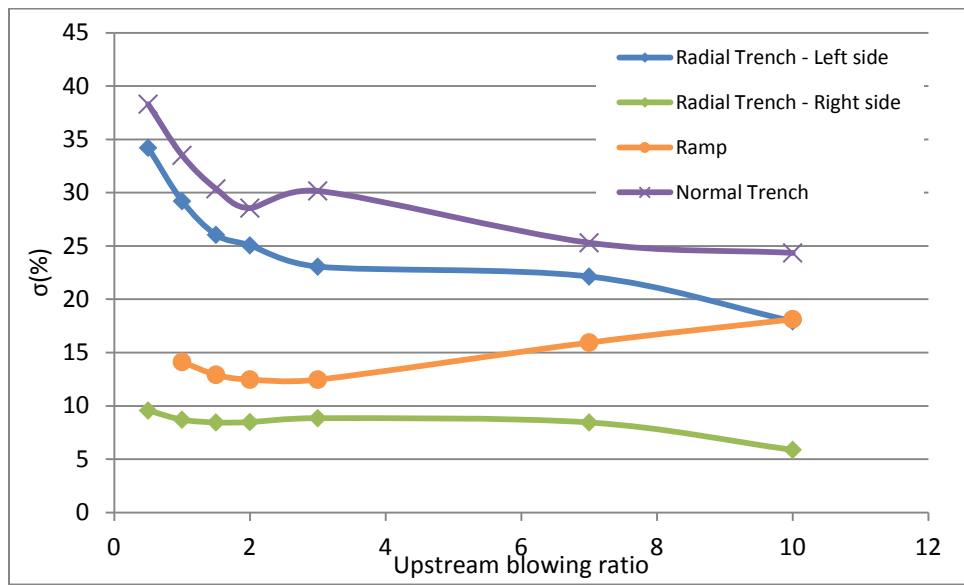


Figure IV-22. Phase II – Augmentation ( $\sigma$ ), at  $\phi=1.3$ ,  $x/d_j = 51$ , US: Offset normal, DS:  $M= 2.0$ , Geometry = Variable

Phase II also contains a second set of series configuration data with the slot in the upstream location. Unfortunately, the last day of testing ended short due to the reactor core degrading to an unusable point. Therefore, ramp series data using an upstream slot was not

completed. Only the radial and normal trench series data, using the upstream slot, can be shown in this section.

Figure IV-23 contains radial and normal trench series data with the slot in the upstream location. The downstream and upstream bays are ejecting air at every blowing ratio. The horizontal axis in all series plots represents the upstream blowing ratio; the downstream blowing ratio is held constant at 2.0. Both trenches exhibit a decreasing heat flux as upstream blowing ratio increases. Phase I also shows the same trend with respect to increasing blowing ratio from the slot. Note that the respective zero-zero point for the 51-diameter point is the same as the previously mentioned 25-diameter point in Table III-4, which shows the statistical analysis and mean values. At an upstream blowing ratio of 1.0 the resulting heat flux, when using the normal trench in series with the slot, is below the baseline value of  $\sim 85500 \text{ W/m}^2$ . This shows the ability to cool a downstream surface in a reacting environment. Furthermore, the cooling effectiveness increases dramatically with increasing blowing ratio.

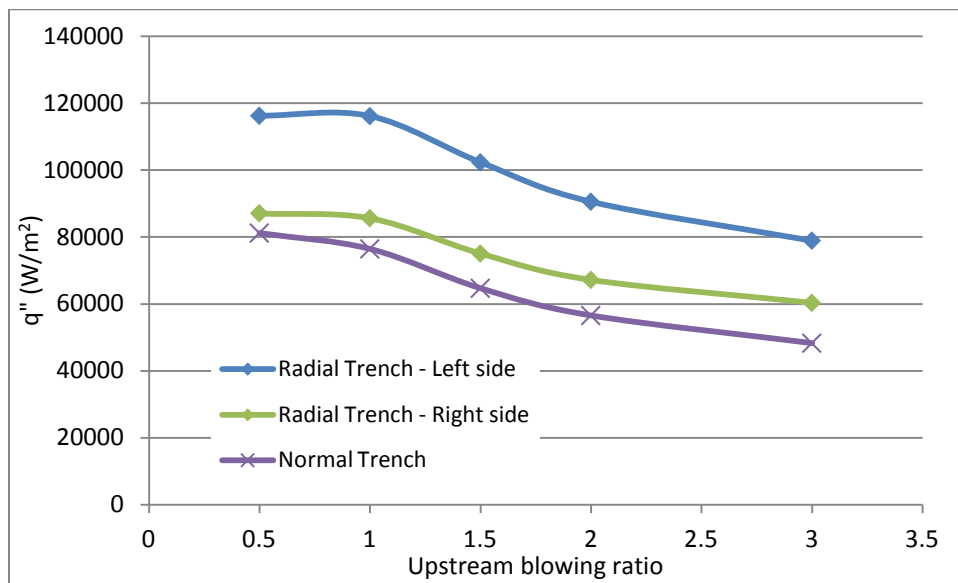


Figure IV-23. Phase II - Heat flux for air injection, at  $\phi=1.3$ ,  $x/d_j = 51$ , US: SLOT, DS: Variable

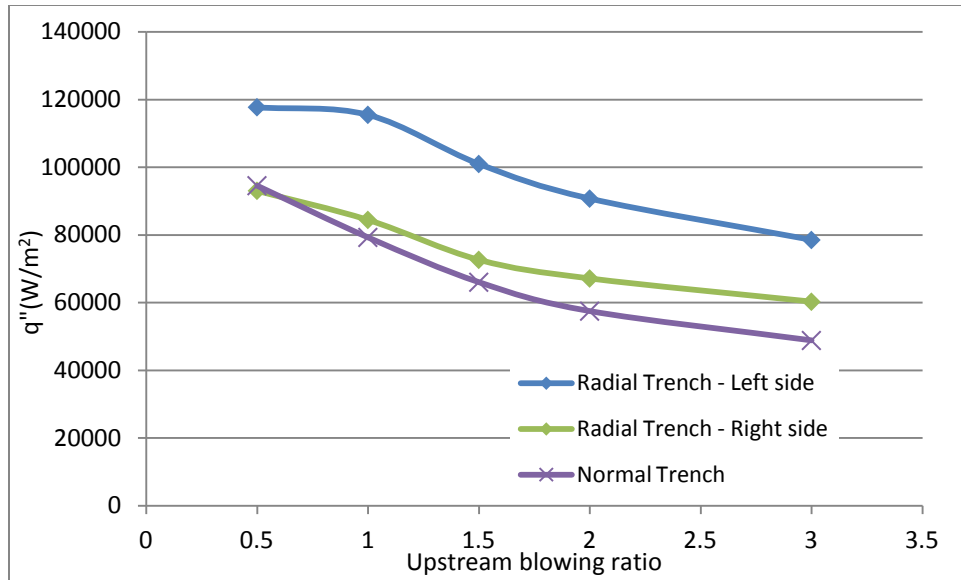


Figure IV-24. Phase II - Heat flux for N<sub>2</sub> injection, at  $\phi=1.3$ ,  $x/d_j = 51$ , US: SLOT, DS: Variable

Augmentation results are shown in Figure IV-25 for phase II series data using the slot in the upstream bay and the normal trench and radial trench in the downstream bay. Trends are similar to those shown in phase I with decreasing augmentation as blowing ratio increases. The radial trench data results in a negative augmentation at several blowing ratios. A negative augmentation is not possible due to nitrogen and air having only slight differences in density and specific heat as compared to air. Therefore, a negative augmentation represents the error present in the calculation, correction factors, and data acquisition which correspond to the uncertainty of the measurement.

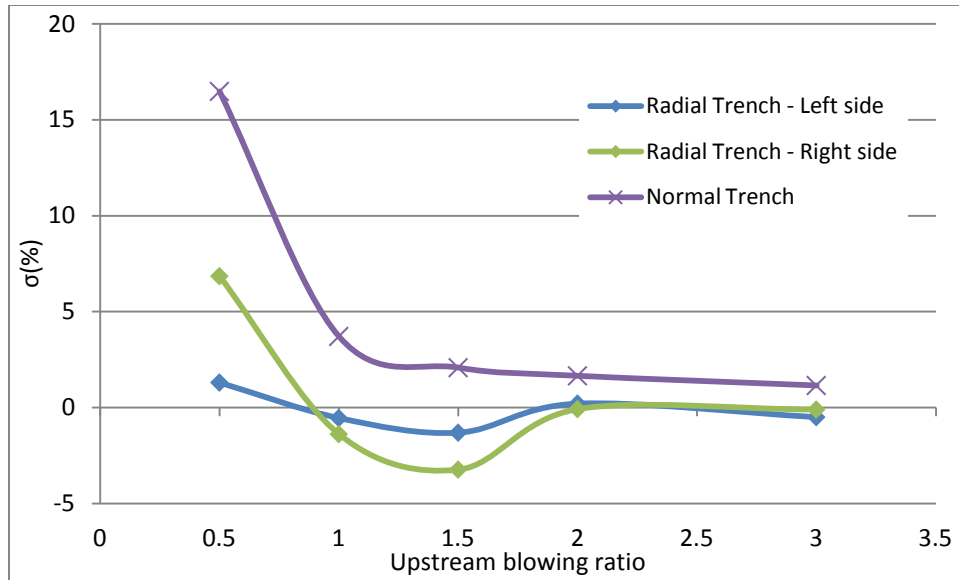


Figure IV-25. Phase II – Augmentation ( $\sigma$ ), at  $\phi=1.3$ ,  $x/d_j = 51$ , US: Slot, DS: Variable

#### IV.3.7 Phase I and II - Volumetric comparison of upstream input

Figure IV-19 and Figure IV-25 reveal that the slot was highly successful at reducing the heat flux augmentation on downstream fan, ramp and trench designs. As the blowing ratio of the slot was increased above 1.0 the heat flux augmentation was reduced to nearly zero for all four downstream cooling configurations. This is a significant result indicating the potential to eliminate the effects of secondary reactions by means of a slot. Two parameters affect the slots' ability to cool. First, the quantity of air ejected from the slot is enough to reduce the local concentrations of reactive species. Additionally, the angle of injection and uniform flow of coolant provided by the slot enabled the high volume flow rate to stay near the wall. Angled injection reduces the component of momentum perpendicular to the flow as shown by Ito et al, [8]. To determine the impact of momentum ratio, a comparison is made based on standard liters per minute (SLPM) between the offset normal and slot in the upstream location.

Figure IV-27 and Figure IV-28 show heat flux using a downstream ramp and normal trench, respectively. Both figures reveal that the quantity of air is not as important as the method of injection. Injecting a similar amount of air from the offset normal holes did not have the same effect as the slot. In fact, the heat flux continued to increase when increasing the blowing ratio from the offset normal configuration. The higher momentum flux jet traveling further from the wall due to the stronger vertical motion decreases offset normal performance. High momentum normal jets create stagnation points in the flow due to the perpendicular velocity as shown by Lilley [13]. Therefore, perpendicular jets are more likely to increase the local turbulence, which increases convective heat transfer coefficients and mixing. This indicated that the orientation of the coolant was the significant factor, not just the amount. Figure IV-26 presents photographs taken of the offset normal and slot during testing at a volume flow rate of  $\sim 9.5$  SLPM, which is equivalent to a blowing ratio of 10.0 and 2.0 from the offset normal and slot, respectively.



Figure IV-26. Volume flow rate comparison between slot (Left) and offset normal (right):  $\dot{V} = 9.5$  SLPM;  $\phi=1.3$ ; US: Slot or Offset normal; DS: Normal trench

Another important result from this mass flow comparison indicates higher blowing ratios push the air further from the wall. As a result, mainstream temperature increases away from the wall and not next to the surface. While this may help bring reactions to completion, the downstream surface is left unprotected. This indicates the increase in heat flux at high offset normal blowing ratios is primarily a result of the downstream air coolant ejection aided by the increased turbulence created by the offset normal ejection.

Another interesting comparison of Figure IV-27 and Figure IV-28 is the amount of heat flux reduction. Figure IV-27 is a result from phase I testing and uses a ramp in the downstream location. Figure IV-28 is a result from phase II and uses a normal trench in the downstream location. Remember that phase II uses heated oil and phase I uses room temperature water to cool the plate. This means the surface temperature of phase I testing is higher than phase II resulting in increased heat flux in all phase I cases. However, the amount of heat flux reduction when using the upstream slot in combination with the downstream normal trench, is significantly more than the reduction seen when using the slot upstream from the ramp. This shows that the ramp should not be used in series with an upstream input.

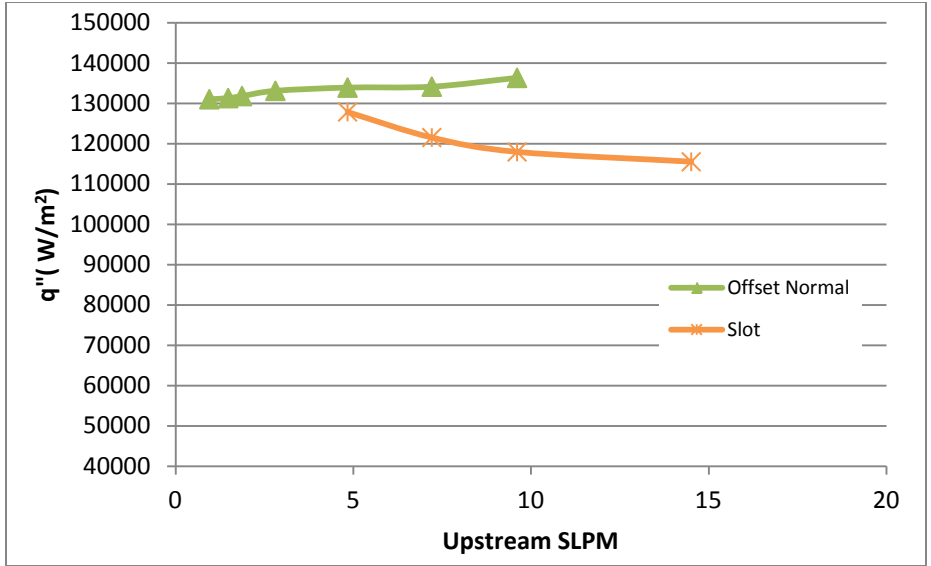


Figure IV-27. Phase I - SLPM comparison at  $\phi=1.3$ ,  $x/d_j = 51$ ,  
US: offset normal or slot DS: Ramp

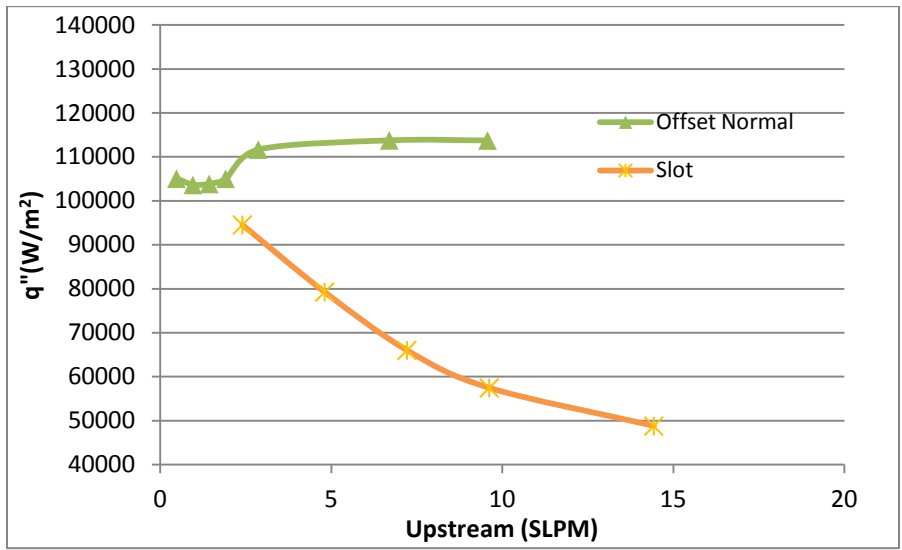


Figure IV-28. Phase II - SLPM comparison at  $\phi=1.3$ ,  $x/d_j = 51$ ,  
US: offset normal or slot DS: Normal Trench

#### **IV.4 Phase I and II - Normalized wall temperature**

A unique comparison can be made to estimate worst-case blowing conditions using both phase I and II data. Worst-case conditions indicate blowing ratios and configurations that create the highest heat release. This comparison can be made by estimating the local gas temperature and then comparing it to a theoretical maximum. As explained previously, Equation (III-9) provides an estimation of the maximum driving temperature that could be achieved when local  $\phi = 1.0$  with the reaction occurring at the wall surface. The normalized temperature method contributes to the second objective. (to determine a method/s of finding worst-case burning in the turbine conditions.)

The normalized temperature charts compare blowing ratios between series and non-series coolant injection. The heat flux and convective coefficient data used to perform the normalized temperature analysis was taken from the previous heat flux investigations. Series data is presented according to the upstream blowing ratio whereas the non-series data (alone) is presented according to the downstream blowing ratio. As before, series configuration testing sets the downstream blowing ratio at 2.0 while varying the upstream blowing ratio (slot or offset normal). Non-series testing does not include an upstream input so the downstream blowing ratio is varied. This means the horizontal axis represents downstream blowing ratio when referencing the normal trench only configuration and upstream blowing ratio when referencing the series configurations. This does not present an apples-to-apples comparison in terms of total volume of flow however, our goal of finding worst-case blowing conditions and configuration can still be met.

For method I, the nitrogen equivalent convective coefficient is assumed similar to the air case convective coefficient. Figure IV-29 provides the phase I normalized temperature for the

normal trench alone and in series with the slot and offset normal. A relatively constant  $\theta = 0.5$  was achieved for the normal trench only case. The addition of the offset normal injection upstream decreased the normalized gas temperature by as much as ten percent. Figure IV-29 shows the upstream normal trench's mass addition served to reduce the potential energy release at the downstream location. However, Figure IV-2 and Figure IV-15 show the offset normal producing a higher heat flux than the normal trench alone. Higher heat flux is a result of either a higher convective coefficient or adiabatic wall temperature.

Increased volume near the wall can significantly improve performance by using a slot configuration upstream of the normal trench. The slot can completely protect the downstream injection gas from free stream radicals. Figure IV-29 shows that the normalized gas temperature was decreased by fifty percent by the presence of the slot and another ten percent as the slot's blowing ratio was increased from 1.0 to 2.0. This result indicates the importance of both volume as well as injection method, as the important factors in reducing the effects of secondary reactions in film cooling flows.

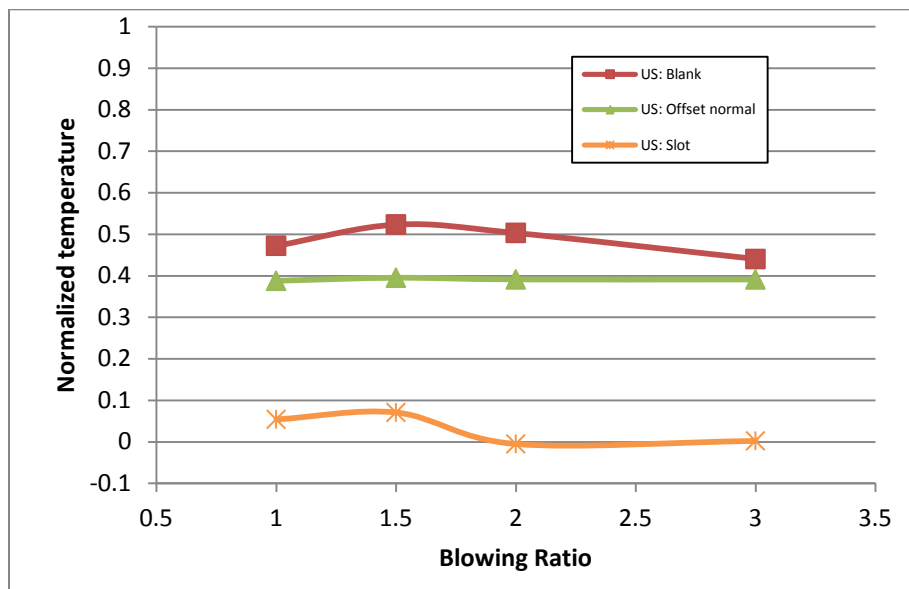


Figure IV-29. Phase I - Normalized temperature at  $\phi=1.3$ , US: Variable, DS: Normal trench

Phase I data does not indicate the maximum heat release in any of the three configurations. This is primarily due to the assumed heat transfer coefficient. As previously discussed, the upper limit of 1.0 is an overestimation by an amount proportional to the difference between the local wall temperature in the nitrogen case and the actual free stream temperature. The local free stream temperature of 1759 K was assumed to be the driving temperature at every blowing ratio and is used to calculate the convective coefficient in the nitrogen case. This assumption is not correct because the driving temperature is decreased with the increase of the adiabatic efficiency of a particular configuration. This overestimation of the nitrogen case convective coefficient is due to the use of the mainstream temperature instead of actual local gas temperature in Equation (III-10).

Phase II analysis of normalized temperature contains adiabatic wall temperature estimates based on the averaged zero-zero baseline values. This averaged convective coefficient is used in all cases for each blowing ratio. Therefore, it does not account for the known increase in the convective heat transfer coefficient with increasing blowing ratio. However, reaching the theoretical maximum is possible when using the mean convective heat transfer coefficient. The potential to reach theoretical maximum is shown below in Figure IV-30 .

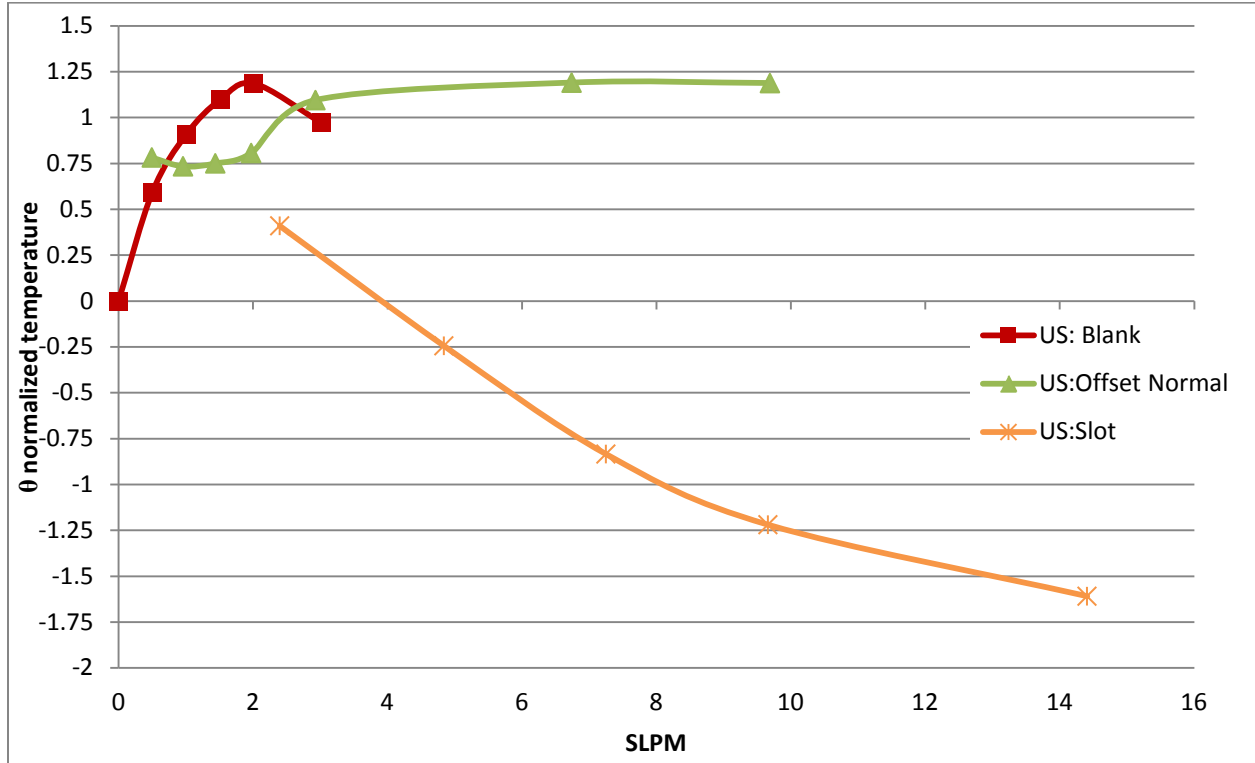


Figure IV-30. Phase II - Normalized temperature at  $\phi=1.3$ , US: Variable, DS: Normal trench

Figure IV-30 exhibits phase II normalized temperature for the normal trench alone and in series with the upstream offset normal and slot configuration. Data suggest the potential to reach worst-case conditions at several different blowing ratios both with and without the offset normal in the upstream location. Normal trench with no upstream input exceeds the maximum theoretical amount at blowing ratios of 1.5 and 2. Additionally, at an upstream offset normal blowing condition greater than or equal to 3.0, the maximum theoretical temperature is exceeded. This is the direct result of not being able to account for the increase in the convective heat transfer coefficient with increasing blowing ratio.

A small correction can be made to the data to correct for increases in the convective heat transfer coefficient. As shown by Bunker et al [22], normal trench injection can increase the convective heat transfer coefficient at an  $x/d_j$  of 25-diameters by ~3% or more. An increase of 3% in convective heat transfer coefficient would decrease the calculated adiabatic wall temperature according to Equation (III-12). This has a significant impact on the results presented in Figure IV-30. A 3% increase in the convective coefficient yields large changes in the calculated adiabatic wall temperature. Differences in normalized temperature due to the 3% increase in the convective coefficient are shown in Table IV-1. The 3% increase in the convective coefficient can dramatically change the normalized temperature as shown in the right hand column under the  $\Delta$  symbol. The delta between the normalized wall temperature ( $\theta$ ) and the normalized wall temperature calculated with a 3% increase ( $\theta$  increased h), shows significant differences of up to 20%. This would lower those conditions shown above that exceed 1.0 to something much closer to 1.0.

Table IV-1. Change in normalized temp with 3% increase in “h”,  $\phi=1.3$ , US: Variable, DS: Normal trench

Configuration	US Blowing Ratio	DS Blowing Ratio	Adiabatic Temp (K)	Adiabatic w/ increased h (K)	$\theta$	$\theta$ increased h	$\Delta$
Normal Trench	0	0	1765.122	1735.027	0.000	-0.094	0.094
	0	0.5	1955.813	1921.275	0.594	0.487	0.108
	0	1	2056.697	2019.516	0.909	0.793	0.116
	0	1.5	2117.305	2078.495	1.098	0.977	0.121
	0	2	2145.374	2105.691	1.185	1.061	0.124
	0	3	2076.612	2038.499	0.971	0.852	0.119
Normal Trench & Slot	0.5	2	1896.711	1831.708	0.410	0.208	0.203
	1	2	1686.831	1626.266	-0.244	-0.433	0.189
	1.5	2	1497.493	1440.520	-0.834	-1.012	0.178
	2	2	1373.904	1320.028	-1.219	-1.387	0.168
	3	2	1248.832	1197.632	-1.609	-1.769	0.160
Normal Trench & Offset Normal	0.5	2	2016.254	1979.521	0.783	0.668	0.114
	1	2	2000.796	1964.561	0.734	0.622	0.113
	1.5	2	2005.964	1969.648	0.751	0.637	0.113
	2	2	2024.043	1987.317	0.807	0.692	0.114
	3	2	2116.594	2077.546	1.095	0.974	0.122
	7	2	2147.118	2107.342	1.190	1.067	0.124
	10	2	2146.347	2106.578	1.188	1.064	0.124

#### IV.4.1.1 *Adiabatic wall temperature extrapolation*

Another method is available for finding adiabatic wall temperature. As explained previously one can change the wall temperature to manipulate the heat flux to the wall from the gas. The use of two different cooling fluids provides the opportunity to take advantage of a difference in wall temperature and extrapolate to find the adiabatic wall temperature. Adiabatic wall temperature extrapolation contributes to the second objective of this thesis (to determine a method/s of finding worst-case burning in the turbine conditions).

The top three lines in Figure IV-31 represent air-cooling while the bottom three lines represent nitrogen-cooling. The slopes of the top three lines are larger, in the negative direction, than the bottom three lines. This is an expected result because the convective coefficient in the reacting cases should be higher due to the additional turbulence generated by the combustion process. However, the slope should not be great enough to allow for an extrapolation to a lower wall temperature than the corresponding nitrogen cases, shown in Figure IV-32. A lower wall temperature in the reacting case is a clear indication of error in the data or not using enough data points to obtain a good estimate.

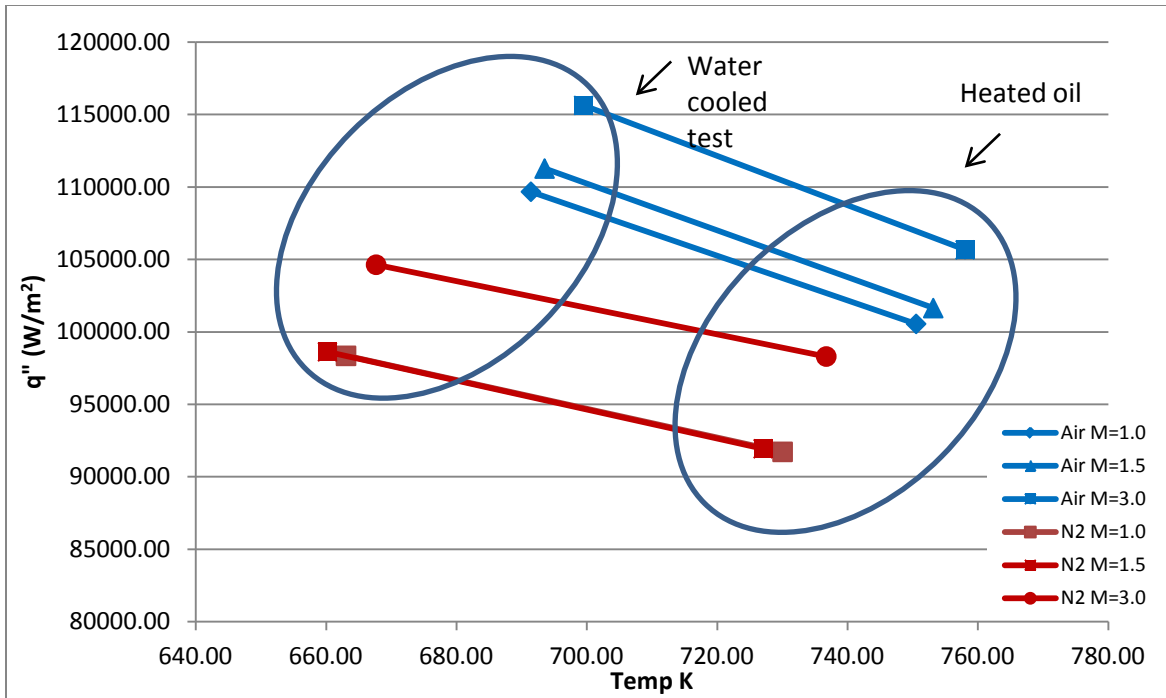


Figure IV-31. Air and N<sub>2</sub> extrapolation zoom view at  $x/d_j = 25$ ; US: Blank DS: Normal Trench -  $\phi=1.3$

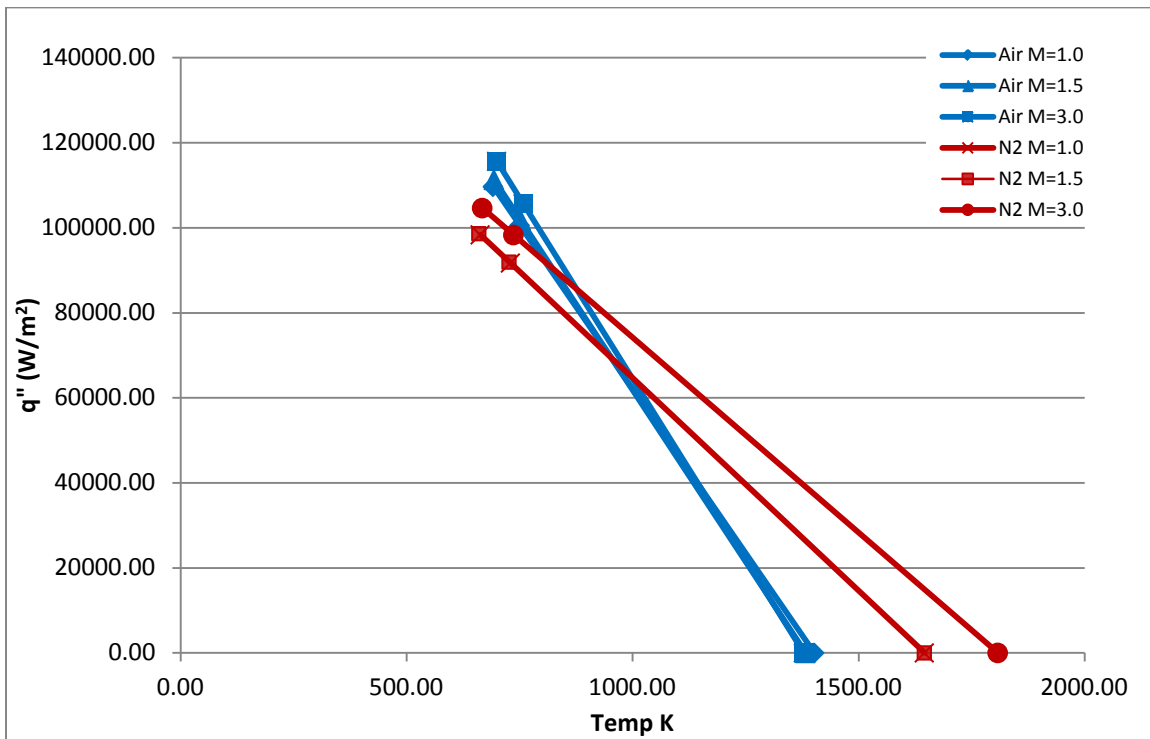


Figure IV-32. Adiabatic wall temp extrapolation at  $x/d_j = 25$ ; US: Blank DS: Normal Trench -  $\phi=1.3$

A summary of the data shown in Figure IV-31 is provided below in Table IV-2. Although the adiabatic effectiveness is incorrect, the indicated convective heat transfer coefficients are as expected. The cases where reactions are happening result in higher convective coefficients than the cases where reactions are not happening. However, the magnitude of the differences in convective coefficients is subject to the inaccuracy of the data plotted. Each of the calculated values in the right three columns of Table IV-2 are a result of the plotted data above. Adiabatic effectiveness is a result of Equation (II-2) assuming a  $T_{\infty}$  of 1740 K and a  $T_{c,exit}$  of 600 K.

Air injected cases should result in a local gas temperature higher than the incoming stack temperature, which is above 1750 K. Inaccuracies consist of several factors however the most significant of which is inconsistency in baseline phase I data used to find the water data points. Uncorrected data consisting of errors  $> 5\%$  may be contributing a significant amount of error due to the magnitude of the extrapolation from tested values. In addition to this, the distance between each of the data points is small compared to the distance of the extrapolation. More data points with greater separation would provide a better approximation of adiabatic wall temperature.

Table IV-2. Air & N<sub>2</sub> adiabatic effectiveness at y/d = 25; US: Blank DS: Normal Trench -  $\phi=1.3$

Norm Trench		Water conditions	Oil conditions	Water Conditions	Oil conditions				
Down Stream M	Air (0) / N2 (1)								Adiabatic eff
		q" 25 diam (W/m2)	q" 25 diam (W/m <sup>2</sup> )	T wall 25 diam (K)	T wall 25 diam (K)		Slope of Line	Adiabatic wall T (K)	
1.00	0	109673.87	100551.94	691.46	750.56		-154.33	1402.09	0.30
1.50	0	111274.47	101642.43	693.56	753.19		-161.53	1382.45	0.31
2.00	0	112333.80	102319.44	694.08	752.95		-170.13	1354.37	0.34
3.00	0	115634.31	105660.85	699.54	758.07		-170.39	1378.19	0.32
1.00	1	98346.50	91718.88	663.09	730.08		-98.94	1657.06	0.07
1.50	1	98619.93	91932.88	660.24	727.08		-100.05	1645.98	0.08
2.00	1	100076.86	93706.74	660.38	728.70		-93.24	1733.73	0.01
3.00	1	104635.33	98299.60	667.71	736.77		-91.74	1808.30	-0.06



## V. Conclusions and Recommendations

### V.1 Overview

This thesis examines the chemical kinetic and fluid dynamic phenomena associated with burning in the turbine. Specifically, this thesis investigates different analysis methods to help compare and contrast different cooling configurations as well as identify worst-case conditions. Both mitigation and identification of worst-case conditions are important to future turbine design. The objectives of this thesis are to identify appropriate analysis methods to find optimum film cooling conditions and to determine a method/s of finding worst-case burning in the turbine conditions. Finding worst-case film cooling conditions in a reacting flow is crucial to the future development of the UCC.

This thesis consisted of a two-phase investigation of film cooling in a reacting environment. The first phase of the investigation utilized water as the coolant in the heat exchanger. The second phase of testing utilized heated oil as the coolant in the heat exchanger. Both phases of testing used various film cooling configurations, alone and in series, to find the best and worst-case film cooling conditions for burning in the turbine. Testing results of both phases are evaluated using the same analysis tools. Analysis tools consist of a comparison of heat flux, augmentation, and normalized temperature. One additional analysis method was introduced which combines both phases of testing and is referred to as adiabatic wall temperature extrapolation.

Specifically, this work investigated the potential heat release from a normal trench, radial trench, fanned and ramped configurations. These configurations were tested alone and in series with an upstream input from an offset normal and slot configuration. Phase II conditions were

corrected using a polynomial to correlate combustor pressure to mainstream conditions. Overall, most of the phase I data trends corresponded with the phase II data.

## **V.2 Augmentation Conclusion**

Our relative comparison of augmentation and heat flux results revealed interesting trends in performance. The normal trench design was more effective in the nitrogen cases than the air cases and resulted in the worst augmentation when used alone. The ramped configuration produced additional turbulence due to the upstream facing step. Results showed the ramped configuration should be used without upstream input. The radial trench produces mainstream asymmetric results due to the radial velocity component of the coolant. Radial velocity was beneficial to the left side of the plate due to the right to left velocity component of the coolant. Radial velocity was detrimental to the right side of the test plate due to a lack of coolant. Series injection proved to be valuable with the angled slot. The angled slot configuration was shown to be the ideal cooling geometry in a reacting flow due to its high volume output at a low stream wise momentum ratio. Offset normal cooling works best at low blowing ratios where the coolant does not have enough momentum to separate from the downstream surface. By comparing the offset normal to the slot at similar mass flows, it became apparent that the volume of injection was not as important as the method of injection.

Developing a useful analysis tool for comparing different film cooling configurations was one of the objectives of this thesis. Augmentation and heat flux provided a relative and actual performance measure. Both augmentation and heat flux account for changes in adiabatic wall temperature as well as the convective coefficient. Both of these parameters are significant when making comparisons between different configurations. However, care must be taken in

maintaining consistent mainstream conditions. The amount of heat flux and the amount of augmentation is dependent on the mainstream conditions as well as the blowing conditions. Overall, augmentation and heat flux have proven to be useful in determining the optimum film-cooling configuration in a reacting flow.

### **V.3 Adiabatic Wall Temperature Calculation Conclusion**

A direct method of calculating the adiabatic wall temperature was presented as normalized temperature. Two different normalized temperature methods are shown as method I and method II. Method I used the convective coefficient from the corresponding nitrogen case to predict the adiabatic wall temperature in the air case. Method II used the averaged heat transfer coefficient found in the zero-zero baseline data to predict the adiabatic wall temperature. Both methods of calculation provide an estimation of the adiabatic wall temperature by making an assumption about the local convective coefficient.

Being able to identify best and worst-case scenarios was another objective of this thesis. Each normalized temperature calculation method had its advantages however, the second method, which uses the baseline average convective coefficient, proved to be more valuable than the first. Method II normalized temperature calculation identified several potential worst-case scenarios. Being able to identify a worst-case scenario provides insight into design constraints and cooling configurations to avoid using. Additionally, this method could be improved with a better estimation of the changes to the convective heat transfer coefficient with increasing blowing ratio.

Finding the convective heat transfer coefficient is possible by using another direct method of calculation. An extrapolation technique was investigated by combining the results

from both phases. This extrapolation technique requires the ability to change the walls surface temperature. Changing the wall's surface temperature allows one to manipulate the heat flux to the wall from the fluid. Ultimately, this method proved inaccurate due to the error in the extrapolated adiabatic wall temperatures. However, if one could set up an experiment where the wall temperature could be scaled through a broad range of temperatures, the extrapolation method could be a very valuable analysis tool to future investigations.

#### **V.4 Recommendations for Future Work**

The analysis tools presented provide the means necessary to find a good solution to mitigate the burning in the turbine problem. However, these methods are only as valuable as the quality of the data obtained. Future testing should include a full analysis of the flow conditions in the test rig, over time, to account for the changing mainstream conditions. Being able to eliminate the sources of error during testing will enhance the products of the methods presented providing better results.

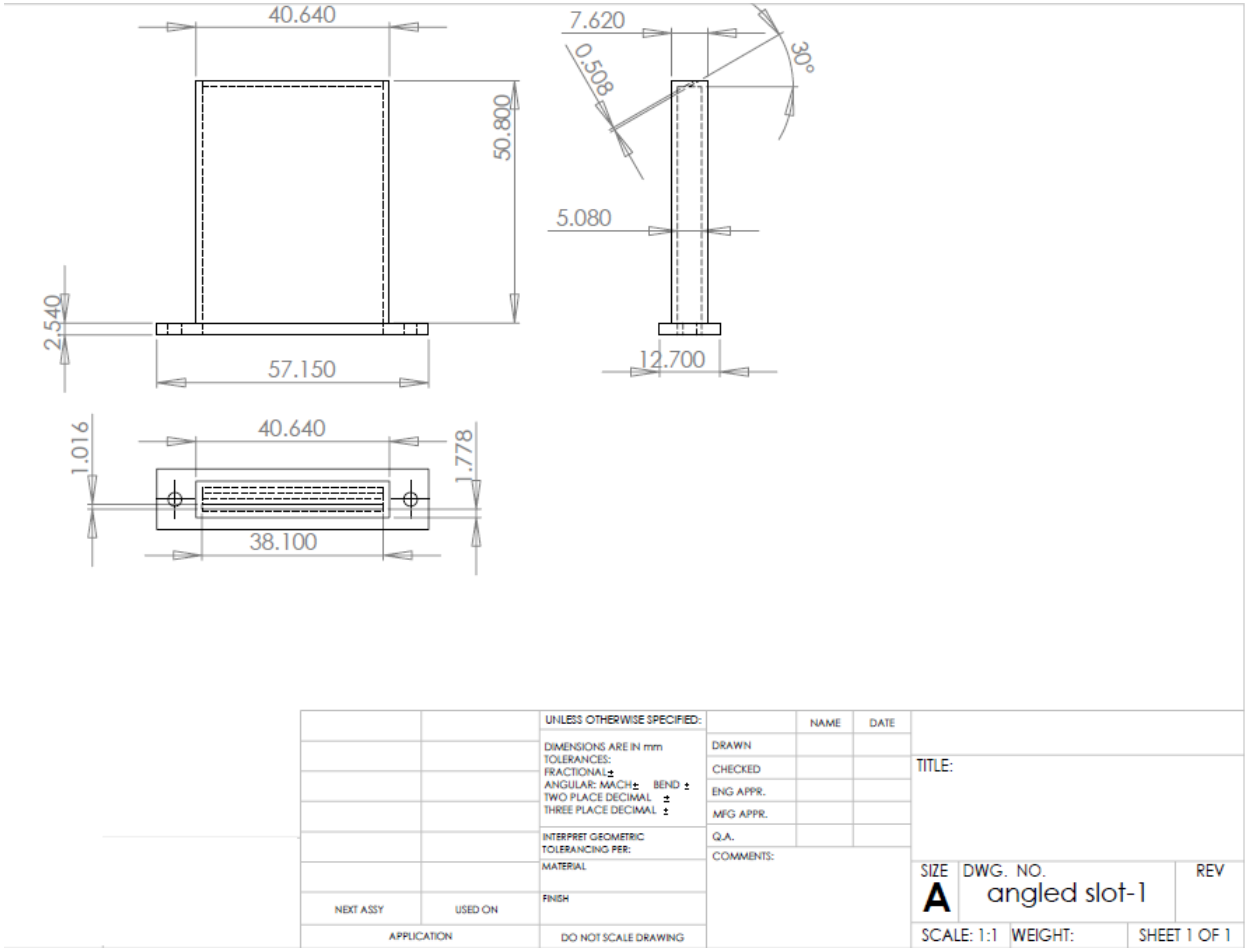
Future investigations into the burning in the turbine problem should focus on mimicking current slot designs used in combustor liners. The slot was the optimum design as shown in the previous results section. Therefore, future film cooling configurations should take advantage of the slots performance and vary the type of slot used as shown by Mellor [10]. Since the turbine vane at the UCC combustor cavity outlet is a stationary configuration, a slot may be more suitable to this design.

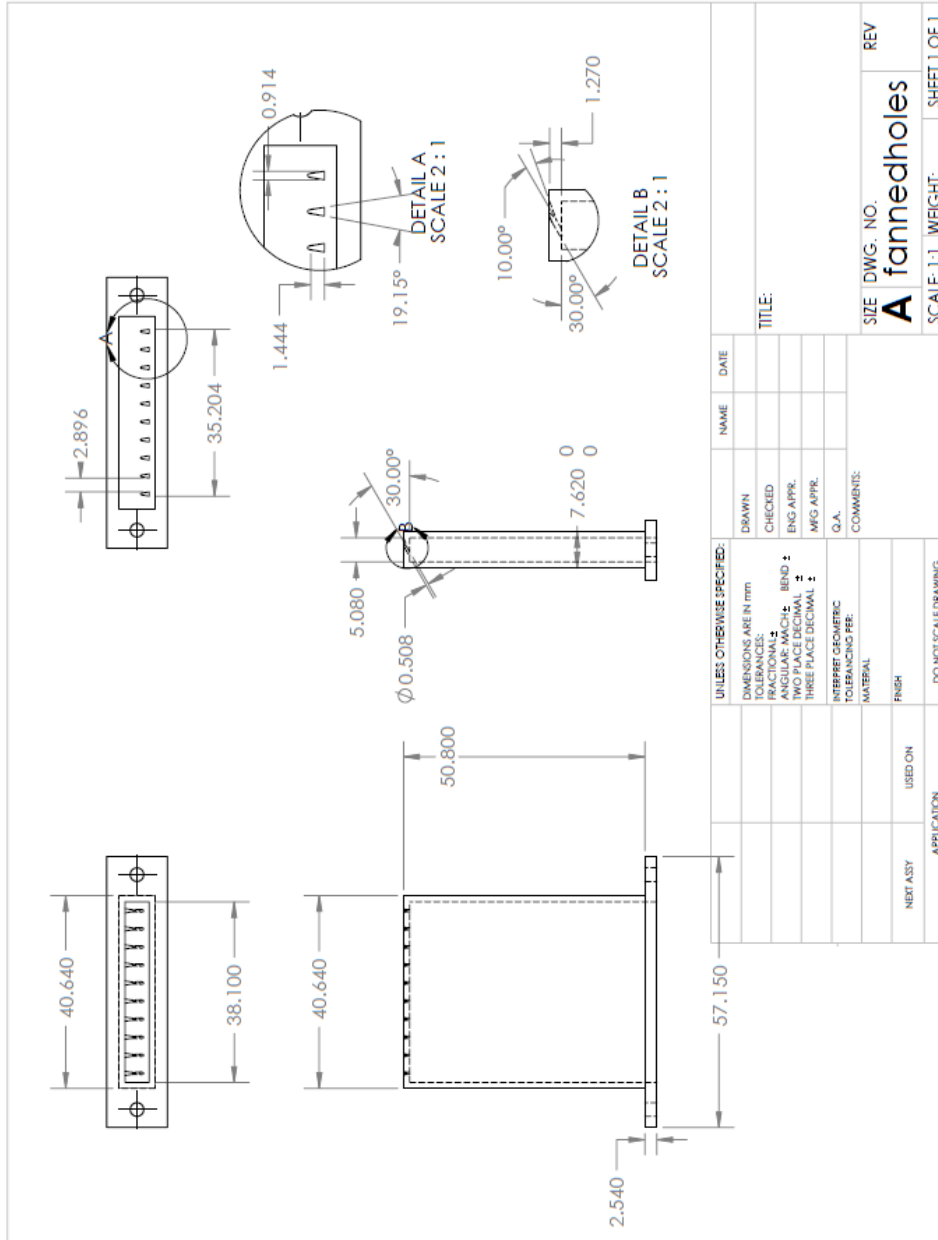
Additionally, one of the big unknowns in this thesis was the relationship between the convective heat transfer coefficient and blowing ratio. The ability to predict the changes in the convective coefficient would allow for greater accuracy in predicting adiabatic wall temperature.

Researching the changes in the convective coefficient due to slot coolant injection would be beneficial to future testing and UCC design.

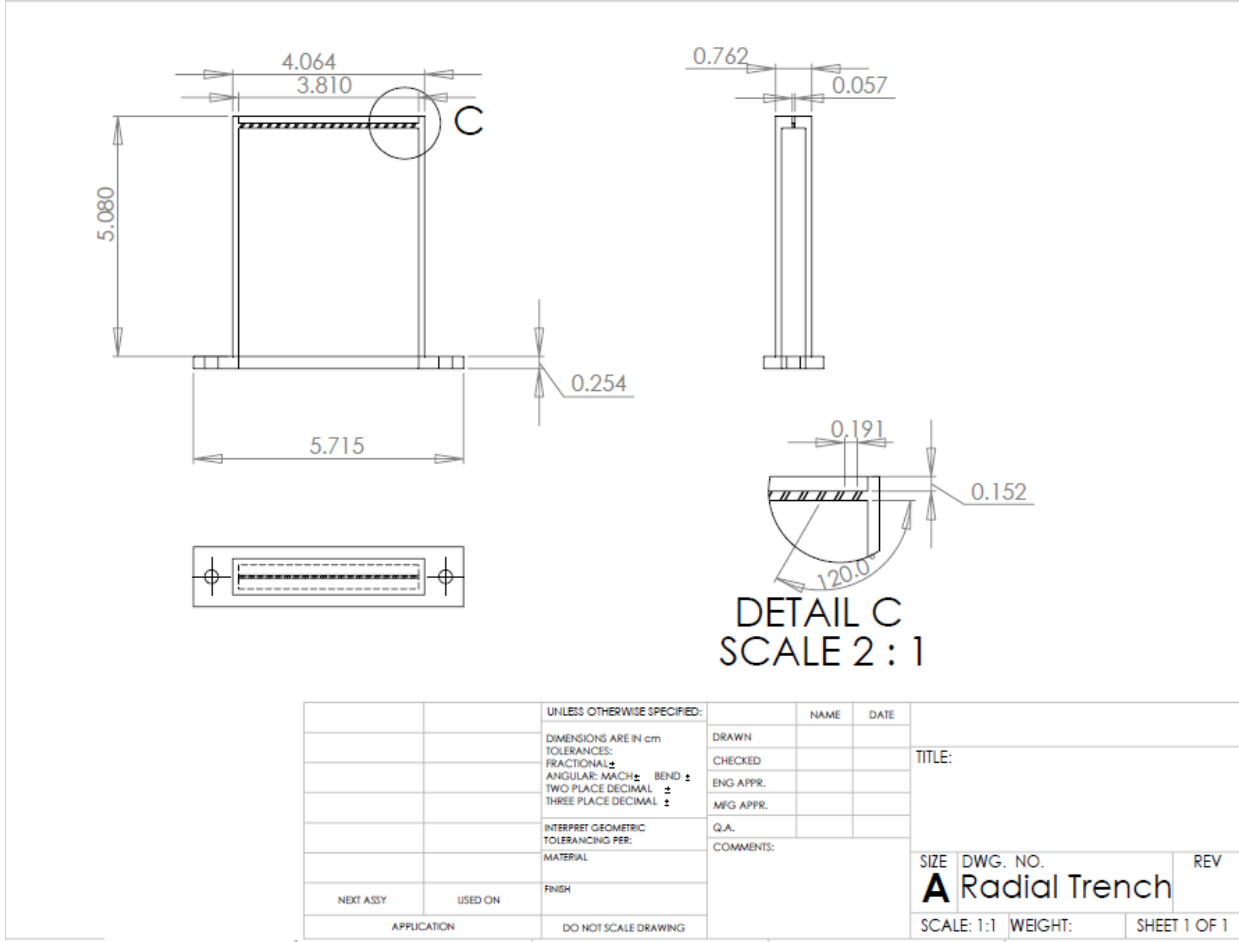
# APPENDIX A

## Drawings of rig and cooling plenums

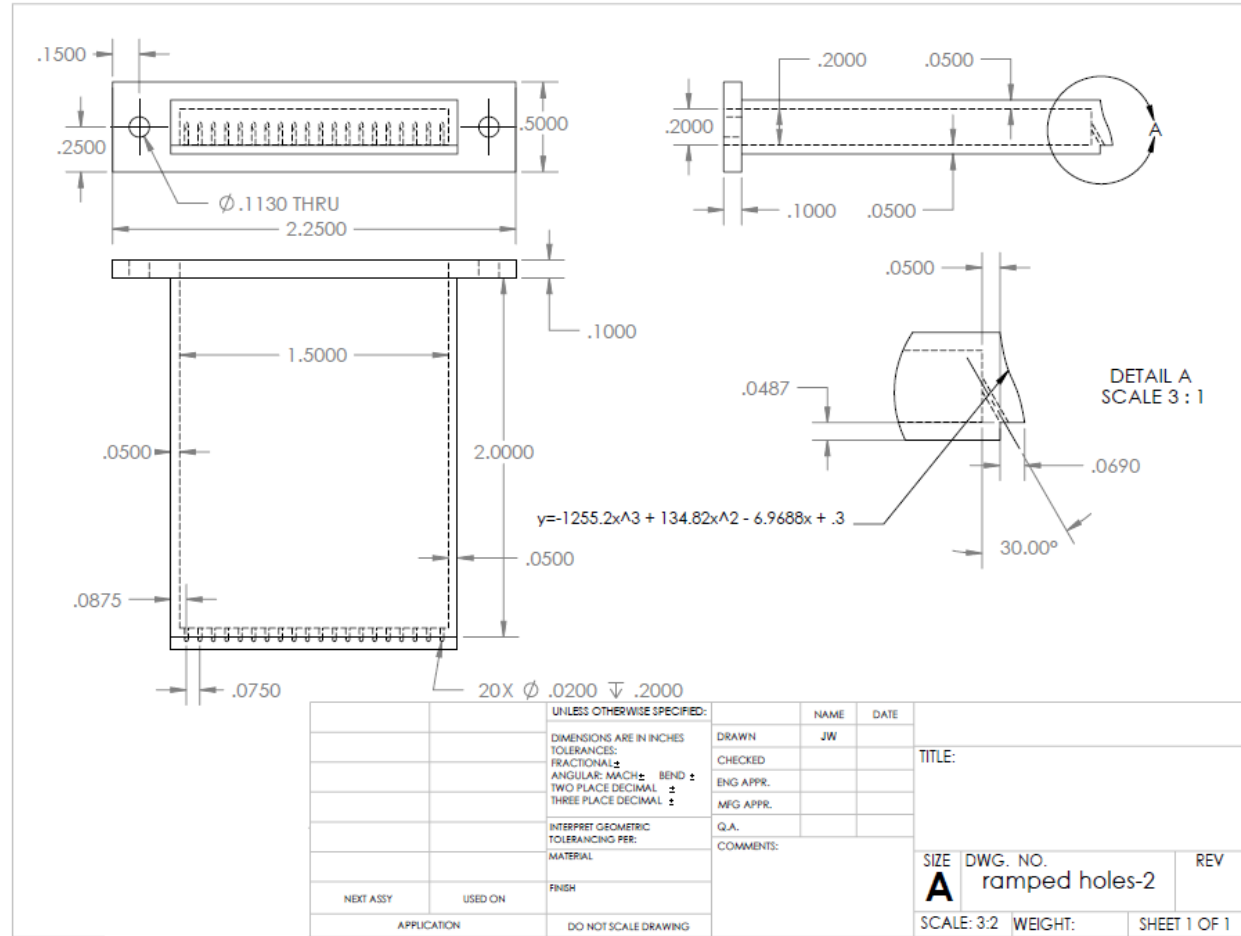




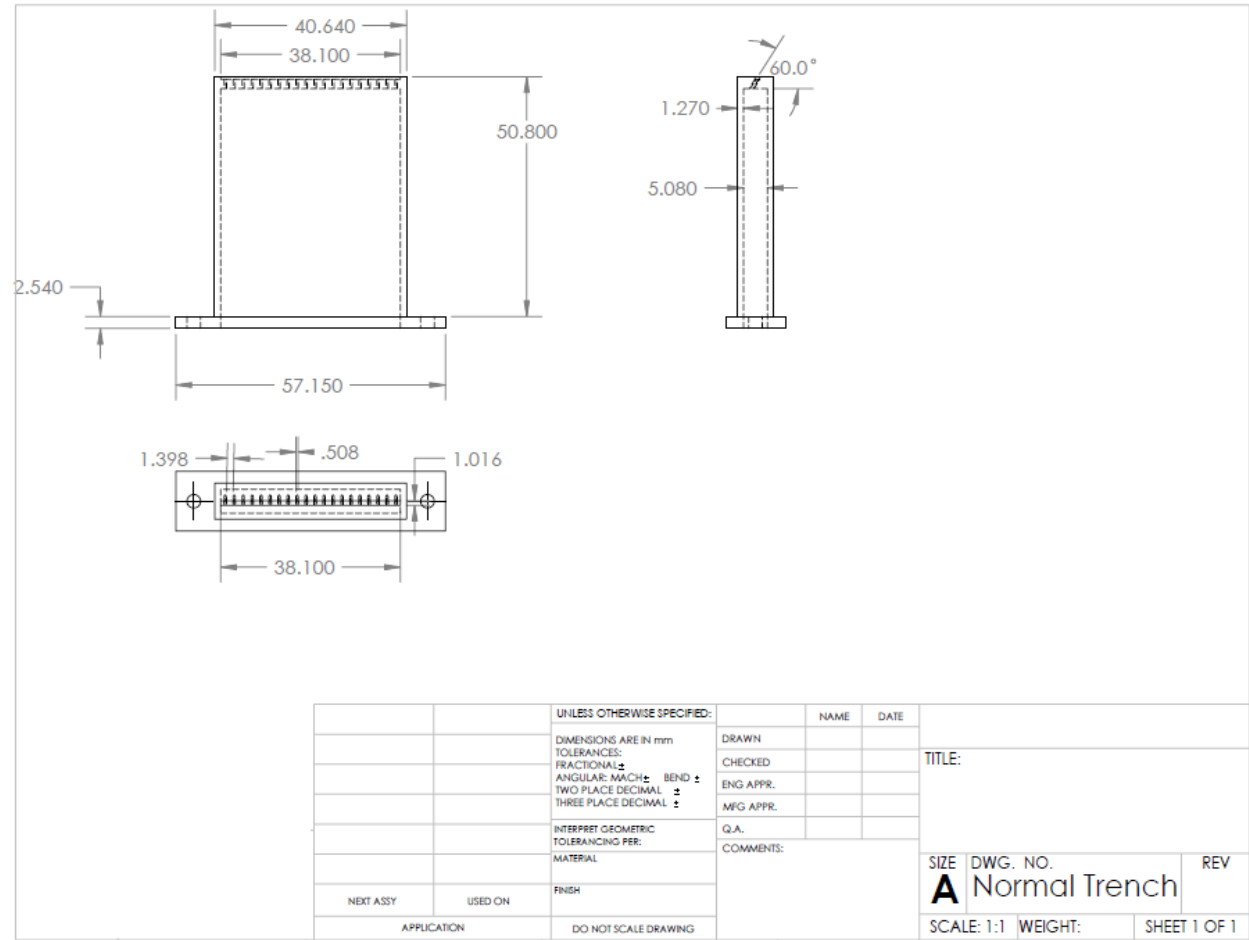




		UNLESS OTHERWISE SPECIFIED:	NAME	DATE	
		DIMENSIONS ARE IN cm	DRAWN		
		TOLERANCES:	CHECKED		TITLE:
		FRACTIONAL: ±	ENG APPR.		
		ANGULAR: MACH ± BEND ±	MFG APPR.		
		TWO PLACE DECIMAL ±	Q.A.		
		THREE PLACE DECIMAL ±	COMMENTS:		
		INTERPRET GEOMETRIC TOLERANCING PER:			
		MATERIAL			SIZE DWG. NO. REV
NEXT ASSY	USED ON	FINISH			<b>A</b> Radial Trench
APPLICATION		DO NOT SCALE DRAWING			SCALE: 1:1 WEIGHT: SHEET 1 OF 1



UNLESS OTHERWISE SPECIFIED:		NAME	DATE
DIMENSIONS ARE IN INCHES		DRAWN	JW
TOLERANCES:		CHECKED	
FRACTIONAL: ±		ENG APPR.	
ANGULAR: MATCH: BEND ±		MFG APPR.	
TWO PLACE DECIMAL: ±		Q.A.	
THREE PLACE DECIMAL: ±		COMMENTS:	
INTERPRET GEOMETRIC TOLERANCING PER:		SIZE	DWG. NO.
MATERIAL		<b>A</b>	ramped holes-2
NEXT ASSY	USED ON	FINISH	REV
APPLICATION		DO NOT SCALE DRAWING	
		SCALE: 3:2	WEIGHT:
		SHEET 1 OF 1	



## APPENDIX B CEA summary pages

*The file titled "propane-air-1.3.out" is the CEA calculation of reactor products using propane and air at an equivalence ratio of 1.3.*

Feb 16, 2012 02:01 PM

FileEditor:propanr-air-1.3.out

```

*****
NASA-GLENN CHEMICAL EQUILIBRIUM PROGRAM CEA2, MAY 21, 2004
  BY BONNIE MCBRIDE AND SANFORD GORDON
REPS: NASA RP-1311, PART I, 1994 AND NASA RP-1311, PART II, 1996
*****

```

```

problem phi,eq,ratio=1.3,
hp p,atm=1, t,k=2300
react
fuel=C3H8 moles=1 t,k=300
oxid=Air moles=18.3022 t,k=300
output short
plot p t m cp
end

```

### THERMODYNAMIC EQUILIBRIUM COMBUSTION PROPERTIES AT ASSIGNED

#### PRESSURES

CASE =

	REACTANT	MOLES	ENERGY KJ/KG-MOL	TEMP K
FUEL	C3H8	1.0000000	-104543.521	300.000
OXIDANT	Air	18.3022000	-71.689	300.000

O/F= 12.06069 %FUEL= 7.656563 R, EQ. RATIO= 1.299544 PHI, EQ. RATIO= 1.300000

#### THERMODYNAMIC PROPERTIES

P, BAR	1.0132
T, K	2123.52
RHO, KG/CU M	1.5353-1
H, KJ/KG	-183.81
U, KJ/KG	-843.77
G, KJ/KG	-21374.5
S, KJ/(KG)(K)	9.9790
M, (1/n)	26.753
(dLV/dLP)t	-1.00030
(dLV/dLT)p	1.0086
Cp, KJ/(KG)(K)	1.5896
GAMMAS	1.2478
SON VEL, M/SEC	907.5

#### MOLE FRACTIONS

*Ar	0.00799
*CO	0.07354

FileEditor:propanr-air-1.3.out

*CO2	0.06609
*H	0.00066
*H2	0.03362
H2O	0.15166
*NO	0.00007
*N2	0.66596
*O	0.00001
*OH	0.00041
*O2	0.00001

\* THERMODYNAMIC PROPERTIES FITTED TO 20000.K

The second CEA file titled "mainstreamheatrelease.out" shows the products and temperatures resulting from stoichiometric combustion using the products resulting from "propane-air-1.3.out".

FileEditor:mainstreamheatrelease.out

Feb 16, 2012 02:15 PM

```

*****
NASA-GLENN CHEMICAL EQUILIBRIUM PROGRAM CEA2, MAY 21, 2004
BY BONNIE MCBRIDE AND SANFORD GORDON
REFS: NASA RP-1311, PART I, 1994 AND NASA RP-1311, PART II, 1996
*****

```

```

problem case=Freestreamheatrelease
hp p,atm=1, t,k=2300
react
fuel=CO moles=.07354 t,k=1759
fuel=H moles=.00066 t,k=1759
fuel=H2 moles=.03362 t,k=1759
fuel=OH moles=.00041 t,k=1759
oxid=Air moles=.255 t,k=550
name=Ar moles=.00799 t,k=1759
name=CO2 moles=.06609 t,k=1759
name=H2O moles=.15166 t,k=1759
name=NO moles=.00007 t,k=1759
name=N2 moles=.66596 t,k=1759
output short
plot p t rho m cp
end

```

THERMODYNAMIC EQUILIBRIUM COMBUSTION PROPERTIES AT ASSIGNED

PRESSURES

CASE = Freestreamheatr

	REACTANT	MOLES	ENERGY KJ/KG-MOL	TEMP K
FUEL	CO	0.0735400	-62485.519	1759.000
FUEL	H	0.0006600	248364.458	1759.000
FUEL	H2	0.0336200	44795.644	1759.000
FUEL	OH	0.0004100	82785.756	1759.000
OXIDANT	Air	0.2550000	7304.867	550.000
NAME	Ar	0.0079900	30365.630	1759.000
NAME	CO2	0.0660900	-316522.002	1759.000
NAME	H2O	0.1516600	-181029.891	1759.000
NAME	NO	0.0000700	140350.418	1759.000
NAME	N2	0.6659600	47520.037	1759.000

O/F= 0.27608 %FUEL= 78.364774 R,EQ.RATIO= 1.000822 PHI,EQ.RATIO= 1.003578

THERMODYNAMIC PROPERTIES

P, BAR 1.0132  
T, K 2086.93  
RHO, KG/CU M 1.6533-1

FileEditor:mainstreamheatrelease.out

H, KJ/KG	-512.71
U, KJ/KG	-1125.57
G, KJ/KG	-20323.7
S, KJ/(KG) (K)	9.4929

M, (1/n)	28.313
(dLV/dLP)t	-1.00133
(dLV/dLT)p	1.0429
Cp, KJ/(KG) (K)	1.8697
GAMMAS	1.2041
SON VEL,M/SEC	859.0

## MOLE FRACTIONS

*Ar	0.00861
*CO	0.00567
*CO2	0.11019
*H	0.00011
*H2	0.00160
H2O	0.15174
*NO	0.00102
*N2	0.71696
*O	0.00006
*OH	0.00142
*O2	0.00261

\* THERMODYNAMIC PROPERTIES FITTED TO 20000.K

## VI. BIBLIOGRAPHY

1. Koff, B. L., "Gas Turbine Technology Evolution: A Designer's Perspective," *Journal of Propulsion and Power*, vol. 20, no. 4, pp. 577-595, 2004.
2. Mattingly, Jack D., Heiser, William H., and Pratt, David T., *Aircraft Engine Design*, Przemieniecki, J. S., Ed. Reston, VA: American Institute of Aeronautics and Astronautics, INC., 2002.
3. Thole, K. A., Sinha, A. K., Bogard, D. G., and Crawford, M. E., "Mean Temperature Measurements of Jets with a Crossflow for Gas Turbine Film Cooling Application," in *Rotating Machinery Transport Phenomena*, J H Kim and W J Yang, Eds. New York: Hemisphere, 1992, pp. 69-85.
4. Teekaram, A., Forth, C., and Jones, T., "The use of Foreign Gas to Simulate the Effects of Density Ratios in Film Cooling," *Journal of Turbomachinery*, vol. 111, pp. 57-62, 1989.
5. Schmidt, D. L., and Bogard, D. G., "Effects of Free-Stream Turbulence and Surface Roughness on Film Cooling," in *International Gas Turbine and Aeroengine Congress & Exhibition*, 96-GT-462 ASME, Birmingham, U.K., 1996.
- 6 Schmidt, D. L., Sen, B., and Bogard, D. G., "Film Cooling With Compound Angle Holes: Adiabatic Effectiveness," *Journal of Turbomachinery*, vol. 118, pp. 807-813, October 1996.
7. Gritsch, M., Schulz, A., and Wittig, S., "Adiabatic Wall Effectiveness Measurements of Film-Cooling Holes With Expanded Exits," *Journal of Turbomachinery*, vol. 120, no. 3, pp. 549-557, July 1998.
8. Ito, S., Goldstein, R. J., and Eckert, E., "Film Cooling of a Gas Turbine Blade," *Journal of Engineering for Power*, vol. 100, pp. 476-482, 1978.
9. Pedersen, D. R., "Effect of Density Ratio on Film Cooling Effectiveness for Injection Through a Row of Holes and for a Porous Slot," University of Minnesota, ph.D. thesis 1972.

10. Mellor, A. M., Bahr, D. W., Derr, W. S., Depooter, K., Dodds, W. J., Eickhoff, H. E., Gardner, L., Hammond, D. C., Peters, J. E., Whyte, R. B., Winterfeld, G., *Design of Modern Turbine Combustors*, A M Mellor and J H Whitelaw, Eds. San Diego, CA: Academic Press INC, 1990.
11. Burrus, D. L., Chahrour, C. A., Foltz, H. L., Sabla, P. E., Seto, S. P., Taylor, J. R., "Energy Efficient Engine Combustor Test Hardware," NASA CR-168301, 1984.
12. Sturgess, G. J., and Pfeiffer, G. D., "Design of Combustor Cooling Slots for High Film Effectiveness: Part 2 - Film Initial Development". ASME paper 85-GT-35, 1985.
13. Lilley, D. G., "Swirling Flows and Lateral Jet Injection for Improved Mixing and Combustion," in *49th AIAA Aerospace Sciences Meeting Including the New Horizons Forum and Aerospace Exposition, AIAA 2011-103*, Orlando, FL, 2011.
14. Polanka, Marc D., Lin, C., Evans, David S., Sekar, W. S., Zelina, J., Anderson, W. S., "Heat Release in Turbine cooling I: Experiment and Computational Comparison of Three Geometries," *Journal of Propulsion and Power*, vol. 27, no. 2, pp. 257-267, 2011.
15. Stouffer, S.D., Striebich, R.C., Frayne, C. W., and Zelina, J., "Combustion Particulates Mitigation Investigation Using a Well-Stirred Reactor," AIAA Paper No. 2002-3723, 2002.
16. Lin, C., Holder, R. J., Sekar, B., Zelina, J., Polanka, M. D., Thornburg, H. J., and Briones, A. M., "Heat Release in Turbine Cooling II: Numerical Details of Secondary Combustion Surrounding Shaped Holes." *Journal of Propulsion and Power* vol. 27(2), 2011: 269-81.
17. Bohan, Brian T. "Analysis of Flow Migration in an Ultra-Compact Combustor." Master's Thesis, Air Force Institute of Technology, 2011.
18. Evans, Dave S. "The Impact of Heat Release in Turbine Film Cooling." Master's Thesis, Air Force Institute of Technology, 2008.
19. Waitz, I. A., Milanes, D. W., Kirk, D. R., and Fidkowski, K. J., "Gas Turbine Engine Durability Impacts of High Fuel-Air Ratio Combustors: Near Wall Reaction Effects on Film-Cooled Backward-Facing Step Heat Transfer." *Journal of Engineering for Gas Turbines and Power* vol. 128, 2006: 318-25.

20. Lukachko, S. P., Kirk, D. R., and Waitz, I. A., "Turbine Durability Impacts of High Fuel-Air Ratio Combustors, Part I: Potential for Intra-Turbine Oxidation of Partially-Reacted Fuel," in *ASME Turbo Expo, GT-2002-30077*, Amsterdam, The Netherlands, 2002.
21. Material Datasheet H-3009a, "Hastelloy® X Alloy", Kokomo IN: Haynes International Inc., 1997.
22. Bunker, R. "Film Cooling Effectiveness due to Discrete Holes within a Transverse Surface Slot". *IGTI Turbo Expo. June 3-6, 2002, Amsterdam, Netherlands. GT-2002-30178*.
23. Harrison, K. L., Dorrington, J. R., Dees, J. E., Bogard, D. G., and Bunker, R., "Turbine Airfoil Net Heat Flux Reduction with Cylindrical Holes Embedded in a Transverse Trench" *IGTI Turbo Expo, May 14-17, 2007, Montreal, Canada, GT2007-27996*.
24. Gordon, S. and McBride, B. J., "Computer Program for Calculation of Complex Chemical Equilibrium Compositions and Applications", NASA Reference Publication 1311, October 1994.
25. Bunker, Ronald., Harrison, Katharine L., Dorrington, John R., Dees, Jason E., and Bogard, David G., "Turbine Airfoil Net Heat Flux Reduction with Cylindrical Holes Embedded in a Transverse Trench," in (*GT2007-27996*) *Proceedings of GT2007, ASME Turbo Expo 2007: Power for Land Sea and Air*, Montreal, Canada, May 14-17, 2007.
26. Smith, D. E., Bubb, J. V., Popp, O., Grabowski III, H., Diller, T. E., Schetz, J. A., "An Investigation of Heat Transfer in A Film Cooled Transonic Turbine Cascade, Part I: Steady Heat Transfer," in *International Gas Turbine & Aeroengine Congress & Exhibition, 2000-GT-202*, Munich, Germany, 2000.
27. Sturgess, G. J., "Design of Combustor Cooling Slots for High Film Cooling Effectiveness: Part I - Film General Development," Paper 85-GT-35, 1985.
28. Incropera, DeWitt, Bergman, and Lavine, *Fundamentals of Heat and Mass Transfer*, 6th ed. Hoboken, New Jersey: John Wiley and Sons Inc, 2007.

<b>REPORT DOCUMENTATION PAGE</b>				<i>Form Approved OMB No. 074-0188</i>	
<p>The public reporting burden for this collection of information is estimated to average 1 hour per response, including the time for reviewing instructions, searching existing data sources, gathering and maintaining the data needed, and completing and reviewing the collection of information. Send comments regarding this burden estimate or any other aspect of the collection of information, including suggestions for reducing this burden to Department of Defense, Washington Headquarters Services, Directorate for Information Operations and Reports (0704-0188), 1215 Jefferson Davis Highway, Suite 1204, Arlington, VA 22202-4302. Respondents should be aware that notwithstanding any other provision of law, no person shall be subject to a penalty for failing to comply with a collection of information if it does not display a currently valid OMB control number.</p> <p><b>PLEASE DO NOT RETURN YOUR FORM TO THE ABOVE ADDRESS.</b></p>					
<b>1. REPORT DATE (DD-MM-YYYY)</b> 22 March 2012		<b>2. REPORT TYPE</b> Master's Thesis		<b>3. DATES COVERED (From - To)</b> Sep 2010 - March 2012	
<b>4. TITLE AND SUBTITLE</b> Impact of Trench and Ramp Film Cooling Designs to Reduce Heat Release Effects in a Reacting Flow				<b>5a. CONTRACT NUMBER</b>	
				<b>5b. GRANT NUMBER</b>	
				<b>5c. PROGRAM ELEMENT NUMBER</b>	
<b>6. AUTHOR(S)</b> DeLallo, Michael R., Capt, USAF				<b>5d. PROJECT NUMBER</b>	
				<b>5e. TASK NUMBER</b>	
				<b>5f. WORK UNIT NUMBER</b>	
<b>7. PERFORMING ORGANIZATION NAMES(S) AND ADDRESS(S)</b> Air Force Institute of Technology Graduate School of Engineering and Management (AFIT/ENY) 2950 Hobson Way WPAFB OH 45433-7765				<b>8. PERFORMING ORGANIZATION REPORT NUMBER</b>  AFIT/GAE/ENY/12-M10	
<b>9. SPONSORING/MONITORING AGENCY NAME(S) AND ADDRESS(ES)</b> Air Force Research Laboratories Propulsion Directorate, Combustion Branch 1950 Fifth Street, Building 490 WPAFB, OH 45433-7765 POC: Dr. David Blunck, Phone:937-255-7216 David.Blunck@wpafb.af.mil				<b>10. SPONSOR/MONITOR'S ACRONYM(S)</b> AFRL/RZTC	
				<b>11. SPONSOR/MONITOR'S REPORT NUMBER(S)</b>	
<b>12. DISTRIBUTION/AVAILABILITY STATEMENT</b>  APPROVED FOR PUBLIC RELEASE; DISTRIBUTION UNLIMITED.					
<b>13. SUPPLEMENTARY NOTES</b> This material is declared a work of the U.S. Government and is not subject to copyright protection in the United States.					
<b>14. ABSTRACT</b> Increasing combustor fuel-air ratios are a recent area of concern in gas turbine film cooling due to the potential for heat release on the surface of film-cooled components. This investigation compared four different cooling designs on their heat release potential: namely fanned, normal and radial trenched, and ramped. Measurements of heat flux to the downstream surface, when subjected to a reacting mainstream flow, provide a qualitative comparison between the four tested configurations. Furthermore, this work studied the effect of multiple injection points in series along the surface of a flat plate. An upstream set of normal holes and an upstream slot are evaluated on their ability to protect the downstream coolant flow from the fuel rich mainstream. Results are presented in terms of heat flux, augmentation of heat flux, and adiabatic wall temperature calculations. Downstream heat release is suspected to be a result of coolant interaction with local free radical concentrations. Concentrations, volume flow rates and jet to mainstream momentum ratio dictate local equivalence ratio and hence, the available local enthalpy generation.					
<b>15. SUBJECT TERMS</b> Jet engines, ultra-compact combustor, UCC, inter-turbine burner, turbine-engine, film cooling					
<b>16. SECURITY CLASSIFICATION OF:</b>			<b>17. LIMITATION OF ABSTRACT</b>	<b>18. NUMBER OF PAGES</b>	<b>19a. NAME OF RESPONSIBLE PERSON</b>
a. REPORT	b. ABSTRACT	c. THIS PAGE			Dr. Marc Polanka
U	U	U	UU	149	<b>19b. TELEPHONE NUMBER (Include area code)</b> (937)255-3636, ext 7519 Email: marc.polanka@afit.edu

Standard Form 298 (Rev. 8-98)  
Prescribed by ANSI Std. Z39-18